Nonlinear Dynamical Analysis of Interaction between Rubberlike Membrane and Liquid in a Rectangular Tank

矩形タンクでのゴム膜／流体連成系の非線形動的解析

WORAWAT PARASIL

DEPARTMENT OF AEROSPACE ENGINEERING

GRADUATE SCHOOL OF SYSTEM DESIGN

TOKYO METROPOLITAN UNIVERSITY

MARCH 2017

Nonlinear Dynamical Analysis of Interaction between Rubberlike Membrane and Liquid in a Rectangular Tank

矩形タンクでのゴム膜／流体連成系の非線形動的解析

by

Worawat Parasil

Student ID 12991574

Submitted to the Department of Aerospace Engineering,

Graduate School of System Design,

in partial fulfillment of the requirements for the degree of

Doctor of Philosophy in Aerospace Engineering

at

Tokyo Metropolitan University

March 2017

Certified by advisor

Professor Naoyuki Watanabe

Department of Aerospace Engineering

Graduate School of System Design

Tokyo Metropolitan University

Doctoral thesis committee:

Professor Naoyuki Watanabe	Tokyo Metropolitan University (Chairman)
Professor Koichi Kitazono	Tokyo Metropolitan University
Professor Hironori Sahara	Tokyo Metropolitan University
Associate Professor Toshio Tagawa	Tokyo Metropolitan University

ABSTRACT

The aim of this study was to clarify the nonlinear oscillation of the sloshing-like behavior such as a container made of a flexible membrane like a bladder tank. The 2-dimensional interaction of a rubberlike membrane and liquid problem in a rectangular tank under horizontal vibration was examined by the arbitrary Lagrangian-Eulerian finite element method (ALE-FEM) and the influence of a large excitation and membrane tension were examined. Then, the 3-dimensional rubberlike membrane and liquid interaction problem in rectangular tank under the horizontal vibration are examined by the arbitrary Lagrangian-Eulerian finite element method (ALE-FEM). The influences of large excitation were examined. According to many parametric calculations, we confirmed validity of the present analysis and comparison with sloshing model. In addition, the effects of finite deformations of the membrane, i.e., material and geometrical nonlinearities in the membrane and the liquid, are taken into consideration. Furthermore, the influences of tank depth were examined. The effects of finite deformation of the membrane, i.e., material and geometrical nonlinearities of the membrane and liquid were considered. Last, the implementation of rectangular tank containing liquid with membrane-covered upper and lower surfaces is taken into consideration.

Keywords: Rubberlike membrane, Liquid–structure interaction, Arbitrary Lagrangian–Eulerian, Vibration

CONTENTS

LIST OF FIGURES

LIST OF TABLES

NOMENCLATURE

Symbols	Definition
$\mathbf{a}$	Acceleration vector of the external force
A_x	Acceleration in x direction
A_z	Acceleration in z direction
$\mathbf{E}$	Green–Lagrange strain matrix
$\bar{\mathbf{E}}$	Green–Lagrange strain matrix in the principal direction
E_a	Green-Lagrange strain in principle direction
$\bar{E}_a$	Principal strain
E_{x0}	Initial strains in the x directions
E_{y0}	Initial strains in the y directions
E_x	Strains in the x directions
E_y	Strains in the y directions
E_{xy}	Strains in the $x-y$ plane
$\boldsymbol{e}$	Green-Lagrange strain
$\boldsymbol{f}$	Potential function
f	Physical quantity
f'	Space time differentiation
$\dot{f}$	Material time differentiation
f^*	Mesh time differentiation in ALE coordinate system
g	Acceleration due to gravity
$\mathbf{G}$	Residual vector
$\boldsymbol{h}$	Tank depth
$\mathbf{H}$	Shape function
$\boldsymbol{n}_l$	Normal vector to the liquid boundary

$\boldsymbol{n}_s$	Normal vector to the membrane surface
p	Undetermined multipliers of Lagrange's method
R_x	Initial position of body
R_y	Current position of body
R_z	Initial position of body and mesh
r	Radius of curvature
$\boldsymbol{s}$	Second Piola-Kirchhoff stress (2PK stress)
S_a	Second Piola-Kirchhoff stress in principle direction
$\bar{\mathbf{S}}$	Second Piola-Kirchhoff stress in the principal direction
T	Internal stress in structure
$\widetilde{\mathbf{T}}$	Surface forces on the structure
$\mathbf{t}$	Internal force imparting stress on the body
t	Time
t_m	Membrane thickness
Δt	Time increment
$\hat{\mathbf{u}}$	Mesh displacement
$\boldsymbol{u}$	Membrane displacement vector
u	Membrane displacement in x direction
$\mathbf{u}_l$	Lower membrane displacement
u_n	Normal membrane displacement
$\mathbf{u}_u$	Upper membrane displacement
$\mathbf{U}$	Nodal displacement
$\boldsymbol{v}$	Liquid velocity vector
v	Membrane displacement in y direction
v_n	Normal velocity

v_{ln}	Normal liquid velocity
$\boldsymbol{v^p}$	Movement velocity of material
$\boldsymbol{v^m}$	Movement velocity of mesh
W	Ogden strain energy function
w	Membrane displacement in z direction
$\boldsymbol{x}$	Initial coordinate system
$\mathbf{x}_s$	Position vector of the initial shape of solid
$\hat{\mathbf{x}}$	Initial coordinate in the liquid domain
$\mathbf{X}$	Nodal coordinate
$\boldsymbol{y}$	Current coordinate
$\mathbf{y}_l$	Position vector of the current shape of liquid
$\mathbf{y}_s$	Position vector of the current shape of solid
$\boldsymbol{z}$	Mesh coordinate
λ_a	Stretching rate
λ_i	Lagrange undetermined multiplier
μ_r, α_r	Material constant
σ_a	Cauchy stress
ρ_l	Density of liquid
ρ_m	Density of the membrane
ϕ	Liquid velocity potential
β_N, γ_N	Parameters of the Newmark-β method
Π_{liquid}	Functional on liquid domain
Π_{solid}	Functional on structural domain
$\Pi_{\text{liquid+solid}}$	Functional of liquid-structure interaction problem
π_l	Liquid pressure

Ω_l	Liquid domain
Ω_s	Structural domain
Γ_{ls}	Liquid-structure boundary

CHAPTER 1

INTRODUCTION

1.1 Research background and literature review

On the ground, sloshing means any motion of a free liquid surface inside a container. The dynamics of a liquid sloshing is physical phenomenon that is attractive for research. Stability and structural integrity of externally excited filled liquid storage tanks, moving containers, and the many associated applications have been the focus of a wide range of technologies and engineering. The literature reported a variety of analytical and numerical techniques for formulating slosh models for different practical geometries such as large-capacity liquid containers, propellant storage tanks or containers in airplanes, missiles, space vehicles, satellites, or space stations [1].

In the aerospace industry, an overview of the relevant physics and modeling techniques for sloshing liquids in space was given by Vreeburg and Veldman [2]. Sloshing experiments have been designed to provide more information on these issues [3-4]. Most of the reports, however, were concerned with rigid tanks. For example, Faltinsen et al. [5] derived a linear analytical solution for a liquid sloshing in a horizontally excited 2-D rectangular tank, which has been widely used in the validation of numerical models. It is shown that the theory is not valid when the water depth (h) becomes small relative to the tank width (l). This is due to secondary parametric resonance. It is then necessary to include nonlinearly interacting modes having the same order of magnitude. This is demonstrated for a tank with h/l =0.173. They observed fluctuations of the excitation frequency in an initial period up to approximately 10 s. This effect was important to include in the theoretical model. There is good agreement with experimental free surface elevation when h/l >0.28.

Faltinsen and Timokha [6] developed a multimodal approach to describe the nonlinear sloshing in a rectangular tank with a finite water depth. Since the difference between natural frequencies decreases with decreasing liquid depth, this is more likely to occur at low liquid depths. This is a reason why the single dominant mode theories are invalid for small liquid depth. In addition, if the excitation amplitude increases, the liquid response becomes large in an increased frequency domain around the primary natural frequency. The method has been validated by comparing with model tests. Adaptive procedures have been established for all excitation periods as long as the mean liquid depth is larger than 0.24 times the tank width. When h/l <0.24and depth is not shallow, good agreement with experiments has been achieved for isolated excitation periods.

In the case of large deformations, sloshing of the free surface has a very strong effect on performance and stability of structures. The liquid pressure and motion generated by sloshing when the external excitation frequency is close to the natural frequency may lead to structural instability and damage. The typical approach to solving this serious problem is to covering the free surface with a flexible structural member, such as a membrane or an elastic plate [7]. In connection with these issues, analysis of liquid-filled rigid or flexible storage containers has been of great interest to structural engineers in recent years [8-10]. Celebi and Akyıldız [11] described a liquid sloshing in two-dimensional tanks using the finite difference method. It is noted that the structural flexibility and free surface sloshing effects were not properly addressed in the previous studies. In modern technology, structures have trended toward being designed thinner and lighter because of high flexibility of these structures. Moreover, researchers often find strong interactions of propellants with the elastic structure in the control system. For instance, the interaction of a rubberlike membrane and liquid could occur in the rubber bag of the solid container used for the three axis control of a satellite [12].

Liquid propellant is confined within a flexible bladder that is itself contained in a rigid tank, with the role of the bladder being to facilitate discharge of propellant during thrusting and to constrain movement of the propellant from moving, as shown in Fig. 1.1

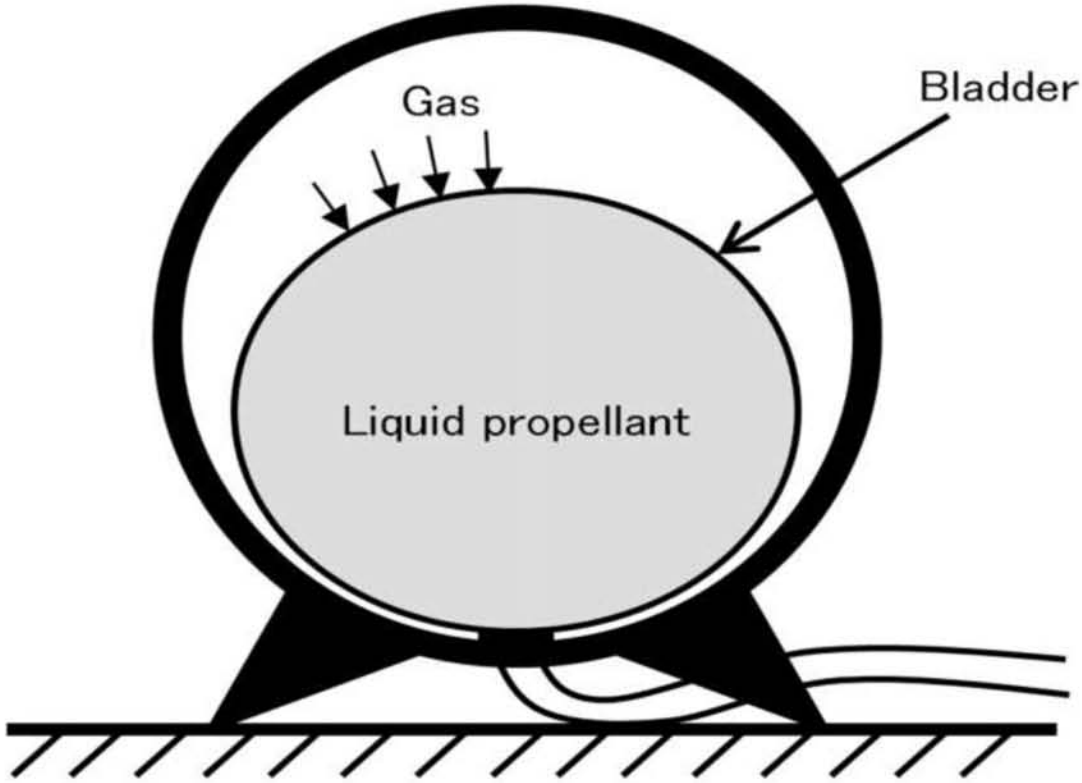

Figure 1.1. Flexible bladder tank.

Kawakami [12] considered a model of a cylindrical tank containing liquid whose surface is covered by a rubberlike membrane and investigated the effects of finite deformations of the membrane using linear analysis and nonlinear finite element analysis. However, this study neglected the motion of the membrane-liquid boundary resulting from the large deformation of the liquid region.

Bauer [13] studied the resonant frequencies of an incompressible and non-viscous liquid in a rigid cylindrical container, in which the free liquid surface was covered by a membrane or elastic plate. The assumption of small deformations was adopted to allow use

of Fourier-Bessel series. This paper stated that a free liquid covered by a membrane or an elastic thin plate increased the resulting frequencies. After this study, Bauer and Chiba [14] extended the study in Ref. [13] to a structure filled with an incompressible viscous liquid, while Bauer and Komatsu [15, 16]studied the coupled hydroelastic frequencies of an inviscid liquid in a circular cylindrical container, in which the free liquid surface was partially covered by an elastic annular plate.

Bauer and Chiba [17, 18] studied the effects of the membrane tension parameter and the stiffness parameter on the amplitudes of both the natural frequency and the decay of oscillations of a membrane-covered viscous liquid in a rigid cylindrical container. The results showed that when a free liquid surface is completely covered by an elastic structure, the natural frequencies of the liquid–structure system are increased owing to the tension or stiffness of the membrane.

Bohun and Trotsenko [19] developed an analytic modal solution for coupled free hydroelastic oscillations of liquid in an upright circular cylindrical container, with the unperturbed free surface of the liquid being covered by an elastic membrane or plate.

Gavrilyuk et al. [20] studied a circular membrane clamped to the edge of a rigid upright circular cylindrical tank filled with an incompressible liquid. This paper examined a linear problem that describes small relative coupled oscillations. The problem was defined to an operator differential equation completed with initial conditions, which imply initial variation and velocities of the stretched membrane. The Cauchy problem was reduced to a spectral boundary problem on linear natural modes (eigenfunctions). The numerical results demonstrated the efficiency of the proposed approximate method. The fast convergence to the solution is facilitated by a functional basis of a specific singular structure. Similar studies have also been performed for rectangular containers [21-23].

Bauer [21] studied the interaction of an elastic bottom with the free surface and liquid in a rigid tank that has a free liquid covered by a membrane in a rectangular container. The results showed that the free liquid surface was completely covered by an elastic structure; also the natural frequencies of the liquid and structure system increased because of the tension or stiffness of the covering membrane.

Bauer [22] theoretically investigated the same issue and discussed the influences of the system parameters on the coupled natural frequencies. He mentioned that a free liquid surface was covered by a membrane in a rectangular container under large deformation. The liquid reduced the influence on the system, while the membrane increased the influence on the system. Specifically, the vibration was dampened due to the increasing membrane tension.

Ikeda and Nakagawa [24] and Ikeda et al. [25] considered the nonlinear interaction of a liquid sloshing in rectangular and cylindrical tanks with an elastic structure in which the motion was orthogonal to the tank vertical walls. For a vertical sinusoidal excitation of an elastic structure carrying a rigid rectangular tank, Ikeda [26] determined the responses of the coupled systems when the structure natural frequency was approximately twice the liquid sloshing frequency. However, hydrodynamic systems, in which the free liquid surface was only partially covered with an elastic membrane, were evaluated. In most cases, the liquid is assumed to be inviscid and incompressible, while the motion was irrotational.

The transient response of liquid storage tanks due to external excitation can be strongly influenced by the interaction between the flexible containment structure and the contained liquid. Due to this fact, the amplitude of the sloshing depends on the nature, amplitude and frequency of the tank motion, liquid-fill depth, liquid properties, and tank geometry [27].

Many previous researches informed that the liquid depth was an important parameter because of nonlinearity of the resonant waves, and the liquid depth related to the tank base dimension [5-6, 28-30]. However, almost studies were interested in sloshing model, while interaction problem was not concerned.

In the systems described above, the elastic structures are on top of the liquid. In the opposite case, Chiba [31] presented theoretical and experimental studies on the axisymmetric free vibration of an elastic bottom plate in a liquid-containing cylindrical tank resulting from the in-plane forces in the plate due to static liquid pressure.

Bauer and Chiba [32] examined the free surface tension effect on the interaction of a viscous liquid in a rigid circular cylindrical tank with a flexible membrane bottom. Chiba et al. [33] presented a linear free hydroelastic vibration analysis of an inviscid liquid with a free surface contained in a rigid cylindrical tank with a flexible membrane bottom. They considered small-amplitude free vibrations of the liquid and the membrane, neglecting static deformations of the bottom membrane. Similar behavior has also been investigated for rectangular containers [34, 35]. In the case of a liquid-filled rectangular container with a sagging bottom membrane, Daneshmand and Ghavanloo [35] investigated the influence of pressure head, membrane length and weight, and distance between the two rigid walls on the natural frequency of interaction of the liquid and membrane.

The studies described above have all considered the systems as two-dimensional and with oscillations confined to one direction. Realistic situations, however, involve motion in three dimensions and the sloshing phenomenon becomes more complicate. For example, Zhang etal. [36] analyzed second-order resonance in a three-dimensional tank using potential theory and perturbation techniques. Such resonance can occur when the sum or difference frequency of one of the excitation frequencies and one of the natural frequencies is equal to another natural frequency.

Hasheminejad and Tafani [37] presented a three-dimensional analysis for an elliptical cylindrical tank with an elastic bottom based on linear potential theory and an eigenfunction expansion in elliptic coordinates. They examined the effects of liquid level, bottom plate elasticity, and cross-sectional aspect ratio on sloshing frequencies and hydrodynamic pressure modes. They also gave a graphical presentation of selected hydrodynamic and structural deformation mode shapes. Most research in this area has concentrated on calculating the natural frequencies of flexible storage containers and has considered just small deformations of flexible cover or bottom plates in two dimensions. However, there is a need for studies in three dimensions of liquid-filled tanks with one or two membrane-covered surfaces, one approach to which is the use of a three-dimensional (3D) finite element method (FEM).

Moreover, there are two major problems that arise in a computational approach to sloshing: the moving boundary conditions at the liquid–tank interface and excessive distortion of liquid elements, which may cause numerical instability or even computational incompleteness [38]. To include nonlinearity and avoid complex boundary conditions of moving walls, a moving coordinate system known as the ALE (Arbitrary Lagrangian Eulerian) method has been used [39].

The ALE method allows arbitrary motion of the moving boundary of the interaction of a rubberlike membrane and liquid with respect to their frame of reference by taking the convection of these points as described in [40–43]. Especially for 2D analysis where the remeshing of the liquid domain can be easily treated with the ALE description, numerical results were in good agreement with experimental results, see [44]. Currently, the mesh distortion and mesh adaptation problem can be resolved, to a large extent, by employing the ALE method with the help of a suitable remeshing and smoothing algorithm [45]. Referring to the papers by Soulaimani and Saad [46] and Cho and Lee [47], the

boundary tracking in both Lagrangian and ALE approaches was straightforward because the liquid mesh moved exactly with the liquid particles.

1.2 Aims of dissertation

The aim of this paper is to analyze the nonlinear sloshing-like behavior that occurs in containers where liquid is confined by a flexible membrane, such as bladder tanks.

The two-dimensional and three-dimensional interaction of a rubberlike membrane and liquid problem in a rectangular tank subject to vibration is investigated using the arbitrary Lagrangian–Eulerian finite element method (ALE-FEM). According to many parametric calculations, we confirmed validity of the present analysis and comparison with sloshing model. In addition, the effects of finite deformations of the membrane, i.e., material and geometrical nonlinearities in the membrane and the liquid, are taken into consideration.

Furthermore, the influences of a large excitation, membrane tension, and tank depth were examined. The effects of finite deformation of the membrane, i.e., material and geometrical nonlinearities of the membrane and liquid were considered. Last, In addition, the implementation of rectangular tank containing liquid with membrane-covered upper and lower surfaces is taken into consideration.

1.3 Layout of dissertation

This thesis is divided into five chapters as follows:

Chapter 1 presents the background and overview of this thesis. Literature studies on the sloshing and liquid-structure interaction are given. The published works reviewed in the study show that membrane–liquid interactions occur in many areas of engineering and it is important to understand their properties. Most research in this area has concentrated on calculating the natural frequencies of flexible storage containers and has considered just small deformations of flexible cover or bottom. To overcome the difficulties caused by the presence of a moving boundary due to large deformations, an arbitrary Lagrangian–Eulerian (ALE) description is used. However, there is a need for studies in large deformation area with more complex behavior of nonlinearity material as rubberlike membrane.

Chapter 2 presents the analytical model and the assumptions made regarding the conditions of the problem. The constitutive equation of the rubberlike membrane, which can be defined in terms of a strain energy function as a hyperelastic material. The corresponding equations for the structural and liquid domains are also given. The variational formulation of the liquid–structure interaction problem is presented. The ALE-FEM based on the Nitikitpaiboon–Bathe method is explained and applied. The mesh updating techniques required for the ALE method at each time step as a result of the large liquid deformations are then described. The Newmark-β method is applied to deal with the time-derivative term in the dominant equation. Finally in this section, the weak form of the dominant equation is discretized using the FEM, the Newton–Raphson method is used to solve the nonlinear equation, and the tangent stiffness matrix is derived, with a convergence test.

Chapter 3 presents numerical evaluations and a discussion of the two-dimensional interaction of a rubberlike membrane and liquid problem in a rectangular tank under horizontal vibration was examined. The influence of a large excitation and membrane tension were examined. The effects of finite deformation of the membrane, i.e., material and geometrical nonlinearities of the membrane and liquid were considered. The numerical evaluations were performed and the time historical response, liquid pressure, and membrane and liquid displacements were presented. The results present the importance of the nonlinearity arising from the membrane itself. Nevertheless, the nonlinearity of a liquid still plays an important role in larger amplitude oscillations.

Chapter 4 presents numerical evaluations and a discussion of the three-dimensional interaction of a rubberlike membrane and liquid problem in a rectangular tank under horizontal vibration was examined. A rectangular tank in which the upper liquid surface is covered by a membrane is analyzed and the results are compared with those of a sloshing model. Some nonlinear characteristics are obtained through parametric calculations and the force equilibrium in the liquid–structure interaction is shown to confirm the validity of the analysis. Effects of tank depth influencing on natural frequency, time history response and displacement of membrane were discussed. Successfully, the results confirmed that the nonlinearity of membrane and liquid was important in the larger amplitude excitation causing by low tank depth.

Chapter 5 discusses the implementation and results of rectangular tank containing liquid with membrane-covered upper and lower surfaces. Some nonlinear characteristics are obtained. Finally, the membrane and liquid nonlinear behavior, especially under large excitation, are discussed.

Chapter 6, the dissertation concludes with a summary of the achievements of the present work. Recommendations for future research are also included in the chapter.

CHAPTER 2

RESEARCH METHOD

2.1 Overview

The analytical model and the assumptions made regarding the conditions of the problem are presented in section 2.2. Section 2.3 presents the constitutive equation of the rubberlike membrane, which can be defined in terms of a strain energy function as a hyperelastic material [48]. The corresponding equations for the structural and liquid domains are also given. Finally in this section, the variational formulation of the liquid–structure interaction problem is presented. In Section 2.6, the ALE-FEM based on the Nitikitpaiboon–Bathe method [42] is explained and applied to the equations from Section 2.3. The mesh updating techniques required for the ALE method at each time step as a result of the large liquid deformations [49] are then described. The Newmark-β method is applied to deal with the time-derivative term in the dominant equation. Finally in this section, the weak form of the dominant equation is discretized using the FEM, the Newton–Raphson method is used to solve the nonlinear equation, and the tangent stiffness matrix is derived, with a convergence test.

2.2 Analytical model

In a two-dimensional model, the rubberlike membrane and liquid interaction model, a rectangular tank of infinite width of 0.8 m was filled with a liquid to a height 0.3 m and the upper surface was covered by a membrane, as shown in Fig. 2.1.

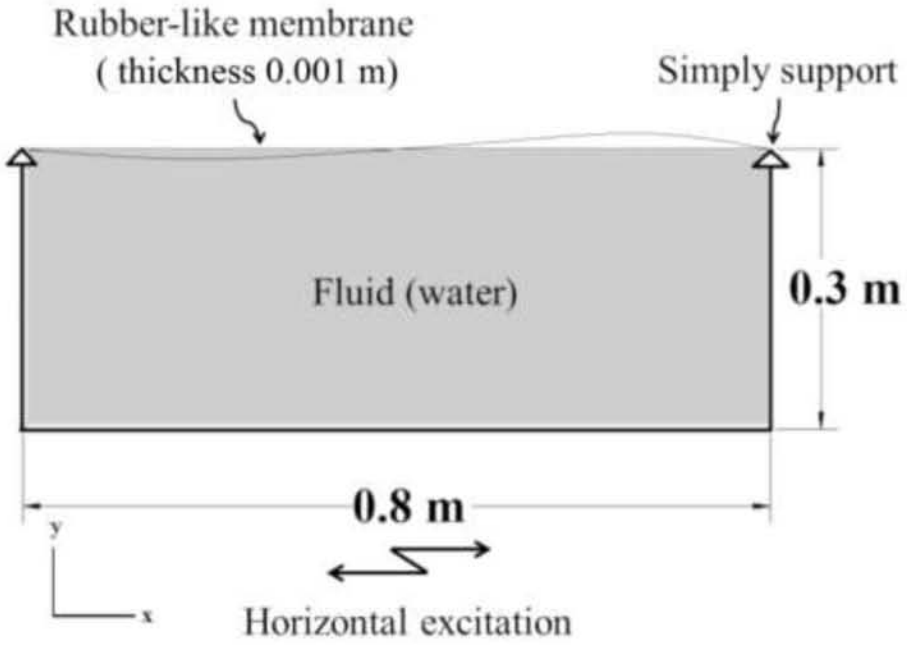

Figure 2.1. 2-D tank which upper surface is covered by membrane.

The tank was assumed to be sufficiently long in the perpendicular direction to the sheet so that a two-dimensional analysis and plane strain domain were reasonable assumptions. The tank was rigid compared to the rubberlike membrane. The rubberlike membrane was thin enough that the assumption of plane stress could be assumed. The bending stiffness and the friction with the liquid were so small that they could be disregarded. The membrane was simply supported at both edges of the tank, and also was assumed to have uniform and constant tension everywhere in advance. The liquid was assumed to be a potential flow that was incompressible, inviscid, and irrotational. The liquid had sufficient heat capacity, and the temperature change could be disregarded.

In a three-dimensional model, the first model of the interaction between rubberlike membranes and liquid, a rectangular tank of infinite height, width $\boldsymbol{a}$, and length $\boldsymbol{b}$ is filled with liquid to a depth $\boldsymbol{h}$, and the upper surfaces of the liquid are covered by membranes as Fig. 2.2. The model is subjected to vibration in the horizontal direction. The tank is rigid compared with the membranes, and the latter are sufficiently thin that the assumption of plane stress can be made. The bending stiffness and the friction with the

liquid are so small that they can be neglected. The membranes are simply supported at both edges and are subjected to uniform and constant tension from the start. The liquid is assumed to be in potential flow that is incompressible, inviscid, and irrotational. The liquid has sufficient heat capacity that its temperature can be taken as constant.

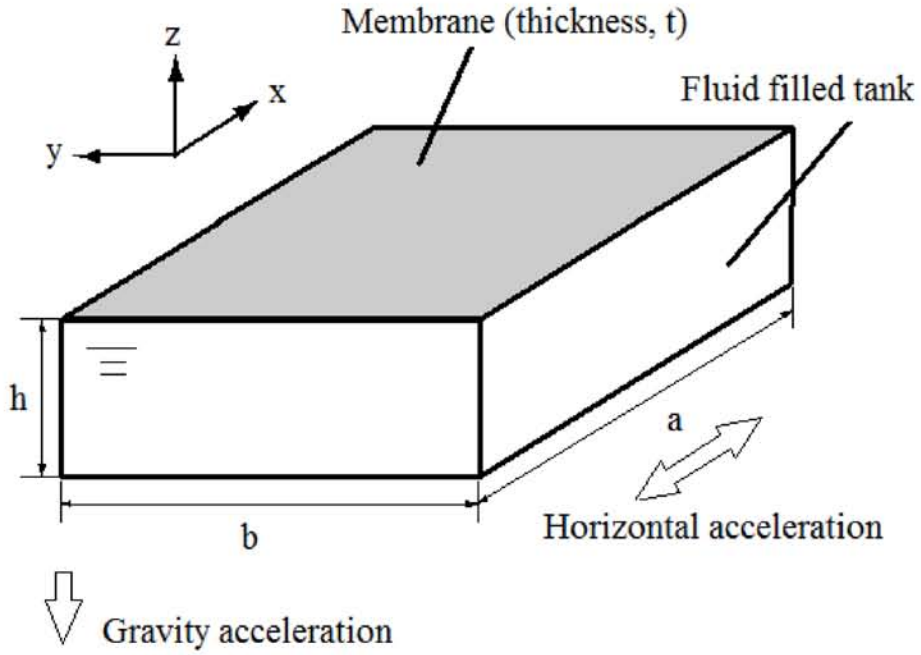

Figure 2.2. 3-D tank which upper surface is covered by membrane.

In our second model, a rectangular tank contains a liquid whose upper and lower surface is covered by a membrane (Fig. 2.3). In this case, the model is vibrated vertically. In the model shown in Fig. 2.2, the effects of gravity are taken into account. In contrast, in the second model (Fig. 2.3), for simplicity, gravity is ignored because in this case the initial conditions nonlinear and the inclusion of gravity would complicate the problem to the extent that it would be difficult to determine the effects of large deformations.

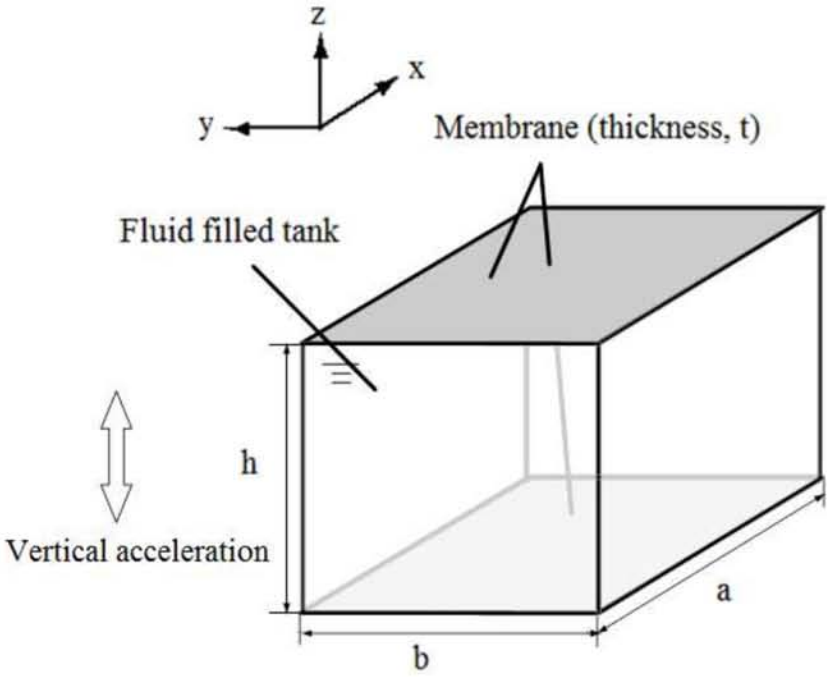

Figure 2.3. 3-D tank which upper and bottom surfaces is covered by membrane.

2.3 Hyperelastic rubberlike material

In this section, the constitutive equations for the incompressible rubberlike material are discussed. The neo-Hookean (Rivlin), Mooney–Rivlin, and Ogden theories are well-known approaches to the constructive equation of rubber. The neo-Hookean and Mooney–Rivlin theories, have limited applicability because the resulting constitutive equations are nonlinear in the high-strain domain. On the other hand, the strain energy function suggested by Ogden provides a generally applicable constitutive equation involving a strain energy function that is polynomial in the stretch rate in the principal direction and is in accord with the experimental results of Treloar up to a stretch rate of 700%. Predictions of the Mooney model are good only for moderate deformation. Indeed, the Mooney predictions become too soft for large deformations, thus introducing important errors (60% of elongation on the right side of the path). On the contrary, predictions given by Ogden models still fit to the experimental data well even for large elongations. Finite

element analysis using Ogden constitutive equations provided results in good agreement with experimental data [50]. Three-term (modified) models are widely used. Besides the material constants mentioned above, Poisson ratio is also required. For most cases, satisfactory results can be obtained by assigning Poisson's ratio from 0.49 to 0.499. The Ogden model is used here for the constitutive equation of the rubberlike material. The Ogden strain energy function W is given in terms of the stretch rate λ_a in the principal direction (a = 1, 2, 3) as follows:

$$W(\lambda_1, \lambda_2, \lambda_3) = \sum_r \frac{\mu_r}{\alpha_r}[{\lambda_1}^{\alpha_r} + {\lambda_2}^{\alpha_r} + {\lambda_3}^{\alpha_r} - 3]. \quad (1)$$

Here μ_r and α_r are material constants determined from experimental data. In this paper, the values from Table 2.1 are used. These parameters are commonly used in other numerical analyses.

Table 2.1 Parameter of Ogden strain energy function

r	$\propto_r$	$\mu_r(\mathrm{kg/m^2})$
1	1.3	62994.7
2	5.0	126.7
3	-2.0	-1001.3

Generally, the second Piola–Kirchhoff (2PK) stress in the principal direction, S_a, is derived by partially differentiating the strain energy function W with respect to the corresponding Green–Lagrange strain, E_a. The relation between E_a and λ_a is

$$(\lambda_a)^2 = 1 + 2E_a, \quad (2)$$

$$\frac{\partial}{\partial E_a} = \lambda_a^{-1}\frac{\partial}{\partial \lambda_a}, \quad (3)$$

and so the 2PK stress in the principal direction is found to be

$$S_a = \frac{\partial W}{\partial E_a} = \lambda_a^{-1}\frac{\partial W}{\partial \lambda_a} = \lambda_a^{-2}\sum_r \mu_r(\lambda_a)^{\alpha_r} + \lambda_a^{-2}p. \quad (4)$$

Lagrange's method of undetermined multipliers gives the following result, because the stress perpendicular to the membrane surface is zero ($S_3 = 0$) owing to the assumption of plane stress:

$$p = -\sum_r \mu_r (\lambda_3)^{\alpha_r} = -\sum_3 \mu_r (\lambda_1 \lambda_2)^{-\alpha_r}. \tag{5}$$

When Eq. (5) is substituted into Eq. (4), the 2PK stress becomes

$$S_a = \lambda_a^{-2} \sum_r \mu_r [{\lambda_a}^{\alpha_r} - (\lambda_1 \lambda_2)^{-\alpha_r}]. \tag{6}$$

Thus, the 2PK stress depends on the initial shape. In this, it is different from the Cauchy stress, which depends on the current shape. Owing to the assumption of incompressibility, the relationship between the 2PK stress in the principal direction and the corresponding Cauchy stress σ_a is as follows:

$$S_a = \frac{1}{\lambda_a^2} \sigma_a. \tag{7}$$

2.4 Strain on a thin membrane

2.4.1 Green–Lagrange strain component

Owing to the assumption of plane stress, the Green–Lagrange strain matrix **E** of the membrane can be represented as follows in a rectangular coordinate system:

$$\mathbf{E} = \begin{bmatrix} E_x & \frac{1}{2}E_{xy} \\ \frac{1}{2}E_{xy} & E_y \end{bmatrix}, \tag{8}$$

$$E_x = \frac{\partial u}{\partial x} + \frac{1}{2}\left\{\left(\frac{\partial u}{\partial x}\right)^2 + \left(\frac{\partial v}{\partial x}\right)^2 + \left(\frac{\partial w}{\partial x}\right)^2\right\} + E_{x0}, \tag{9}$$

$$E_y = \frac{\partial v}{\partial y} + \frac{1}{2}\left\{\left(\frac{\partial u}{\partial y}\right)^2 + \left(\frac{\partial v}{\partial y}\right)^2 + \left(\frac{\partial w}{\partial y}\right)^2\right\} + E_{y0}, \tag{10}$$

$$E_{xy} = \frac{\partial u}{\partial y} + \frac{\partial v}{\partial x} + \left(\frac{\partial u}{\partial x}\frac{\partial u}{\partial y} + \frac{\partial v}{\partial x}\frac{\partial v}{\partial y} + \frac{\partial w}{\partial x}\frac{\partial w}{\partial y}\right), \tag{11}$$

Here E_{x0} and E_{y0} are the initial strains in the x and y directions and $\mathbf{u} = (u, v, w)$ is the displacement vector of the membrane.

2.4.2 Determination of the principal direction

The principal strain $\bar{E}_a$ is required in order to calculate the strain energy of the membrane. The principal direction of the membrane, which varies with time and location, is determined as follows. The principle direction is rotated by an angle θ from the z axis, as shown in Fig. 2.4, and can be represented as follows, using the strain components from Eq. (8) [51]:

$$\theta = \frac{1}{2}\arctan\frac{E_{xy}}{E_x - E_y}. \tag{12}$$

The Green–Lagrange strain matrix in the principal direction, $\bar{\mathbf{E}}$, is then obtained as follows:

$$\bar{\mathbf{E}} = \mathbf{T}\mathbf{E}\mathbf{T}^{\mathrm{T}} = \begin{bmatrix} \bar{E}_1 & 0 \\ 0 & \bar{E}_2 \end{bmatrix}, \tag{13}$$

$$\mathbf{T} = \begin{bmatrix} \cos\theta & \sin\theta \\ -\sin\theta & \cos\theta \end{bmatrix}. \tag{14}$$

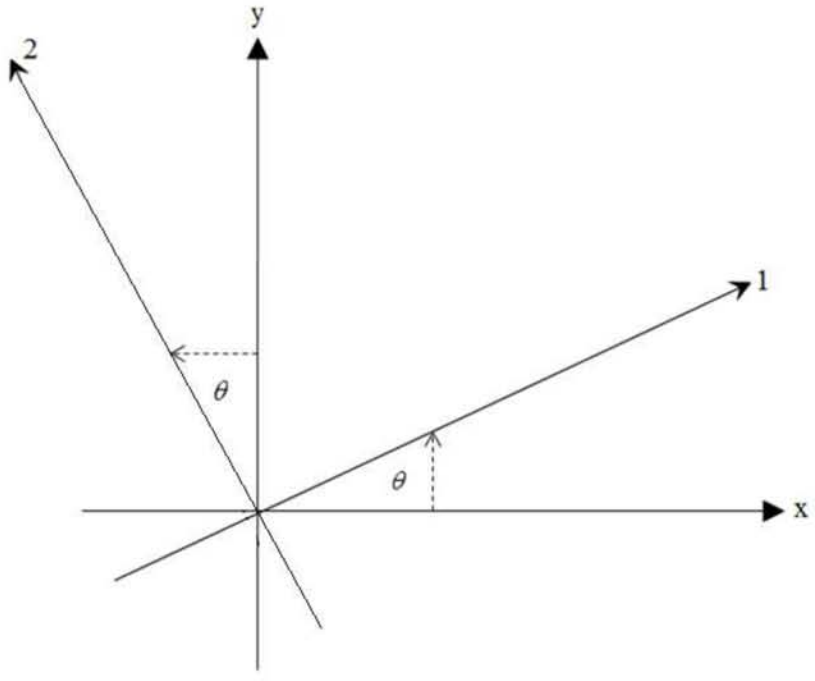

Figure 2.4. x-y axis system and principle direction.

2.5 Variational principle for the liquid–structure interaction problem

In this subsection, the dominant equation is derived from a functional formulation of the liquid–structure interaction problem based on Hamilton's principle [52].

2.5.1 Structural domain

A functional on the structural domain, Π_{solid}, is derived by subtracting the kinetic energy of the membrane and the gravitational potential energy due to acceleration from the strain energy of the membrane:

$$\Pi_{\text{solid}} = \int_{t_1}^{t_2} \left[\int_{\Omega_s} \left\{ W - \frac{1}{2}\rho_m \ddot{\mathbf{u}} \cdot \dot{\mathbf{u}} - \rho_m \mathbf{a} \cdot \mathbf{y}_s \right\} \mathrm{d}\Omega_s \right] \mathrm{d}t, \tag{15}$$

where Ω_s is the structural domain, ρ_m is the density of the membrane, $\mathbf{u}$ is the displacement vector, $\mathbf{y}_s = \mathbf{x}_s + \mathbf{u}$ is the position vector of the current shape, an overdot " $\cdot$ " indicates the time derivative. $\mathbf{a}$ is the acceleration vector of the external force, and, with gravity taken into account and with acceleration in the x direction as shown in Fig. 2.2, it is given by

$$\mathbf{a} = \begin{Bmatrix} A_x \\ 0 \\ -g \end{Bmatrix}. \tag{16}$$

While in the absence of gravity and with acceleration in the z direction as shown in Fig. 2.3, is given by

$$\mathbf{a} = \begin{Bmatrix} 0 \\ 0 \\ A_z \end{Bmatrix}, \tag{17}$$

Here A_x and A_z are the accelerations due to the imposed vibration and g is the acceleration due to gravity.

2.5.2 Liquid domain

A functional on the liquid domain, Π_{liquid}, is derived by subtracting the kinetic energy of the liquid from its potential energy under the assumption that the liquid is incompressible and inviscid.

$$\Pi_{\text{liquid}} = \int_{t_1}^{t_2} \left[\int_{\Omega_l} \left\{ \rho_l \mathbf{a} \cdot \mathbf{y}_l - \frac{1}{2} \rho_l \mathbf{v} \cdot \mathbf{v} \right\} \mathrm{d}\Omega_l \right] \mathrm{d}t. \tag{18}$$

Here Ω_l is the liquid domain, $\mathbf{y}_l$ is the position vector of the current shape, ρ_l is the density of the liquid, and $\mathbf{v}$ is the liquid velocity vector. The equation of continuity and the dynamic boundary condition on the interaction boundary are taken into account using Lagrange's method of undetermined multipliers, and Eq. (18) becomes

$$\Pi_{\text{liquid}} = \int_{t_1}^{t_2} \left[\begin{array}{c} \int_{\Omega_l} \left\{ \rho_l \mathbf{a} \cdot \mathbf{y}_l - \frac{1}{2} \rho_l \mathbf{v} \cdot \mathbf{v} - \lambda_1 \nabla \cdot (\rho_l \mathbf{v}) \right\} \mathrm{d}\Omega_l \\ + \int_{\Gamma_{ls}} \lambda_2 (-\dot{\mathbf{u}} \cdot \mathbf{n}_s + \mathbf{v} \cdot \mathbf{n}_l) \mathrm{d}\Gamma_{ls} \end{array} \right] \mathrm{d}t. \tag{19}$$

Here Γ_{ls} is the liquid–structure boundary, λ_i is the Lagrange undetermined multiplier, and $\mathbf{n}_s$ and $\mathbf{n}_l$ are the normal vectors on the structure and liquid boundaries, respectively. Variation of the functional with respect to $\mathbf{v}$ using partial integration and Gauss's theorem, taking account of the incompressibility of the liquid, gives the following:

$$\begin{cases} -\rho_l \mathbf{v} + \rho_l \nabla \lambda_1 = 0 & \text{in } \Omega_l, \\ \lambda_2 = \lambda_1 \rho_l & \text{on } \Gamma_{ls}. \end{cases} \tag{20}$$

Taking λ_1 from Eq. (20) as the velocity potential and using it in Eq. (19) gives

$$\Pi_{\text{liquid}} = \int_{t_1}^{t_2} \left[\begin{array}{c} \int_{\Omega_l} \left\{ \rho_l \mathbf{a} \cdot \mathbf{y}_l - \frac{1}{2} \rho_l \mathbf{v} \cdot \mathbf{v} - \phi \nabla \cdot (\rho_l \mathbf{v}) \right\} \mathrm{d}\Omega_l \\ + \int_{\Gamma_{ls}} \rho_l \phi (-\dot{\mathbf{u}} \cdot \mathbf{n}_s + \mathbf{v} \cdot \mathbf{n}_l) \mathrm{d}\Gamma_{ls} \end{array} \right] \mathrm{d}t. \tag{21}$$

The following equation results from the equality between the increments in volume per unit time in the structure–liquid interaction domain and the liquid domain:

$$\int_{\Gamma_{ls}} \dot{\mathbf{u}} \cdot \mathbf{n}_s \mathrm{d}\Gamma_{ls} = \int_{\Omega_l} \mathrm{d}\Omega_l', \tag{22}$$

where the prime " ′ " indicates the time derivative. Applying Gauss's theorem to the boundary integral term of Eq. (21) and taking Eq. (22) into account gives the following equation:

$$\Pi_{\text{liquid}} = \int_{t_1}^{t_2} \left[\begin{array}{c} \int_{\Omega_l} \left\{ \rho_l \mathbf{a} \cdot \mathbf{y}_l - \frac{1}{2} \rho_l \mathbf{v} \cdot \mathbf{v} - \rho_l \phi \nabla^2 \phi \right\} \mathrm{d}\Omega_l \\ - \int_{\Omega_l} \rho_l \phi \mathrm{d}\Omega_l' + \int_{\Omega_l} \rho_l \nabla \cdot (\phi \nabla \phi) \mathrm{d}\Omega_l \end{array} \right] \mathrm{d}t. \tag{23}$$

Using the formula for the derivative of a product gives the following expression:

$$\Pi_{\text{liquid}} = \int_{t_1}^{t_2} \left[\int_{\Omega_l} \pi_l \mathrm{d}\Omega_l \right] \mathrm{d}t, \tag{24}$$

where

$$\pi_l \equiv \frac{1}{2}\rho_l \nabla\phi \cdot \nabla\phi + \rho_l \phi' + \rho_l \mathbf{a} \cdot \mathbf{y}_l. \tag{25}$$

Here ϕ has the physical meaning of the liquid velocity potential and the " $'$ " indicates the time derivative.

2.5.3 Liquid–structure interaction problem

The functional for the liquid–structure interaction problem is as the sum of the expressions in Eq. (24) and Eq. (15):

$$\Pi_{\text{liquid+solid}} = \int_{t_1}^{t_2} \left[\begin{array}{l} \displaystyle\int_{\Omega_s} \left\{ W - \frac{1}{2}\rho_m \ddot{\mathbf{u}} \cdot \dot{\mathbf{u}} - \rho_m \mathbf{a} \cdot \mathbf{y}_s \right\} \mathrm{d}\Omega_s \\ \displaystyle + \int_{\Omega_l} \left\{ \frac{1}{2}\rho_l \nabla\phi \cdot \nabla\phi + \rho_l \phi' + \rho_l \mathbf{a} \cdot \mathbf{y}_l \right\} \mathrm{d}\Omega_l \end{array} \right] \mathrm{d}t, \tag{26}$$

The first-variation equation is zero owing to the stationarity of the functional (note that the increment in the liquid domain, $\mathrm{d}\Omega_l$, varies because the boundary of the liquid domain changes as the membrane deforms):

$$\delta\Pi_{\text{liquid+solid}} = \int_{t_1}^{t_2} \left[\begin{array}{c} \displaystyle\int_{\Omega_s} \{\delta\bar{\mathbf{E}}^{\mathrm{T}} \bar{\mathbf{S}} - \rho_m \delta\mathbf{u}^{\mathrm{T}} \mathbf{a} + \rho_m \delta\mathbf{u}^{\mathrm{T}} \ddot{\mathbf{u}}\} \mathrm{d}\Omega_s \\ \displaystyle + \int_{\Omega_l} \rho_l \nabla\delta\phi \cdot \nabla\phi \, \mathrm{d}\Omega_f - \\ \displaystyle\int_{\Gamma_{ls}} \rho_f \dot{\mathbf{u}} \cdot \mathbf{n}_s \delta\phi \, \mathrm{d}\Gamma_{ls} + \int_{\Gamma_{ls}} \delta\mathbf{u}^{\mathrm{T}} \pi_l \mathbf{n}_l \, \mathrm{d}\Gamma_{ls} \end{array} \right] \mathrm{d}t = 0. \tag{27}$$

Here $\bar{\mathbf{E}}$ and $\bar{\mathbf{S}}$ are the Green–Lagrange strain in the principal direction and the 2PK stress, respectively. This equation can be rewritten as follows:

$$\delta\Pi_{\text{liquid+solid}} = \int_{t_1}^{t_2} \begin{bmatrix} \delta\mathbf{u}^{\mathrm{T}} \int_{\Omega_s} (\rho_m \ddot{\mathbf{u}} - \rho_m \mathbf{a} - \nabla \mathbf{t}) \mathrm{d}\Omega_s \\ -\delta\phi \int_{\Omega_l} \rho_l \nabla \cdot \nabla\phi \, \mathrm{d}\Omega_l \\ +\delta\mathbf{u}^{\mathrm{T}} \int_{\Gamma_{ls}} \left(\tilde{\mathbf{T}} \cdot \mathbf{n}_s + \pi_l \mathbf{n}_l\right) \mathrm{d}\Gamma_{ls} \\ +\delta\phi \int_{\Gamma_{ls}} \rho_l (-\dot{\mathbf{u}} \cdot \mathbf{n}_s + \nabla\phi \cdot \mathbf{n}_l) \, \mathrm{d}\Gamma_{ls} \end{bmatrix} \mathrm{d}t = 0. \tag{28}$$

Here $\tilde{\mathbf{T}}$ represents the surface forces on the structure and $\mathbf{t}$ the internal force imparting stress on the body. Because $\delta\mathbf{u}$ and $\delta\phi$ are arbitrary, Eq. (28) leads to the following dominant equations:

$$\rho_m \ddot{\mathbf{u}} - \rho_m \mathbf{a} - \nabla \mathbf{t} = 0 \quad \text{in } \Omega_s, \tag{29}$$

$$\nabla \cdot \nabla\phi = 0 \quad \text{in } \Omega_l, \tag{30}$$

$$\tilde{\mathbf{T}} \cdot \mathbf{n}_s + \pi_l \mathbf{n}_l = 0 \quad \text{on } \Gamma_{ls}, \tag{31}$$

$$\dot{\mathbf{u}} \cdot \mathbf{n}_s = \nabla\phi \cdot \mathbf{n}_l \quad \text{on } \Gamma_{ls}, \tag{32}$$

where T, $\mathbf{n}_s$, and $\mathbf{n}_l$ are the internal stress in the structure, the unit normal vector to the membrane surface, and the unit normal vector to the liquid boundary, respectively. Equations (29), (30), (31), and (32) are the equilibrium equation of the structural domain, the equation of continuity, the dynamic boundary condition representing equilibrium of forces, and the geometric boundary condition representing the kinematic condition on the structure–liquid boundary, respectively.

2.6 Arbitrary Lagrangian–Eulerian (ALE)

A summary of the ALE method is given in this section and it applied to the dominant equation derived in Section 2.5 in accordance with the Nitikitpaiboon-Bathe method [42].

2.6.1 Outline of ALE method

Lagrangian descriptions are mainly used in structural dynamics because they allow easy tracking of free surfaces and interfaces between different materials. However, they cannot follow large displacements of the computational domain without recourse to frequent remeshing operations. On the other hand, Eulerian descriptions are widely used in fluid dynamics. The computational mesh is fixed and the continuum moves with respect to the grid and the large displacements in the continuum motion can be handled-but often at the expense of accurate interface definition and flow resolution of flow. The ALE system combines these two descriptions. The mesh deforms, but it does not need to follow the motion of the material points.

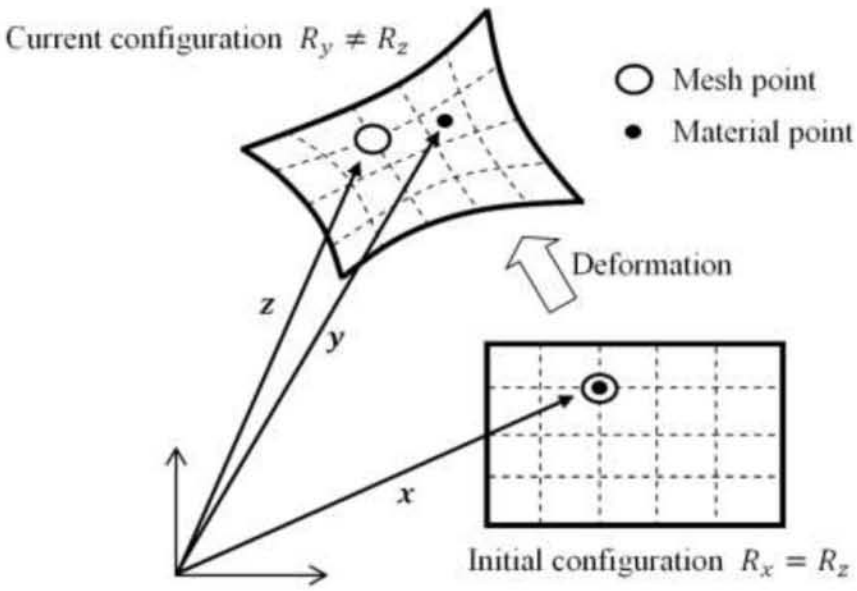

Figure 2.5. ALE coordinate system

An outline of the ALE coordinate system is shown in Fig. 5. R_x is the initial position of the body, R_y is the current position, and $\mathbf{x} \in R_x$, $\mathbf{y} \in R_y$ are the coordinates of the respective material points. The coordinate of the material point at the current position is a function of the initial position as follows:

$$\mathbf{y} = \tilde{\mathbf{y}}(\mathbf{x}, t). \tag{33}$$

Here $\mathbf{z} \in R_z$ is defined by the mesh. It is assumed that the initial positions of the body and mesh are the same and also match the boundary surface at the current position. The relationship between $\mathbf{y}$ and $\mathbf{z}$ is written as follows:

$$\mathbf{y} = \hat{\mathbf{y}}(\mathbf{z}, t). \tag{34}$$

If some physical quantity f is expressed in the Eulerian coordinate system, it is written as follows as a function of the current coordinate $\mathbf{y}$:

$$f = \bar{f}(\mathbf{y}, t). \tag{35}$$

In the case of a Lagrangian coordinate system, it is written as follows with reference to the initial coordinate $\mathbf{x}$:

$$f = \bar{f}(\tilde{\mathbf{y}}(\mathbf{x}, t), t) = \tilde{f}(\mathbf{x}, t). \tag{36}$$

It is also written as follows with reference to the mesh coordinate $\mathbf{z}$: .

$$f = \bar{f}(\hat{\mathbf{y}}(\mathbf{z}, t), t) = \hat{f}(\mathbf{z}, t). \tag{37}$$

In the ALE coordinate system, the physical quantity f is evaluated with reference to the mesh coordinate $\mathbf{z}$. Next, the time derivatives are taken in each coordinate system and the relationships between them are given. In the Eulerian coordinate system, the time derivative is taken at a fixed point in space. This is called space–time differentiation and is written as follows:

$$f' = \frac{\partial}{\partial t}\bar{f}(\mathbf{y}, t)|_{\mathbf{y}\ \text{fixed}}. \tag{38}$$

On the other hand, in the Lagrangian coordinate system, the time derivative is taken at a fixed material point. This is called material time differentiation and is written as follows:

$$\dot{f} = \frac{\partial}{\partial t}\tilde{f}(\mathbf{x}, t)|_{\mathbf{x}\ \text{fixed}}. \tag{39}$$

In the ALE coordinate system, the time derivative is taken at a fixed mesh point and is written as follows:

$$f^* = \frac{\partial}{\partial t}\hat{f}(\mathbf{z},t)|_{\mathbf{z}\text{ fixed}}. \tag{40}$$

The velocity of a material point is $\mathbf{v}^p = \partial\tilde{\mathbf{y}}/\partial t$, and $\dot{f}$ is written as follows in the Eulerian coordinate system:

$$\begin{aligned}\dot{f} &= \frac{\bar{f}(\mathbf{y}+\mathbf{v}^p\Delta t, t+\Delta t)|_{\mathbf{y}\text{ fixed}} - \bar{f}(\mathbf{y},t)|_{\mathbf{y}\text{ fixed}}}{\Delta t} \\ &= \frac{\partial}{\partial t}\bar{f}(\mathbf{y},t)|_{\mathbf{y}\text{ fixed}} + \nabla\bar{f}\cdot\mathbf{v}^p \\ &= f' + \nabla\bar{f}\cdot\mathbf{v}^p. \end{aligned} \tag{41}$$

When the material time derivative is represented in the Eulerian coordinate system in this way, a convection term $\nabla\bar{f}\cdot\mathbf{v}^p$ appears because it is not the same material point that is observed as time passes. Similarly, the velocity of the mesh is $\mathbf{v}^m = \partial\hat{\mathbf{y}}/\partial t$, and f^* is written as follows in the Eulerian coordinate system:

$$f^* = f' + \nabla\bar{f}\cdot\mathbf{v}^m. \tag{42}$$

If the motions of the mesh and the material point are the same $(\mathbf{v}^m = \mathbf{v}^p)$, then the expression in Eq. (42) is equivalent to the material time derivative, while if the mesh is fixed in space $(\mathbf{v}^m = 0)$, it is equivalent to the space–time derivative. The mesh coordinate $\hat{\mathbf{y}}$ is defined by the mesh control rule and is normally different from both the Eulerian and Lagrangian coordinates.

2.6.2 Dominant equation of the ALE method

Using Eq. (42), the Eulerian governing equation for the liquid from Section 3.3.3 is replaced. We assume that the structure mesh agrees with the liquid mesh on its boundary.

Substituting Eq. (27) into Eqs. (29)–(32), the ALE governing equations for the structure and the current liquid domain are obtained as follows:

$$\nabla\cdot\nabla\phi = 0 \quad \text{in} \quad \Omega_l \tag{43}$$

$$\mathbf{T}\cdot\mathbf{n}_s + \pi'_l\mathbf{n}_l = 0 \quad \text{on} \quad \Gamma_{ls}, \tag{44}$$

$$v_n = \frac{\partial \phi}{\partial n} \quad \text{on} \quad \Gamma_{ls}, \tag{45}$$

$$t = 0 \quad \text{in} \quad \Omega_s, \tag{46}$$

Where

$$\pi'_l \equiv \frac{1}{2}\rho_l(\nabla\phi)^2 + \rho_l f + \rho_l \frac{\partial \phi}{\partial t}\Big|_{\mathbf{z}\ \text{fixed}} - \rho_l \mathbf{v}^m \cdot \frac{\partial \phi}{\partial \mathbf{x}}. \tag{47}$$

The last term in Eq. (47) is the major change from the Eulerian formulation. Thus, the weak form of the above equation is

$$\int_{t_1}^{t_2} \left[\begin{array}{c} \int_{\Omega_s} \delta\mathbf{e} \cdot \mathbf{s} \mathrm{d}\Omega_s - \int_{\Gamma_{ls}} \pi'_l \delta u_n \mathrm{d}\Gamma_{ls} \\ + \int_{\Omega_l} \rho_l \nabla\delta\phi \cdot \nabla\phi \mathrm{d}\Omega_l - \int_{\Gamma_{ls}} \rho_l \delta\phi {v_n}^m \mathrm{d}\Gamma_{ls} \end{array} \right] \mathrm{d}t = 0. \tag{48}$$

For this equation to be applicable, the mesh displacement velocity $\dot{\hat{\mathbf{u}}}$ must satisfy the following condition on the structure–liquid boundary:

$$\dot{\mathbf{u}} \cdot \mathbf{n}_s = \dot{\hat{\mathbf{u}}} \cdot \mathbf{n}_l \quad \text{on} \quad T_{ls}. \tag{49}$$

If the surface of the liquid is covered by the structure, Eq. (49) can be solved by using the ALE coordinate system in the liquid domain. Thus, if the shape functions of the structure and liquid on the structure–liquid boundary are the same, Eq. (49) is satisfied. If the ALE coordinates system is used for the weak form of the dominant equation (27) in the liquid domain and on the structure–liquid boundary, then, taking account of Eqs. (49) and (32), the following equation is found:

$$\delta\Pi_{\text{liquid+solid}} = \int_{t_1}^{t_2} \left[\begin{array}{c} \int_{\Omega_s} \{\delta\bar{\mathbf{E}}^{\mathrm{T}}\bar{\mathbf{S}} - \rho_m \delta\mathbf{u}^{\mathrm{T}}\mathbf{a} + \rho_m \delta\mathbf{u}^{\mathrm{T}}\ddot{\mathbf{u}}\} \mathrm{d}\Omega_s \\ + \int_{\Omega_l} \rho_l \nabla\delta\phi \cdot \nabla\phi \, \mathrm{d}\Omega_l \\ - \int_{\Gamma_{ls}} \rho_l \dot{\hat{\mathbf{u}}}\,|_{\mathbf{x}\ \text{fixed}} \cdot \mathbf{n}_l \delta\phi \, \mathrm{d}\Gamma_{ls} \\ + \int_{\Gamma_{ls}} \delta\mathbf{u}^{\mathrm{T}} {\pi_l}^* \mathbf{n}_l \, \mathrm{d}\Gamma_{ls} \end{array} \right] \mathrm{d}t = 0, \tag{50}$$

$$\pi_l^* = \frac{1}{2}\rho_l \nabla\phi \cdot \nabla\phi + \rho_l \mathbf{a} \cdot \mathbf{y}_l + \rho_l \left(\phi^* - \dot{\hat{\mathbf{u}}} \cdot \frac{\partial \phi}{\partial \mathbf{y}_l}\right), \tag{51}$$

where $\mathbf{y}_l = \hat{\mathbf{x}} + \hat{\mathbf{u}}$ is defined in ALE coordinates. π_l^* denotes the value in the ALE coordinate system of the space–time derivative of π_l.

2.6.3 Mesh updating

In this work, a Lagrangian coordinate system is used in the structural domain and an ALE coordinate system in the liquid domain. The mesh control rule in the liquid domain is defined for each analytical model. In the following, $\boldsymbol{h}$ denotes tank depth and $\hat{\mathbf{x}} = (\hat{x}, \hat{y}, \hat{z})$ denotes the initial coordinate in the liquid domain. The mesh displacement $\hat{\mathbf{u}}$ is linearly controlled such that $\hat{\mathbf{u}} = \mathbf{u}$ on the liquid–structure boundary and $\hat{\mathbf{u}} = 0$ at the bottom of the tank, as shown in Fig. 2.6.

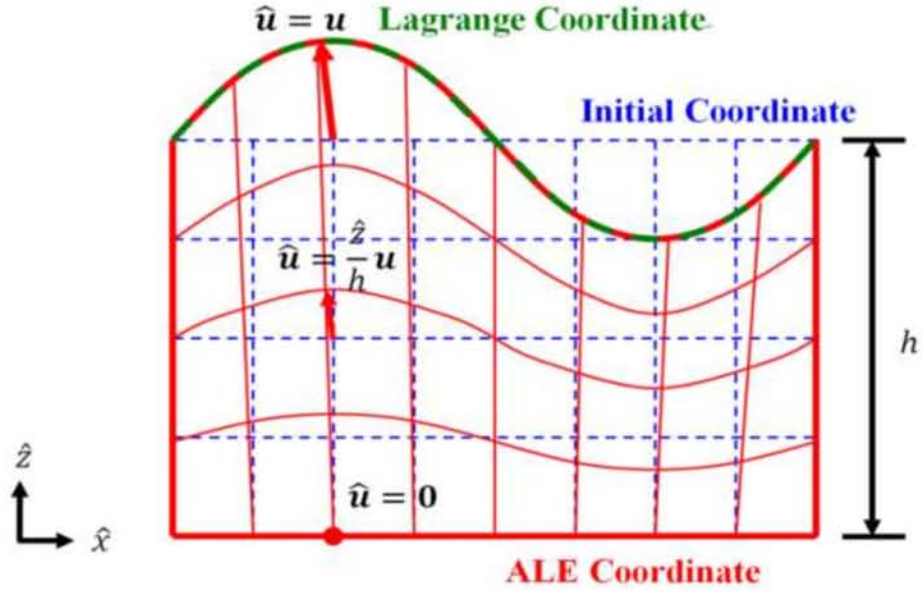

Figure 2.6. Mesh control rule.

For the rectangular tank containing a liquid whose upper surface is covered by a membrane as shown in Fig. 2.2, a Lagrangian coordinate system is used in the liquid–structure system., Close to the bottom of the tank, this become close to an Eulerian coordinate system, and thus $\hat{\mathbf{u}}$ is controlled such that $\hat{\mathbf{u}} = (\hat{z}/h)\,\mathbf{u}$ in the liquid domain.

Therefore, the following equation is included in the finite element analysis:

$$\int_{\Omega_l} \rho_l \left(\hat{\mathbf{u}} - \frac{\hat{z}}{h} \mathbf{u} \right) \cdot \delta \hat{\mathbf{u}} \mathrm{d}\Omega_l = 0. \tag{52}$$

In the rectangular tank containing a liquid whose upper and lower surfaces are covered by membranes shown in Fig. 2.3, $\mathbf{u}_u$ denotes the upper membrane displacement and $\boldsymbol{u}_l$ the lower membrane displacement. $\hat{\mathbf{u}}$ is linearly controlled such that $\hat{\mathbf{u}} = \mathbf{u}_u$ on the upper structure–liquid boundary and $\hat{\mathbf{u}} = \mathbf{u}_l$ on the lower structure–liquid boundary. This can be expressed as follows:

$$\int_{\Omega_l} \rho_l \left\{ \hat{\mathbf{u}} - \left(\mathbf{u}_l + \frac{\hat{z}}{h} (\mathbf{u}_u - \mathbf{u}_l) \right) \right\} \cdot \delta \hat{\mathbf{u}} \mathrm{d}\Omega_l = 0. \tag{53}$$

Although this is a simple control rule, it is sufficient to prevent distortion of the mesh, because for structural deformations in these models, the z direction is dominant.

2.7 Dealing with the time-derivative term (Newmark-β method)

The Newmark-β method, which is an implicit method, is applied to deal with the time-derivative term in the dominant equation. According to this method, when the displacement, velocity, and acceleration are known at time t, the displacement and velocity at time $t + \Delta t$ are written as follows:

$${}^{t+\Delta t}\mathbf{u} = {}^{t}\mathbf{u} + \Delta t \, {}^{t}\dot{\mathbf{u}} + \frac{(\Delta t)^2}{2} \left\{ (1 - 2\beta_N) \, {}^{t}\ddot{\mathbf{u}} + 2\beta_N \, {}^{t+\Delta t}\ddot{\mathbf{u}} \right\}, \tag{54}$$

$${}^{t+\Delta t}\dot{\mathbf{u}} = {}^{t}\dot{\mathbf{u}} + \Delta t \left\{ (1 - \gamma_N) \, {}^{t}\ddot{\mathbf{u}} + \gamma_N \, {}^{t+\Delta t}\ddot{\mathbf{u}} \right\}. \tag{55}$$

Here β_N and γ_N are the parameters of the Newmark-β method and are taken to have the values $\beta_N = 0.25$ and $\gamma_N = 0.5$ in this work. Equations (54) and (55) can be rewritten as follows:

$$\begin{aligned} {}^{t+\Delta t}\ddot{\mathbf{u}} &= \left(1 - \frac{1}{2\beta_N} \right) {}^{t}\ddot{\mathbf{u}} - \frac{1}{\beta_N \Delta t} \, {}^{t}\dot{\mathbf{u}} + \frac{1}{\beta_N (\Delta t)^2} \left({}^{t+\Delta t}\mathbf{u} - {}^{t}\mathbf{u} \right) \\ &= {}^{t+\Delta t}\tilde{\ddot{\mathbf{u}}} + \frac{1}{\beta_N (\Delta t)^2} \, {}^{t+\Delta t}\mathbf{u}, \end{aligned} \tag{56}$$

$$
\begin{aligned}
{}^{t+\Delta t}\dot{\mathbf{u}} &= \left(1-\frac{\gamma_N}{2\beta_N}\right)\Delta t\ {}^{t}\ddot{\mathbf{u}} + \left(1-\frac{\gamma_N}{\beta_N}\right)\ {}^{t}\dot{\mathbf{u}} + \frac{\gamma_N}{\beta_N \Delta t}\left({}^{t+\Delta t}\mathbf{u} - \ {}^{t}\mathbf{u}\right) \\
&= {}^{t+\Delta t}\tilde{\dot{\mathbf{u}}} + \frac{\gamma_N}{\beta_N \Delta t}\ {}^{t+\Delta t}\mathbf{u}. \qquad (57)
\end{aligned}
$$

When ${}^{t+\Delta t}\tilde{\ddot{\mathbf{u}}}$ and ${}^{t+\Delta t}\tilde{\dot{\mathbf{u}}}$ are considered together at time t, they are called a predictor. The weak form of the dominant equation is written as follows at the time $t+\Delta t$ by using Eqs. (56) and (57):

$$
\delta \Pi_{\text{liquid+solid}} = \int_{t_1}^{t_2} \left[\begin{array}{c} \int_{\Omega_s} \left\{ \begin{array}{c} \delta \bar{\mathbf{E}}^{\mathrm{T}} \bar{\mathbf{S}} - \rho_m \delta \mathbf{u}^{\mathrm{T}} \mathbf{a} \\ + \rho_m \delta \mathbf{u}^{\mathrm{T}} \left(\tilde{\ddot{\mathbf{u}}} + \dfrac{1}{\beta_N (\Delta t)^2} \mathbf{u} \right) \end{array} \right\} \mathrm{d}\Omega_s \\ + \int_{\Omega_l} \rho_l \nabla \delta\phi \cdot \nabla \phi \ \mathrm{d}\Omega_l - \\ \int_{\Gamma_{ls}} \rho_l \left(\tilde{\dot{\hat{\mathbf{u}}}} + \dfrac{\gamma_N}{\beta_N \Delta t} \hat{\mathbf{u}} \right) \mathbf{n}_l \delta\phi \ \mathrm{d}\Gamma_{ls} \\ + \int_{\Gamma_{ls}} \delta \mathbf{u}^{\mathrm{T}} {\pi_l}^{*\prime} \mathbf{n}_l \ \mathrm{d}\Gamma_{ls} \end{array} \right] \mathrm{d}t = 0, \qquad (58)
$$

$$
{\pi_l}^{*\prime} = \frac{1}{2}\rho_l \nabla\phi \cdot \nabla\phi + \rho_l \mathbf{a} \cdot \mathbf{y}_l + \rho_l \left\{ \begin{array}{c} \left(\widetilde{\phi^*} + \dfrac{\gamma_N}{\beta_N \Delta t} \phi \right) \\ - \left(\tilde{\dot{\hat{\mathbf{u}}}} + \dfrac{\gamma_N}{\beta_N \Delta t} \hat{\mathbf{u}} \right) \cdot \dfrac{\partial \phi}{\partial \mathbf{y}_l} \end{array} \right\}, \qquad (59)
$$

$$
\tilde{\ddot{\mathbf{u}}} = \left(1-\frac{1}{2\beta_N}\right)\ {}^{t}\ddot{\mathbf{u}} - \frac{1}{\beta_N \Delta t}\ {}^{t}\dot{\mathbf{u}} - \frac{1}{\beta_N (\Delta t)^2}\ {}^{t}\mathbf{u}, \qquad (60)
$$

$$
\tilde{\dot{\hat{\mathbf{u}}}} = \left(1-\frac{\gamma_N}{2\beta_N}\right)\Delta t\ {}^{t}\ddot{\hat{\mathbf{u}}} + \left(1-\frac{\gamma_N}{\beta_N}\right)\ {}^{t}\dot{\hat{\mathbf{u}}} - \frac{\gamma_N}{\beta_N \Delta t}\ {}^{t}\hat{\mathbf{u}}, \qquad (61)
$$

$$
\widetilde{\phi^*} = \left(1-\frac{\gamma_N}{2\beta_N}\right)\Delta t\ {}^{t}\phi^{**} + \left(1-\frac{\gamma_N}{\beta_N}\right)\ {}^{t}\phi^{*} - \frac{\gamma_N}{\beta_N \Delta t}\ {}^{t}\phi. \qquad (62)
$$

Here $\tilde{\ddot{\mathbf{u}}}$, $\tilde{\dot{\hat{\mathbf{u}}}}$, and $\widetilde{\phi^*}$ comprise the predictor, and ${\pi_l}^{*\prime}$ denotes the value in the ALE coordinate system of the result of applying the Newmark-β method to ${\pi_l}^{*}$.

2.8 Application to FEM

The weak form of the dominant equation (50) and the mesh control rules in the liquid domain given by Eqs. (52) and (53) are discretized using the FEM, which is applied to both the structural domain and the liquid domain.

2.8.1 FEM in the structural domain

The displacement $\mathbf{u}$ and the initial coordinate $\mathbf{x}_s$ in the structural domain are discretized as follow by using the eight nodal isoperimetric elements shown in Fig. 2.7:

$$\mathbf{x}_s = \mathbf{HX}, \tag{63}$$

$$\mathbf{u} = \mathbf{HU}, \tag{64}$$

where $\mathbf{H}$ is the shape function, and $\mathbf{X} = X_i$ and $\mathbf{U} = U_i$ are the nodal coordinate and nodal displacement at node i. The shape function is represented in a local coordinate system that is normalized as $-1 \leq \xi \leq 1, \quad -1 \leq \eta \leq 1$ to simplify the numerical integral:

$$\mathbf{H} = \begin{bmatrix} H_1 & 0 & 0 & H_2 & 0 & 0 & \cdots & H_8 & 0 & 0 \\ 0 & H_1 & 0 & 0 & H_2 & 0 & \cdots & 0 & H_8 & 0 \\ 0 & 0 & H_1 & 0 & 0 & H_2 & \cdots & 0 & 0 & H_8 \end{bmatrix}, \tag{65}$$

$$H_1 = 0.25 \times (1-\xi)(1-\eta)(-1-\xi-\eta),$$

$$H_2 = 0.25 \times (1+\xi)(1-\eta)(-1+\xi-\eta),$$

$$H_3 = 0.25 \times (1+\xi)(1+\eta)(-1+\xi+\eta),$$

$$H_4 = 0.25 \times (1-\xi)(1+\eta)(-1-\xi+\eta),$$

$$H_5 = 0.50 \times (1-\eta)(1-\xi^2),$$

$$H_6 = 0.50 \times (1+\xi)(1-\eta^2),$$

$$H_7 = 0.50 \times (1+\eta)(1-\xi^2),$$

$$H_8 = 0.50 \times (1-\xi)(1-\eta^2),$$

$$\mathbf{X}^{\mathrm{T}} = \lfloor X_1 \quad Y_1 \quad Z_1 \quad X_2 \quad Y_2 \quad Z_2 \quad \cdots \quad X_8 \quad Y_8 \quad Z_8 \rfloor, \tag{66}$$

$$\mathbf{U}^{\mathrm{T}} = \lfloor U_1 \quad V_1 \quad W_1 \quad U_2 \quad V_2 \quad W_2 \quad \cdots \quad U_8 \quad V_8 \quad W_8 \rfloor. \tag{67}$$

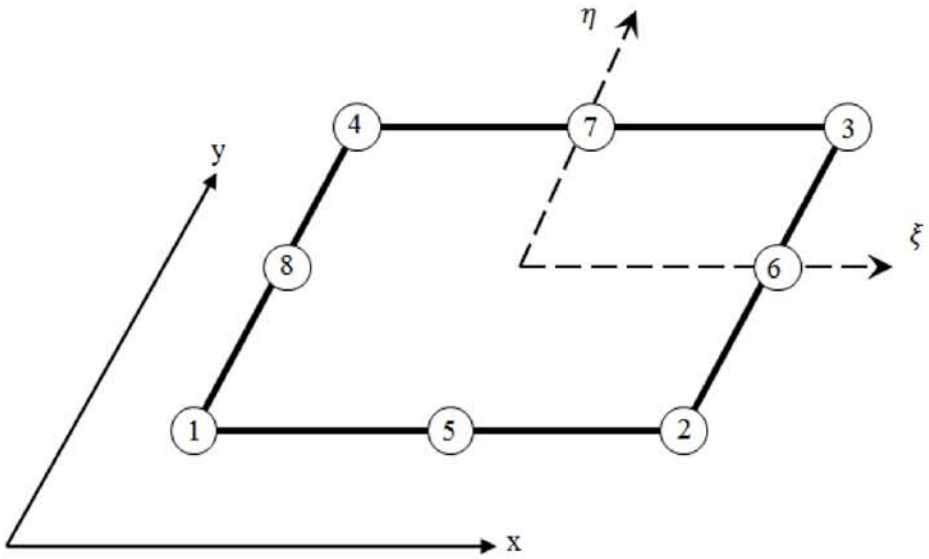

Figure 2.7. 8 nodal isoperimetric element (the number indicate nodal number).

2.8.2 FEM in the liquid domain

The velocity potential ϕ is discretized using the 20 nodal isoparametric elements shown in Fig. 2.8. The mesh displacement $\hat{\mathbf{u}}$ and mesh initial coordinate $\hat{\mathbf{x}}$ are discretized using the 16 nodal isoperimetric elements shown in Fig. 2.9. They are expressed as follows:

$$\phi = \mathbf{h}\boldsymbol{\varphi}, \tag{68}$$

$$\hat{\mathbf{u}} = \hat{\mathbf{H}}\hat{\mathbf{U}}, \tag{69}$$

$$\hat{\mathbf{x}} = \hat{\mathbf{H}}\hat{\mathbf{X}}, \tag{70}$$

where $\mathbf{h}$ and $\hat{\mathbf{H}}$ are the shape functions, and $\boldsymbol{\varphi} = \varphi_i$, $\hat{\mathbf{U}} = \hat{U}_i$, and $\hat{\mathbf{X}} = \hat{X}_i$ are the nodal velocity potential, nodal displacement, and nodal coordinate at node i. The shape functions are represented in a local coordinate system that is normalized as $-1 \le \xi \le 1$, $-1 \le \eta \le 1$, $-1 \le \zeta \le 1$:

$$\mathbf{h} = [h_1 \quad h_2 \quad \cdots \quad h_{20}], \tag{71}$$

$$h_1 = 0.125 \times (1-\xi)(1-\eta)(1-\zeta)(-2-\xi-\eta-\zeta),$$

$$h_2 = 0.25 \times (1-\xi^2)(1-\eta)(1-\zeta),$$

$$h_3 = 0.125 \times (1+\xi)(1-\eta)(1-\zeta)(-2+\xi-\eta-\zeta),$$

$$h_4 = 0.25 \times (1+\xi)(1-\eta^2)(1-\zeta),$$

$$h_5 = 0.125 \times (1+\xi)(1+\eta)(1-\zeta)(-2+\xi+\eta-\zeta),$$

$$h_6 = 0.25 \times (1-\xi^2)(1+\eta)(1-\zeta),$$

$$h_7 = 0.125 \times (1-\xi)(1+\eta)(1-\zeta)(-2-\xi+\eta-\zeta),$$

$$h_8 = 0.25 \times (1-\xi)(1-\eta^2)(1-\zeta),$$

$$h_9 = 0.125 \times (1-\xi)(1-\eta)(1+\zeta)(-2-\xi-\eta+\zeta),$$

$$h_{10} = 0.25 \times (1-\xi^2)(1-\eta)(1+\zeta),$$

$$h_{11} = 0.125 \times (1+\xi)(1-\eta)(1+\zeta)(-2+\xi-\eta+\zeta),$$

$$h_{12} = 0.25 \times (1+\xi)(1-\eta^2)(1+\zeta),$$

$$h_{13} = 0.125 \times (1+\xi)(1+\eta)(1+\zeta)(-2+\xi+\eta+\zeta),$$

$$h_{14} = 0.25 \times (1-\xi^2)(1+\eta)(1+\zeta),$$

$$h_{15} = 0.125 \times (1-\xi)(1+\eta)(1+\zeta)(-2-\xi+\eta+\zeta),$$

$$h_{16} = 0.25 \times (1-\xi)(1-\eta^2)(1+\zeta),$$

$$h_{17} = 0.25 \times (1-\xi)(1-\eta)(1-\zeta^2),$$

$$h_{18} = 0.25 \times (1+\xi)(1-\eta)(1-\zeta^2),$$

$$h_{19} = 0.25 \times (1+\xi)(1+\eta)(1-\zeta^2),$$

$$h_{20} = 0.25 \times (1-\xi)(1+\eta)(1-\zeta^2),$$

$$\widehat{\mathbf{H}} = \begin{bmatrix} \widehat{H}_1 & 0 & 0 & \widehat{H}_2 & 0 & 0 & \cdots & \widehat{H}_{16} & 0 & 0 \\ 0 & \widehat{H}_1 & 0 & 0 & \widehat{H}_2 & 0 & \cdots & 0 & \widehat{H}_{16} & 0 \\ 0 & 0 & \widehat{H}_1 & 0 & 0 & \widehat{H}_2 & \cdots & 0 & 0 & \widehat{H}_{16} \end{bmatrix}, \tag{72}$$

$$\widehat{H}_1 = 0.125 \times (1-\xi)(1-\eta)(1-\zeta)(-1-\xi-\eta),$$

$$\widehat{H}_2 = 0.125 \times (1+\xi)(1-\eta)(1-\zeta)(-1+\xi-\eta),$$

$$\widehat{H}_3 = 0.125 \times (1+\xi)(1+\eta)(1-\zeta)(-1+\xi+\eta),$$

$$\widehat{H}_4 = 0.125 \times (1-\xi)(1+\eta)(1-\zeta)(-1-\xi+\eta),$$

$$\widehat{H}_5 = 0.5 \times (1-\xi^2)(1-\eta)(1-\zeta),$$

$$\widehat{H}_6 = 0.5 \times (1+\xi)(1-\eta^2)(1-\zeta),$$

$$\widehat{H}_7 = 0.5 \times (1-\xi^2)(1+\eta)(1-\zeta),$$

$$\widehat{H}_8 = 0.5 \times (1-\xi)(1-\eta^2)(1-\zeta),$$

$$\widehat{H}_9 = 0.125 \times (1-\xi)(1-\eta)(1+\zeta)(-1-\xi-\eta),$$

$$\widehat{H}_{10} = 0.125 \times (1+\xi)(1-\eta)(1+\zeta)(-1+\xi-\eta),$$

$$\widehat{H}_{11} = 0.125 \times (1+\xi)(1+\eta)(1+\zeta)(-1+\xi+\eta),$$

$$\widehat{H}_{12} = 0.125 \times (1-\xi)(1+\eta)(1+\zeta)(-1-\xi+\eta),$$

$$\widehat{H}_{13} = 0.5 \times (1-\xi^2)(1-\eta)(1+\zeta),$$

$$\widehat{H}_{14} = 0.5 \times (1-\xi^2)(1-\eta)(1+\zeta),$$

$$\widehat{H}_{15} = 0.5 \times (1-\xi^2)(1+\eta)(1+\zeta),$$

$$\widehat{H}_{16} = 0.5 \times (1-\xi)(1-\eta^2)(1+\zeta),$$

$$\boldsymbol{\varphi}^{\mathrm{T}} = \lfloor \varphi_1 \quad \varphi_2 \quad \cdots \quad \varphi_{20} \rfloor, \tag{73}$$

$$\widehat{\mathbf{U}}^{\mathrm{T}} = \left\lfloor \widehat{U}_1 \quad \widehat{V}_1 \quad \widehat{W}_1 \quad \widehat{U}_2 \quad \widehat{V}_2 \quad \widehat{W}_2 \quad \cdots \quad \widehat{U}_{16} \quad \widehat{V}_{16} \quad \widehat{W}_{16} \right\rfloor, \tag{74}$$

$$\widehat{\mathbf{X}}^{\mathrm{T}} = \left\lfloor \hat{X}_1 \quad \hat{Y}_1 \quad \hat{Z}_1 \quad \hat{X}_2 \quad \hat{Y}_2 \quad \hat{Z}_2 \quad \cdots \quad \hat{X}_{16} \quad \hat{Y}_{16} \quad \hat{Z}_{16} \right\rfloor. \tag{75}$$

The velocity potential is discretized as follows:

$$\mathbf{v} = \nabla\phi = \mathbf{D}\boldsymbol{\varphi}, \tag{76}$$

$$\mathbf{D} = \begin{bmatrix} \dfrac{\partial h_1}{\partial(\hat{x}+\hat{u})} & \dfrac{\partial h_2}{\partial(\hat{x}+\hat{u})} & \cdots & \dfrac{\partial h_{20}}{\partial(\hat{x}+\hat{u})} \\ \dfrac{\partial h_1}{\partial(\hat{y}+\hat{v})} & \dfrac{\partial h_2}{\partial(\hat{y}+\hat{v})} & \cdots & \dfrac{\partial h_{20}}{\partial(\hat{y}+\hat{v})} \\ \dfrac{\partial h_1}{\partial(\hat{z}+\hat{w})} & \dfrac{\partial h_2}{\partial(\hat{z}+\hat{w})} & \cdots & \dfrac{\partial h_{20}}{\partial(\hat{z}+\hat{w})} \end{bmatrix}, \tag{77}$$

$$\frac{\partial}{\partial(\hat{x}+\hat{u})} = \frac{\partial}{\partial\xi}\frac{\partial\xi}{\partial(\hat{x}+\hat{u})} + \frac{\partial}{\partial\eta}\frac{\partial\eta}{\partial(\hat{x}+\hat{u})} + \frac{\partial}{\partial\zeta}\frac{\partial\zeta}{\partial(\hat{x}+\hat{u})}, \tag{78}$$

$$\frac{\partial}{\partial(\hat{y}+\hat{v})} = \frac{\partial}{\partial\xi}\frac{\partial\xi}{\partial(\hat{y}+\hat{v})} + \frac{\partial}{\partial\eta}\frac{\partial\eta}{\partial(\hat{y}+\hat{v})} + \frac{\partial}{\partial\zeta}\frac{\partial\zeta}{\partial(\hat{y}+\hat{v})}, \tag{79}$$

$$\frac{\partial}{\partial(\hat{z}+\hat{w})} = \frac{\partial}{\partial\xi}\frac{\partial\xi}{\partial(\hat{z}+\hat{w})} + \frac{\partial}{\partial\eta}\frac{\partial\eta}{\partial(\hat{z}+\hat{w})} + \frac{\partial}{\partial\zeta}\frac{\partial\zeta}{\partial(\hat{z}+\hat{w})}. \tag{80}$$

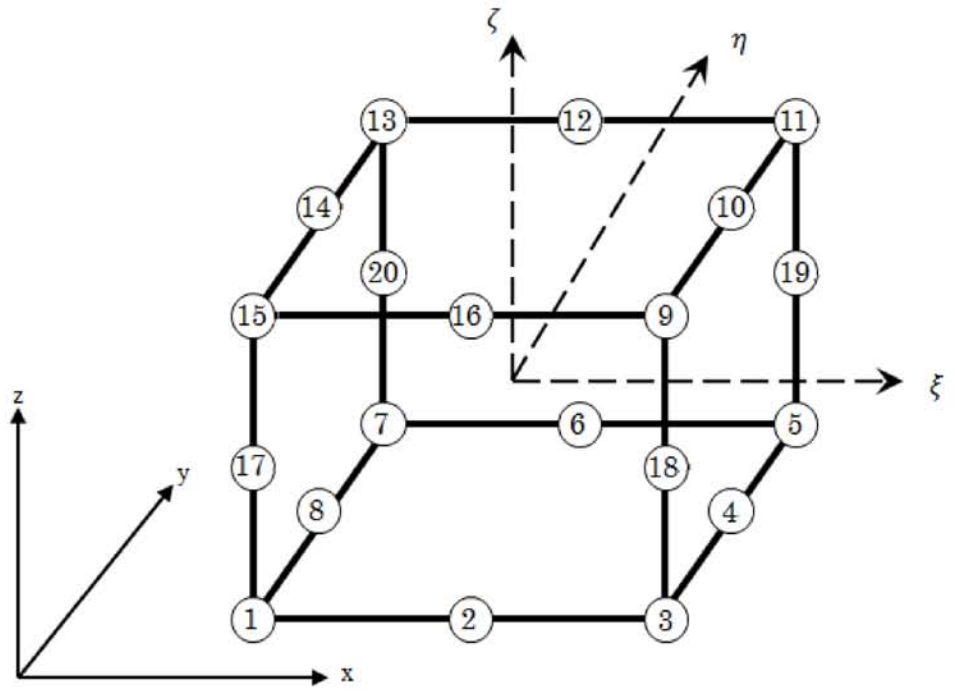

Figure 2.8. 20 nodal isoperimetric element (the number indicate nodal number).

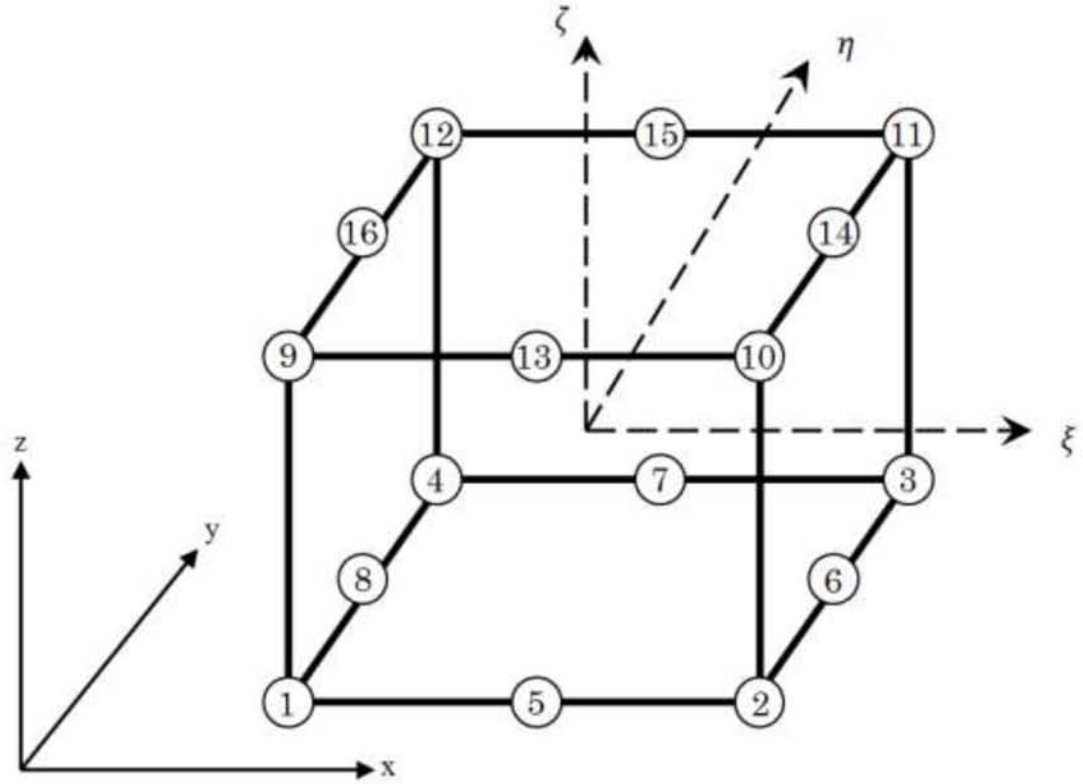

Figure 2.9. 16 nodal isoperimetric element (the number indicate nodal number).

2.8.3 Discretization of the dominant equation

Because $\delta\mathbf{u}$ and $\delta\phi$ are arbitrary in the weak form of the dominant equation (58), the following equations are obtained:

$$\int_{\Omega_s} \left\{\delta\bar{\mathbf{E}}^{\mathrm{T}}\bar{\mathbf{S}} - \rho_m\delta\mathbf{u}^{\mathrm{T}}\mathbf{a} + \rho_m\delta\mathbf{u}^{\mathrm{T}}\left(\tilde{\ddot{\mathbf{u}}} + \frac{1}{\beta_N(\Delta t)^2}\mathbf{u}\right)\right\}\mathrm{d}\Omega_s + \int_{\Gamma_{fs}} \delta\mathbf{u}^{\mathrm{T}}{\pi_f}^{*\prime}\mathbf{n}_f\,\mathrm{d}\Gamma_{fs} = 0, \tag{81}$$

$$\int_{\Omega_f} \rho_f\nabla\delta\phi\cdot\nabla\phi\,\mathrm{d}\Omega_f - \int_{\Gamma_{fs}} \rho_f\left(\tilde{\dot{\hat{\mathbf{u}}}} + \frac{\gamma_N}{\beta_N\Delta t}\hat{\mathbf{u}}\right)\cdot\mathbf{n}_f\delta\phi\,\mathrm{d}\Gamma_{fs} = 0. \tag{82}$$

The FEM is applied to Eqs. (81) and (82) and the mesh control rule Eq. (52) or Eq. (53). They are then discretized, and the following equations are derived:

$$\int_{\Omega_s} \left\{\delta\bar{\mathbf{E}}^{\mathrm{T}}\bar{\mathbf{S}} - \rho_m\delta\mathbf{u}^{\mathrm{T}}\mathbf{a} + \rho_m\delta\mathbf{u}^{\mathrm{T}}\left(\tilde{\ddot{\mathbf{u}}} + \frac{1}{\beta_N(\Delta t)^2}\mathbf{u}\right)\right\}\mathrm{d}\Omega_s + \int_{\Gamma_{fs}} \delta\mathbf{u}^{\mathrm{T}}{\pi_f}^{"}\mathbf{n}_f\,\mathrm{d}\Gamma_{fs}$$

$$= \delta\mathbf{U}^{\mathrm{T}}\int_{-1}^{1}\int_{-1}^{1}\left\{\begin{array}{c}\bar{\mathbf{B}}^{\mathrm{T}}\bar{\mathbf{S}} - \rho_m\mathbf{H}^{\mathrm{T}}\mathbf{a} \\ +\rho_m\mathbf{H}^{\mathrm{T}}\mathbf{H}\left(\tilde{\ddot{\mathbf{U}}} + \frac{1}{\beta_N(\Delta t)^2}\mathbf{U}\right)\end{array}\right\} t_m\det[J_s]\,\mathrm{d}\xi\mathrm{d}\eta$$

$$+\delta\mathbf{U}^{\mathrm{T}}\int_{-1}^{1}\int_{-1}^{1}\rho_f\mathbf{H}^{\mathrm{T}}\left\{\begin{array}{c}\boldsymbol{\varphi}^{\mathrm{T}}\mathbf{D}^{\mathrm{T}}\mathbf{D}\boldsymbol{\varphi} + \mathbf{a}\hat{\mathbf{H}}\left(\hat{\mathbf{X}} + \hat{\mathbf{U}}\right) \\ +\mathbf{h}\left(\widetilde{\boldsymbol{\varphi}^{*}} + \frac{\gamma_N}{\beta_N\Delta t}\boldsymbol{\varphi}\right) - \hat{\mathbf{H}}\left(\tilde{\hat{\mathbf{U}}} + \frac{\gamma_N}{\beta_N\Delta t}\hat{\mathbf{U}}\right)\mathbf{D}\boldsymbol{\varphi}\end{array}\right\}\mathbf{n}_f\det[J_\Gamma]\,\mathrm{d}\xi\mathrm{d}$$

$$= \delta\mathbf{U}^{\mathrm{T}}\mathbf{G}_0 + \delta\mathbf{U}^{\mathrm{T}}\mathbf{G}_3 = 0, \tag{83}$$

$$\int_{\Omega_f} \rho_f\nabla\delta\phi\cdot\nabla\phi\,\mathrm{d}\Omega_f - \int_{\Gamma_{fs}} \rho_f\left(\tilde{\dot{\hat{\mathbf{u}}}} + \frac{\gamma_N}{\beta_N\Delta t}\hat{\mathbf{u}}\right)\mathbf{n}_f\delta\phi\,\mathrm{d}\Gamma_{fs}$$

$$= \delta\boldsymbol{\varphi}^{\mathrm{T}}\int_{-1}^{1}\int_{-1}^{1}\int_{-1}^{1}\rho_f\mathbf{D}^{\mathrm{T}}\mathbf{D}\boldsymbol{\varphi}\det[J_f]\,\mathrm{d}\xi\mathrm{d}\eta\mathrm{d}\zeta$$

$$+\boldsymbol{\delta\varphi}^{\mathrm{T}}\int_{-1}^{1}\int_{-1}^{1}\rho_f\mathbf{h}^{\mathrm{T}}\left(-\hat{\mathbf{H}}\tilde{\hat{\mathbf{U}}} - \frac{\gamma_N}{\beta_N\Delta t}\hat{\mathbf{H}}\hat{\mathbf{U}}\right)\mathbf{n}_f\det[J_\Gamma]\,\mathrm{d}\xi\mathrm{d}\eta$$

$$= \delta\boldsymbol{\varphi}^{\mathrm{T}}\mathbf{G}_1 + \delta\boldsymbol{\varphi}^{\mathrm{T}}\mathbf{G}_4 = 0, \tag{84}$$

$$\int_{\Omega_f} \rho_f\left(\hat{\mathbf{u}} - \frac{\hat{z}}{h}\mathbf{u}\right)\cdot\delta\hat{\mathbf{u}}\mathrm{d}\Omega_f$$

$$= \delta\widehat{\mathbf{U}}^{\mathrm{T}} \int_{-1}^{1}\int_{-1}^{1}\int_{-1}^{1} \rho_f \widehat{\mathbf{H}}^{\mathrm{T}} \left(\widehat{\mathbf{H}}\widehat{\mathbf{U}} - \frac{\hat{z}}{h}\mathbf{H}\mathbf{U}\right) \det[J_f]\,\mathrm{d}\xi\mathrm{d}\eta\mathrm{d}\zeta$$

$$= \delta\boldsymbol{\varphi}^{\mathrm{T}}\mathbf{G}_2 = 0, \tag{85}$$

$$\int_{\Omega_f} \rho_f \left\{\widehat{\mathbf{u}} - \left(\mathbf{u}_l + \frac{\hat{z}}{h}(\mathbf{u}_u - \mathbf{u}_l)\right)\right\} \cdot \delta\widehat{\mathbf{u}}\mathrm{d}\Omega_f$$

$$= \delta\widehat{\mathbf{U}}^{\mathrm{T}} \int_{-1}^{1}\int_{-1}^{1}\int_{-1}^{1} \rho_f \widehat{\mathbf{H}}^{\mathrm{T}} \left\{\widehat{\mathbf{H}}\widehat{\mathbf{U}} - \mathbf{H}\left(\mathbf{U}_u - \frac{\hat{z}}{h}\mathbf{U}_l\right)\right\} \det[J_f]\,\mathrm{d}\xi\mathrm{d}\eta\mathrm{d}\zeta$$

$$= \delta\boldsymbol{\varphi}^{\mathrm{T}}\mathbf{G}_2' = 0, \tag{86}$$

$$\det[\mathbf{J}_s] = \det\begin{bmatrix} \dfrac{\partial x}{\partial \xi} & \dfrac{\partial y}{\partial \xi} \\ \dfrac{\partial x}{\partial \eta} & \dfrac{\partial y}{\partial \eta} \end{bmatrix}, \tag{87}$$

$$\det[\mathbf{J}_f] = \det\begin{bmatrix} \dfrac{\partial(\hat{x}+\hat{u})}{\partial \xi} & \dfrac{\partial(\hat{y}+\hat{v})}{\partial \xi} & \dfrac{\partial(\hat{z}+\hat{w})}{\partial \xi} \\ \dfrac{\partial(\hat{x}+\hat{u})}{\partial \eta} & \dfrac{\partial(\hat{y}+\hat{v})}{\partial \eta} & \dfrac{\partial(\hat{z}+\hat{w})}{\partial \eta} \\ \dfrac{\partial(\hat{x}+\hat{u})}{\partial \zeta} & \dfrac{\partial(\hat{y}+\hat{v})}{\partial \zeta} & \dfrac{\partial(\hat{z}+\hat{w})}{\partial \zeta} \end{bmatrix}, \tag{88}$$

$$\det[\mathbf{J}_\Gamma] = \det\begin{bmatrix} \dfrac{\partial(\hat{x}+\hat{u})}{\partial \xi} & \dfrac{\partial(\hat{y}+\hat{v})}{\partial \xi} \\ \dfrac{\partial(\hat{x}+\hat{u})}{\partial \eta} & \dfrac{\partial(\hat{y}+\hat{v})}{\partial \eta} \end{bmatrix}, \tag{89}$$

$$n_f = \frac{\left\{\dfrac{\partial(\hat{\mathbf{x}}+\hat{\mathbf{u}})}{\partial y}\right\} \times \left\{\dfrac{\partial(\hat{\mathbf{x}}+\hat{\mathbf{u}})}{\partial x}\right\}}{\left|\left\{\dfrac{\partial(\hat{\mathbf{x}}+\hat{\mathbf{u}})}{\partial y}\right\} \times \left\{\dfrac{\partial(\hat{\mathbf{x}}+\hat{\mathbf{u}})}{\partial x}\right\}\right|}. \tag{90}$$

The relation $\delta\bar{\mathbf{E}} = \bar{\mathbf{B}}\delta\mathbf{U}$ is explained in Appendix A. Here t_m denotes the membrane thickness. Gaussian integration is used to calculate the integrals and the integral point number is taken as $3 \times 3 = 9$ points in the structural domain and $3 \times 3 \times 3 = 27$ points in the liquid domain. The following equation is derived from the above expressions

$$\begin{Bmatrix} \mathbf{G}_0 + \mathbf{G}_3 \\ \mathbf{G}_2(\text{or } \mathbf{G}_2') \\ \mathbf{G}_1 + \mathbf{G}_4 \end{Bmatrix} = {}^{t+\Delta t}\mathbf{G} = 0, \tag{91}$$

where ${}^{t+\Delta t}\mathbf{G}$ denotes the residual vector at time $t + \Delta t$.

2.9 Solution method for nonlinear equation

Equation (91) cannot be solved directly because it is a nonlinear simultaneous equation. Therefore, the Newton–Raphson method, which is an iterative solution method, is used in this analysis.

2.9.1 Newton–Raphson method

With ${}^{t+\Delta t}\mathbf{d} = \left[{}^{t+\Delta t}\mathbf{U}^{\mathrm{T}} \quad {}^{t+\Delta t}\widehat{\mathbf{U}}^{\mathrm{T}} \quad {}^{t+\Delta t}\boldsymbol{\varphi}^{\mathrm{T}}\right]^{\mathrm{T}}$ denoting the variable vector at time $t + \Delta t$, Eq. (91) can be written as follows:

$$ {}^{t+\Delta t}\mathbf{G} = \mathbf{G}\left({}^{t+\Delta t}\mathbf{d}\right) = \mathbf{P}\left({}^{t+\Delta t}\mathbf{d}\right) - {}^{t+\Delta t}\mathbf{f} = 0. \tag{92}$$

Here $\mathbf{P}$ denotes the variable vector composed of ${}^{t+\Delta t}\mathbf{d}$ and ${}^{t+\Delta t}\mathbf{f}$ denotes the term that is independent of the variable (the external vector). The Newton–Raphson method gives a first-order approximation (Taylor expansion) of Eq. (92) and, with i denoting the iteration number, this can be written as follows:

$$ {}^{t+\Delta t}\mathbf{G}_{i+1} = \mathbf{G}\left({}^{t+\Delta t}\mathbf{d}_{i+1}\right) \approx \mathbf{G}\left({}^{t+\Delta t}\mathbf{d}_{i}\right) + \mathbf{K}_i \delta^{t+\Delta t}\mathbf{d}_i, \tag{93}$$

$$ \mathbf{K}_i = {}^{t+\Delta t}\left(\frac{\partial \mathbf{G}}{\partial \mathbf{d}}\right)_i = {}^{t+\Delta t}\left(\frac{\partial \mathbf{P}}{\partial \mathbf{d}}\right)_i, \tag{94}$$

where $\mathbf{K}_i$ and $\delta^{t+\Delta t}\mathbf{d}_i$ are the tangential stiffness matrix and the variable increment at iteration i. The following equation is derived from Eq. (93) at iteration i:

$$ \mathbf{K}_i \delta^{t+\Delta t}\mathbf{d}_i = -\mathbf{G}\left({}^{t+\Delta t}\mathbf{d}_i\right). \tag{95}$$

The approximate solution in the iterative process can be expressed as follows:

$$ {}^{t+\Delta t}\mathbf{d} = {}^{t}\mathbf{d} + \Delta\, {}^{t}\mathbf{d} \approx {}^{t+\Delta t}\mathbf{d}_i + \delta^{t+\Delta t}\mathbf{d}_i = {}^{t+\Delta t}\mathbf{d}_{i+1}, \tag{96}$$

where ${}^{t+\Delta t}\mathbf{d}$ is the solution at time $t + \Delta t$ and $\Delta\, {}^{t}\mathbf{d}$ is the increment from solution ${}^{t}\mathbf{d}$ at time t.

2.9.2 Tangential stiffness matrix

In the following, $g_i^0, \ldots, g_i^4$ denote the elements of the residual vectors $\mathbf{G}_0, \ldots, \mathbf{G}_4$ and i is the number of degrees of freedom (DOF). The elements of the tangential stiffness matrix are as follows:

$$k_{ij}^{0} = \frac{\partial g_i^0}{\partial u_j}, \tag{97}$$

$$k_{ij}^{1} = \frac{\partial g_i^1}{\partial \hat{u}_j}, \tag{98}$$

$$k_{ij}^{2} = \frac{\partial g_i^1}{\partial \phi_j}, \tag{99}$$

$$k_{ij}^{3} = \frac{\partial g_i^2}{\partial \hat{u}_j}, \tag{100}$$

$$k_{ij}^{4} = \frac{\partial g_i^3}{\partial \phi_j}, \tag{101}$$

$$k_{ij}^{5} = \frac{\partial g_i^3}{\partial \hat{u}_j}, \tag{102}$$

$$k_{ij}^{6} = \frac{\partial g_i^4}{\partial \hat{u}_j}. \tag{103}$$

The following central difference is calculated in this analysis:

$$k_{ij} = \frac{g_i(\mathbf{d} + \Delta d_j) - g_i(\mathbf{d} - \Delta d_j)}{2\Delta d_j}, \tag{104}$$

where a value of $\Delta d_j = 1.0 \times 10^{-8}$ is assumed. $k_{ij}^0, \dots, k_{ij}^6$ can be taken as the elements of $\mathbf{K}_0, \dots, \mathbf{K}_6$, respectively. The following equation can be derived from Eq. (95):

$$\begin{bmatrix} \mathbf{K}_0 & \mathbf{K}_5 & \mathbf{K}_4 \\ 0 & \mathbf{K}_3 & 0 \\ 0 & \mathbf{K}_1 + \mathbf{K}_6 & \mathbf{K}_2 \end{bmatrix} \begin{Bmatrix} \delta\mathbf{U} \\ \delta\hat{\mathbf{U}} \\ \delta\boldsymbol{\varphi} \end{Bmatrix} = -\begin{Bmatrix} \mathbf{G}_0 + \mathbf{G}_3 \\ \mathbf{G}_2 \\ \mathbf{G}_1 + \mathbf{G}_4 \end{Bmatrix}. \tag{105}$$

The tangential stiffness vector is renewed every iteration, and the variable vector ${}^{t+\Delta t}\mathbf{d}$ at the time $t + \Delta t$ is calculated from the variable vector ${}^{t}\mathbf{d}$ at time t by repeating the calculation.

2.9.3 Convergence test

This iterative calculation converges when all the components of the residual vector ${}^{t+\Delta t}\mathbf{G}$ become zero. However, they cannot become exactly zero in a numerical calculation, so, in this analysis, convergence is assumed to occur when the norms of the variable increment $\delta^{t+\Delta t}\mathbf{d}_i$ and the residual vector ${}^{t+\Delta t}\mathbf{G}$ and the inner product of $\delta^{t+\Delta t}\mathbf{d}_i$ and ${}^{t+\Delta t}\mathbf{G}_i$ become less than some given values:

$$\left\{\delta^{t+\Delta t}\mathbf{d}_i\right\}^{\mathrm{T}}\left\{\delta^{t+\Delta t}\mathbf{d}_i\right\} < (u\text{-tol}) \times \left\{\delta^{t+\Delta t}\mathbf{d}_1\right\}^{\mathrm{T}}\left\{\delta^{t+\Delta t}\mathbf{d}_1\right\}, \tag{106}$$

$$\left\{{}^{t+\Delta t}\mathbf{G}_i\right\}^{\mathrm{T}}\left\{{}^{t+\Delta t}\mathbf{G}_i\right\} < (r\text{-tol}) \times \left\{{}^{t+\Delta t}\mathbf{G}_1\right\}^{\mathrm{T}}\left\{{}^{t+\Delta t}\mathbf{G}_1\right\}, \tag{107}$$

$$\left\{\delta^{t+\Delta t}\mathbf{d}_i\right\}^{\mathrm{T}}\left\{{}^{t+\Delta t}\mathbf{G}_i\right\} < (e\text{-tol}) \times \left\{\delta^{t+\Delta t}\mathbf{d}_1\right\}^{\mathrm{T}}\left\{{}^{t+\Delta t}\mathbf{G}_1\right\}. \tag{108}$$

Here values of $(u\text{-tol})$, $(r\text{-tol})$ and $(e\text{-tol})$ in the range $1.0 \times 10^{-8} - 1.0 \times 10^{-10}$ are assumed.

CHAPTER 3

A TWO-DIMENSIONAL

3.1 Objectives

The two-dimensional of a rubberlike membrane and liquid problem in a rectangular tank subject to horizontal vibration is investigated using the arbitrary Lagrangian–Eulerian finite element method (ALE-FEM). In addition, the effects of finite deformations of the membrane, i.e., material and geometrical nonlinearities in the membrane and the liquid, are taken into consideration. Furthermore, the influences of a large excitation, and membrane tension were examined. The 2D numerical evaluations were performed and the time historical response, frequency response, liquid pressure, and membrane and liquid displacements were presented. Finally, the membrane and liquid nonlinear behavior, especially under low initial strain and large excitation, are discussed.

3.2 Numerical evaluation and discussion

In this section, the researchers focused on the membrane behavior in the vicinity of the natural frequency, and they presented some numerical results that are related to the discussion. The parameters of the numerical model were set up as follows. The width and depth of the container size were set to 0.8 m and 0.3 m, respectively, and the membrane thickness was 0.001 m. The liquid was assumed to be water with a density of 1,000 kg/m^3. The excitation was restricted to a sinusoidal horizontal excitation, and then, it continued with an undamped free vibration. The amplitudes of excitation were fixed at constant values of 0.001 m/s^2 and 0.01 m/s^2 for small and large deformations, respectively. This membrane was subjected to uniform tension of 4.91, 9.60, and 16.92 kN/m in the direction horizontal and perpendicular to the sheet. This initial stress stated corresponds to the

bi-axial uniform strain of 2.0, 5.0, and 10%, respectively, under the plane strain condition and were applied to various frequencies. Two-node rod elements and eight-node rectangular elements were employed for the membrane deformation and liquid potential, respectively. The finite element mesh for the liquid potential consisted of 100 (10*10) elements; coarser elements were employed near the bottom compared to the interface. The membrane was divided into 10 elements of constant length, as shown in Fig. 3.1. The time increment in the time integration scheme was 0.02 of one period of the driving acceleration. The influence of the rubberlike membrane is considered in the sloshing analysis. The tank size is the same in the sloshing model and the rubberlike membrane–liquid interaction model. For the interaction model, the resonant frequency at the maximum vertical displacement of five cycles is used as the vibration frequency. For the sloshing model, the one-degree mode natural frequency of the linear theory is used as the vibration frequency. The linear theory of sloshing is described in Appendix B.

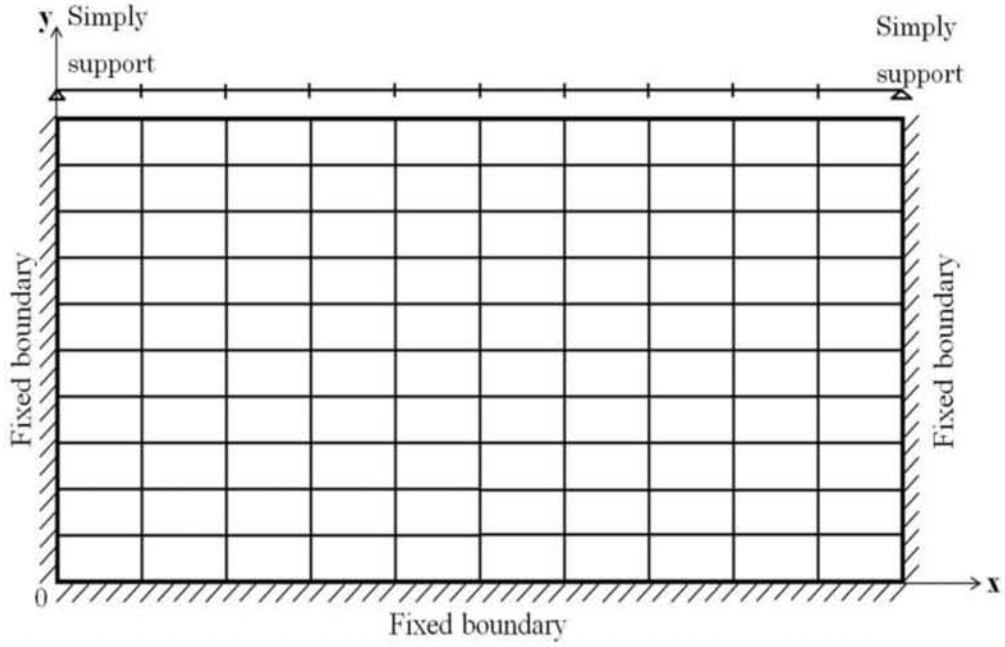

Figure 3.1. Finite element model of analytical model.

3.2.1 Time history response of the membrane

We investigated the time history response of a membrane 0.1 m from the left of tank. This position had the largest deformation of any position when the first vibration mode dominated.

The time history at this point is plotted in Fig. 3.2 and 3.3. The vertical left axis is the vertical displacement of the membrane and the vertical right axis is the excitation amplitude. The driving frequency is 0.95 Hz, which is the natural frequency of an initial strain of 2% and excitation amplitude of 0.001 m/s^2 and 0.01 m/s^2, as shown in the next section. Fig. 3.2 and 3.3 show the amplitude of displacement continues with a constant amplitude for approximately 55 sec. In Fig. 3.2, it is noticed that the amplitude of the upward displacement is symmetrical with the amplitude of the downward displacement. In contrast, in Fig. 3.3, the amplitude of upward displacement is approximately 1.25 times larger than the amplitude of the downward displacement. This phenomenon has been generally observed in studies of liquid sloshing and it is strongly affected by the nonlinearity of a liquid because of the large deformation.

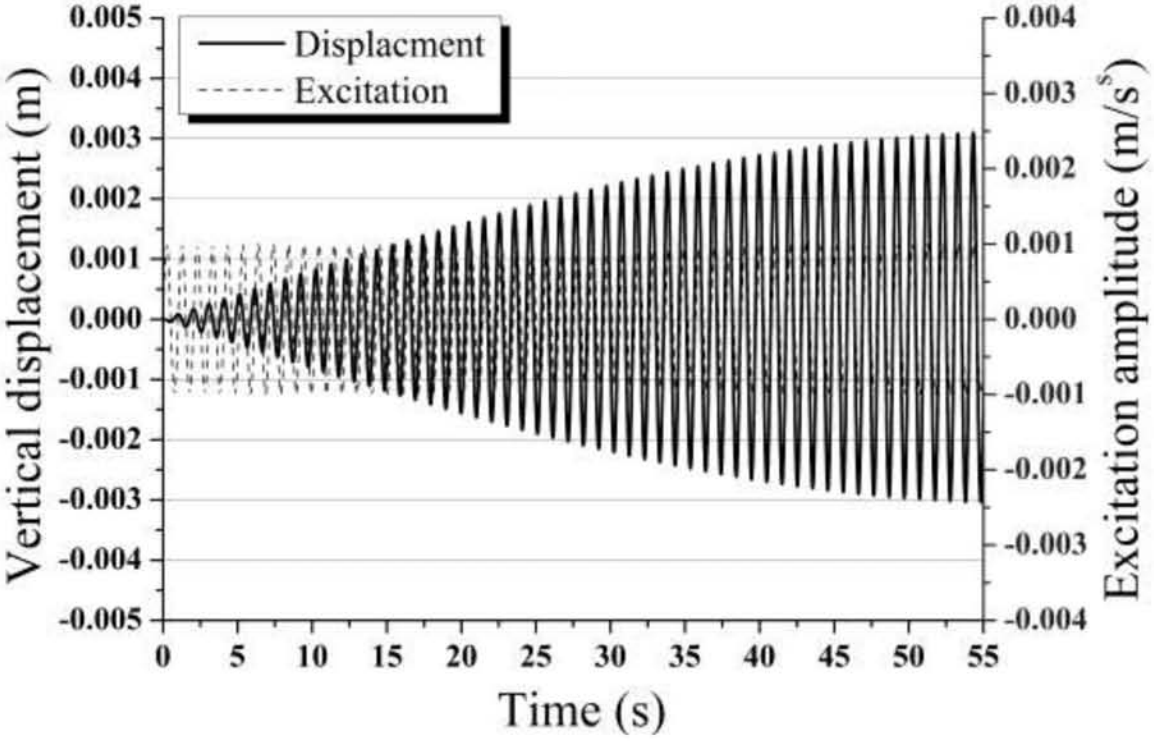

Figure 3.2. Time historical response of 0.001 m/s^2.

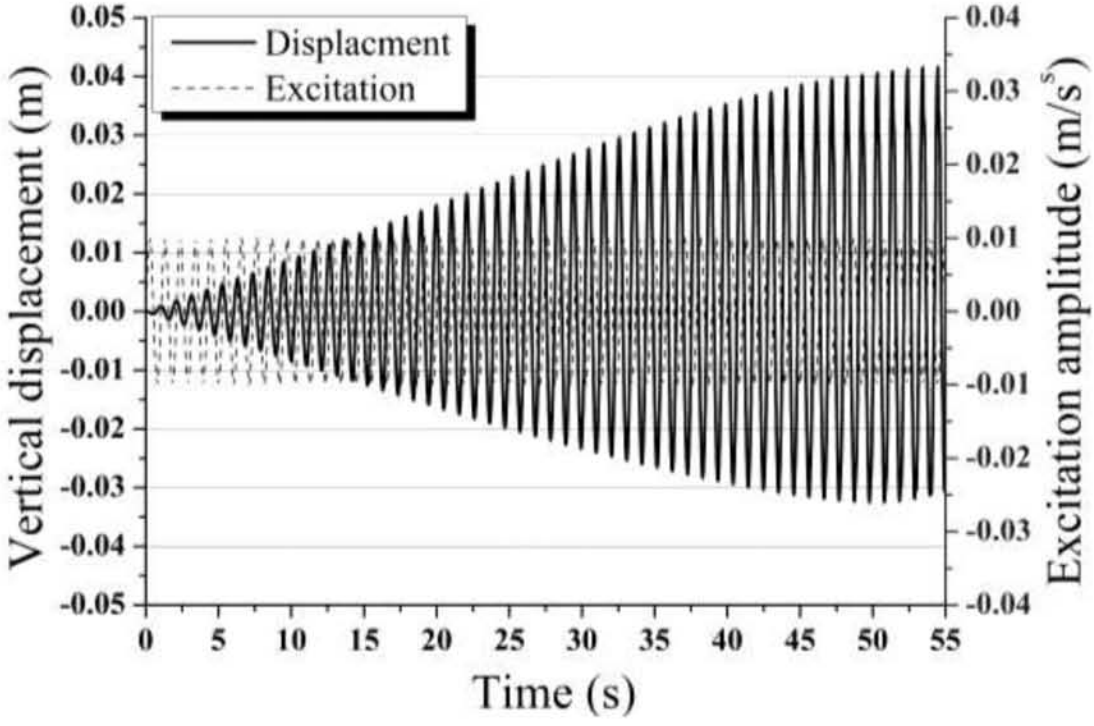

Figure 3.3. Time historical response of 0.01 m/s^2.

3.2.2 Frequency response

In this part of the investigation, the excitation acceleration varied from 0.001 to 0.01 m/s^2 to examine the natural frequency. The maximum displacement after five cycles, which was normalized by the tank depth, is shown in Fig. 3.4. For the sloshing model, the first mode of the natural frequency is 0.9 Hz according to linear theory, and this decreases by only 0.3% when the deformation becomes large. This is a nonlinearity of the normal softening type. In the interaction model, the natural frequency is 1.0 Hz at an excitation of 0.01 m/s^2, which is 10% higher than in the sloshing model. Moreover, the natural frequency at an excitation of 0.01 m/s^2 increases by 1.6% compared to 0.001 m/s^2 that agree with the literatures [5, 6].

On the other hand, Fig. 3.5 shows the initial strain variation with respect to the driving frequency. After five cycles, the oscillation still has approximately constant amplitude. It shows the comparison of the upward displacement of the membrane for initial strains of 2, 5, and 10% at an excitation of 0.01 m/s^2. As a result of the displacement, the peaks of each initial strain are different. At a low initial strain of 2%, the resonance frequency is approximately 0.95 Hz; the resonance frequencies increase to 0.98 Hz and 1.00 Hz when the initial strains are increased to 5 and 10%, respectively. The frequency increases by approximately 3% when initial strain increases one time. These results agree with the literature from Bauer [13, 23] based on Fourier-Bessel series theory that the natural frequency must increase when a free liquid surface was completely covered by a rubberlike membrane, and the magnitude depends on the stiffness of the rubberlike coverage. It can be confirmed that the move to a high-frequency range of the resonance frequency is large in comparison to the initial strains and that the hardening type nonlinearity is stronger due to the rubberlike membrane [13]. In this analysis, the influence of the geometric nonlinearity is small because the behavior is dominated by the initial

strain. In the large-deformation domain, the natural frequency increases, but it shows a complex response because of the left–right asymmetry. Therefore, it is possible to analyze the vertical displacement only up to values that are 10% of the tank depth. It is difficult to observe the behavior in the strong-nonlinearity domain.

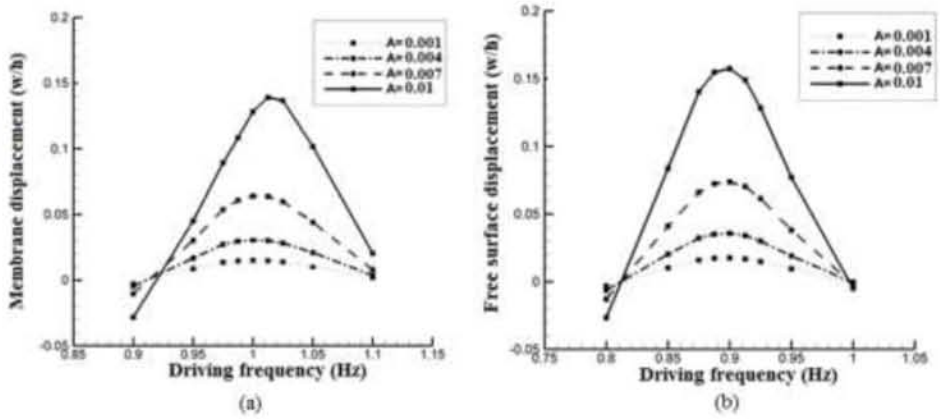

Figure 3.4. Resonant frequency curve (a) Interaction model and (b) Sloshing model.

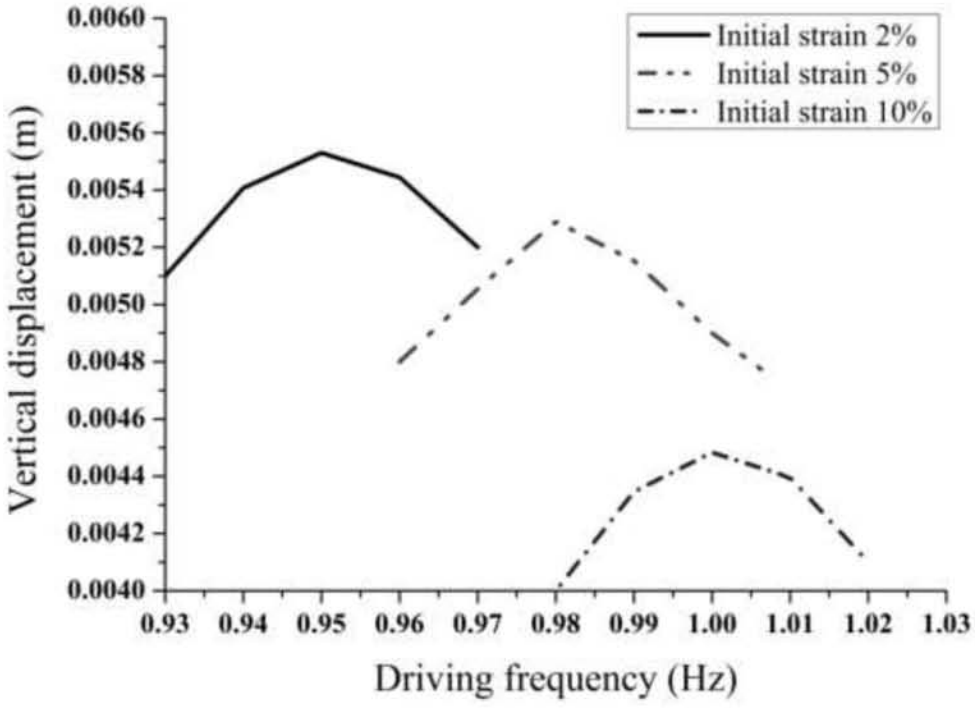

Figure 3.5. Upward displacement vs. frequency with excitation 0.01 m/s^2.

3.2.3 Maximum response amplitude

Figure 3.6 shows the maximum vertical displacement of the membrane at $1/8^{th}$ of tank width for the initial strains of 2, 5, and 10%. From Fig. 3.5, it can be seen that the displacement of the membrane is divided into two areas: the linear increasing area and the sharply increasing area. In the first area, the maximum displacement increases proportionally to the excitation amplitude change. Then, the displacement increases exponentially in the second area (after 0.005 m/s^2) as the excitation amplitude increases. The excitation amplitude changes from 0.001 m/s^2 to 0.01 m/s^2, which is 10 times, but the maximum displacement increase more than 20 times. This observation can be explained by the fact that the deformations are nonlinearly affected by the excitation amplitude in the second behavior area of the membrane.

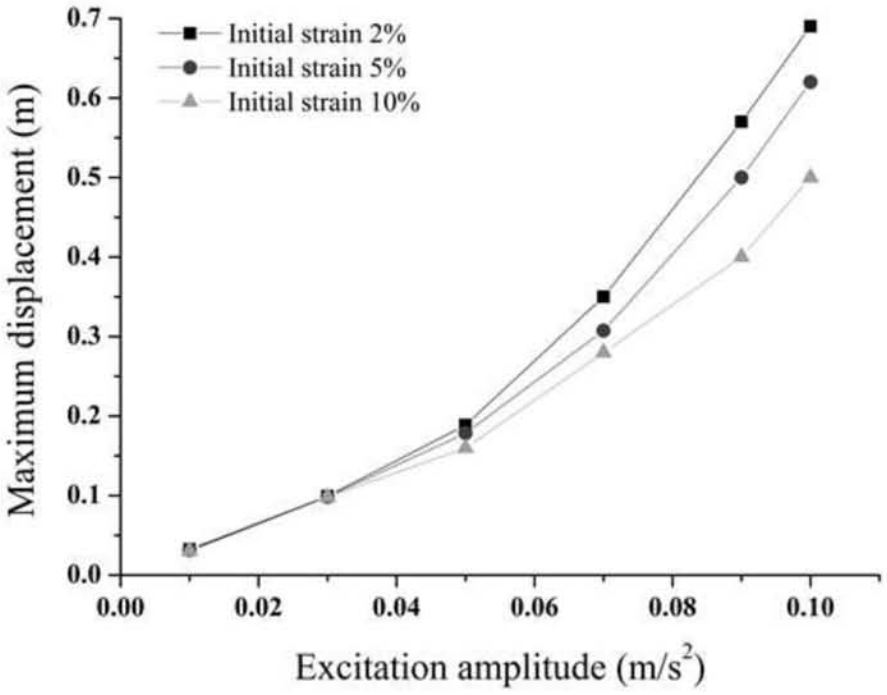

Figure 3.6. Maximum displacement of membrane vs. excitation.

3.2.4 Deformation of the liquid and membrane

Figure 3.7 represents the deformation profiles of the membrane when it has a maximum upward displacement for various initial strains and excitation amplitudes. This figure shows the two properties that cannot be described by linear theory. First, the maximum upward displacement increases more than the maximum downward displacement, as mentioned before, and simultaneously the slope of the upward shape sharply increases. At a low excitation of 0.001 m/s^2, the maximum difference between the upward and downward displacement is 8.34%, which occurs at an initial strain of 2%, and the maximum differences decrease to 2.01% and 1.09% for initial strains of 5 and 10%, respectively. At a high excitation of 0.01 m/s^2, the maximum difference of the upward and downward displacement is 17.08%, which occurs at an initial strain of 2%, and the maximum differences decrease to 14.21% and 11.74% for the initial strains of 5 and 10%, respectively. From the results, it is noticed that the maximum difference occurs at the high excitation of 0.01 m/s^2 and low initial strain of 2%. These types of phenomena are well-known in the field of free surface motion of a liquid, and the main factor is the nonlinearity from the convection term of the liquid. The membrane motion is primarily dominated by the liquid motion because of the low stiffness of the membrane and large deformation. Therefore, this sloshing-like motion of the liquid is very important to the membrane system. The second cause of this motion is the asymmetry of the deformation, as shown in Fig. 3.7. In the other words, if a linear theory was employed, symmetry would have been predicted [53]. Contrary to this, the point that indicates zero vertical displacement shifts to the side of the upward deformation, i.e., to the left side with an enlargement of the deformation in this figure. In same direction as the first property, the maximum shift is 2.44% of 0.8 m and occurs at the high excitation of 0.01 m/s^2 and low initial strain of 2%. When the deformation is large, the deformation of the membrane has

left-right asymmetry. This asymmetry also appears in the sloshing model because of the convection term. At five cycles, Fig. 3.8 shows the displacement of the liquid at different heights in the tank and the membrane surface with an initial strain of 2% and excitation of 0.01 m/s^2. This result ensures agreement between the liquid and membrane motion for a large deformation and low stiffness.

Figure 3.9 shows the vertical displacement of the membrane after five and 15 cycles for the interaction and sloshing models, respectively. The maximum displacement of the upper surface in the sloshing model is at the left end of the tank. In contrast, the maximum displacement of the membrane in the interaction model is at x = 0.1 m because of the presence of a fixed point at the end of the tank.

The solid lines indicate the rubberlike membrane in the interaction model and the dashed lines indicate the sloshing model. The deformation of the membrane near the center of the tank (x = 0.1-0.7 m) in the interaction model is in good agreement with the deformation of the free surface in the sloshing model. The effect of the membrane is strong only near the edge of the tank, where the deformation is constrained because the membrane is attached to the edge of the tank. As the deformation of the membrane becomes large, it develops a left–right asymmetry with a greater displacement on the upward-displacement side (the left side). This phenomenon is mainly observed when studying a liquid sloshing [12] and it is strongly.

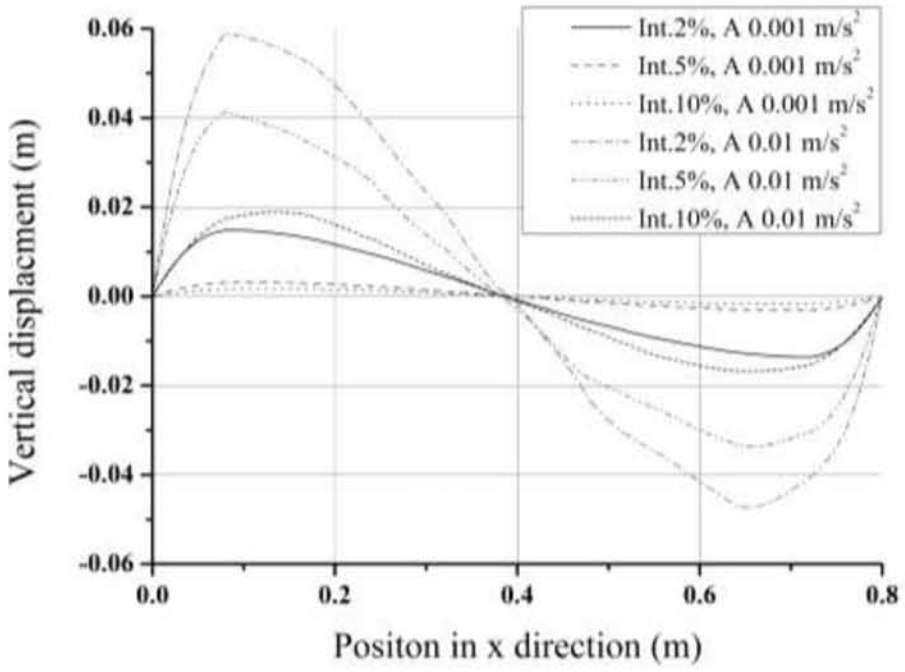

Figure 3.7. Deformation of membrane.

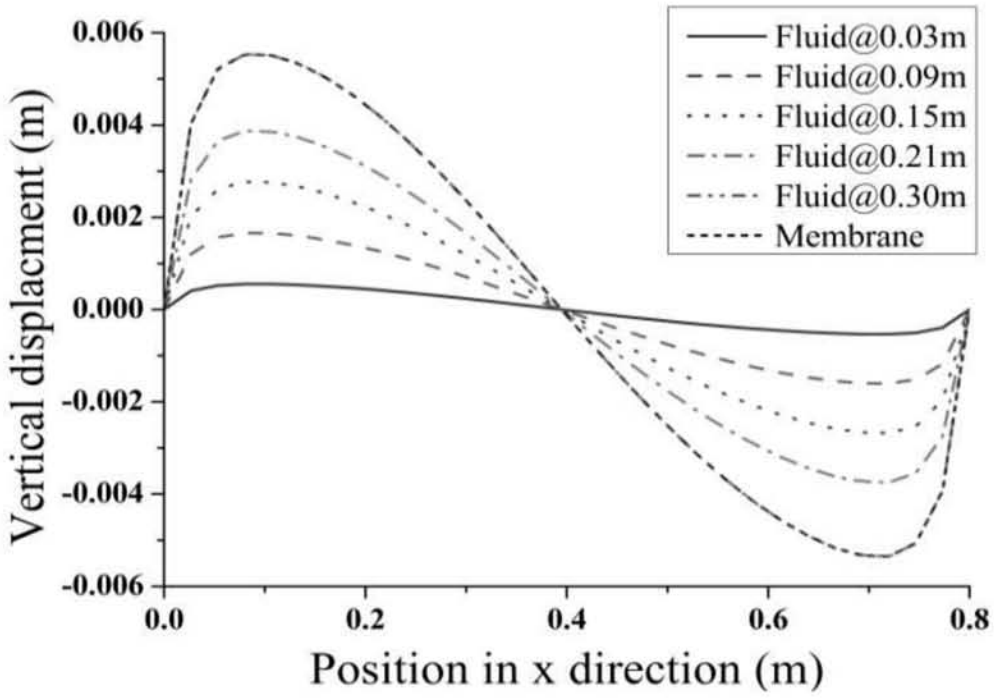

Figure 3.8. Liquid and membrane displacement.

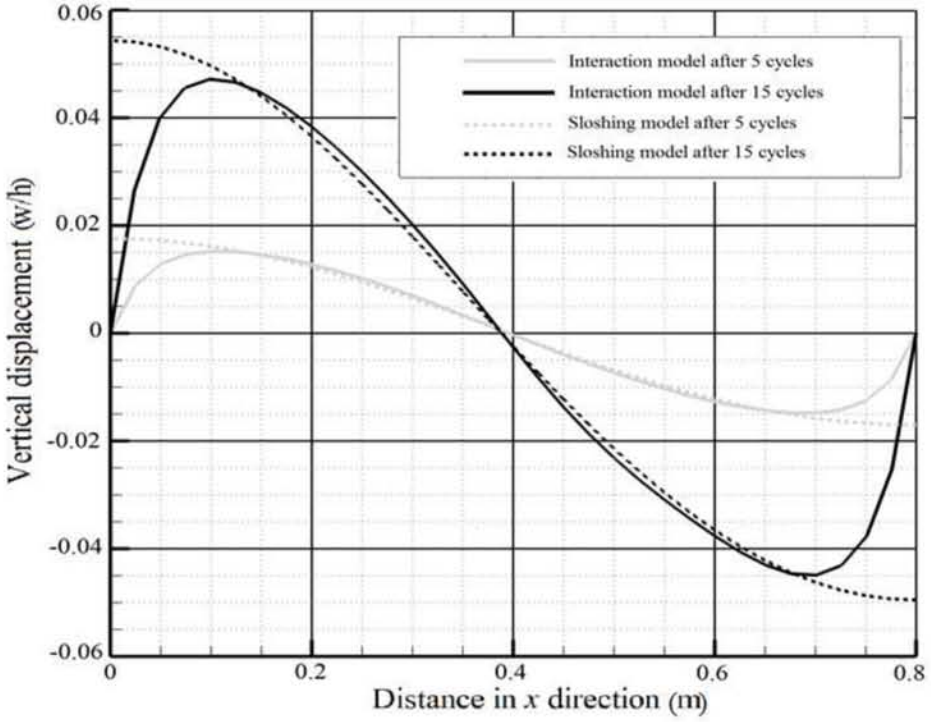

Figure 3.9. Surface displacement.

3.2.5 Equilibrium of forces in the liquid–structure interaction

To demonstrate the validity of the results obtained here for the deformation, the equilibrium forces in the liquid–structure interaction will be examined. We consider a membrane without bending stiffness subject to liquid pressure that produces stress and curvature in the membrane. The equilibrium equation in the out-of-plane direction can take the following form [12]:

$$\frac{\sigma t_m}{r} = -\pi_l + \rho_m t_m \mathbf{a} \cdot \mathbf{n}_s, \tag{109}$$

where σ and r are the Cauchy stresses and radius of curvature, respectively, t_m is the film thickness, π_l is the liquid pressure, $\mathbf{a}$ is the membrane acceleration, and $\mathbf{n}_s$ is the normal vector of the structure. The right-hand side of this equation represents the external force per unit area with the first term representing the liquid pressure force applied to the membrane and the second term representing the inertial force on the membrane. Fig. 3.10

is a graphical representation of the forces in Eq. (109), where Z denotes the sum of the external forces.

The membrane is supported by the component of the sectional force in the out-of-plane direction, which is equivalent to the external force. For this reason, if the curvature is small (i.e., the radius of the curvature is large), the component in the out-of-plane direction will be small, and the external force will also be small. In contrast, if the curvature is large, the component in the out-of-plane direction will be large, and the external force will also be large. The Cauchy stress is dominated by the initial tension. The difference between the maximum and minimum tensile stresses in the x direction is only 11%, and the distribution appears to be uniform. The external force applied to the membrane by the liquid is due only to the liquid pressure because the liquid is assumed to be inviscid. The distributions of the curvature and pressure must match to satisfy Eq. (109).

The distribution of the liquid pressure with the exclusion of the hydrostatic pressure after 15 cycles was shown in Fig. 3.11. The distribution is large near the edge of tank, where the liquid motion is prevented because of the attachment of the membrane. The curvature in the x direction is shown in Fig. 3.12. The curvature in the x direction is large near the edge of the tank but is almost zero elsewhere. This is similar to the distribution of liquid pressure. From Fig. 3.12, it can be seen that there is equilibrium between the membrane and the liquid, and the results obtained for the deformation are considered to be valid. In addition, it should be noted that the FEM analysis was not performed directly, but was formulated using the energy equation. In this case, instead of the natural boundary condition, the mechanical boundary condition was used, which is difficult to strictly satisfy.

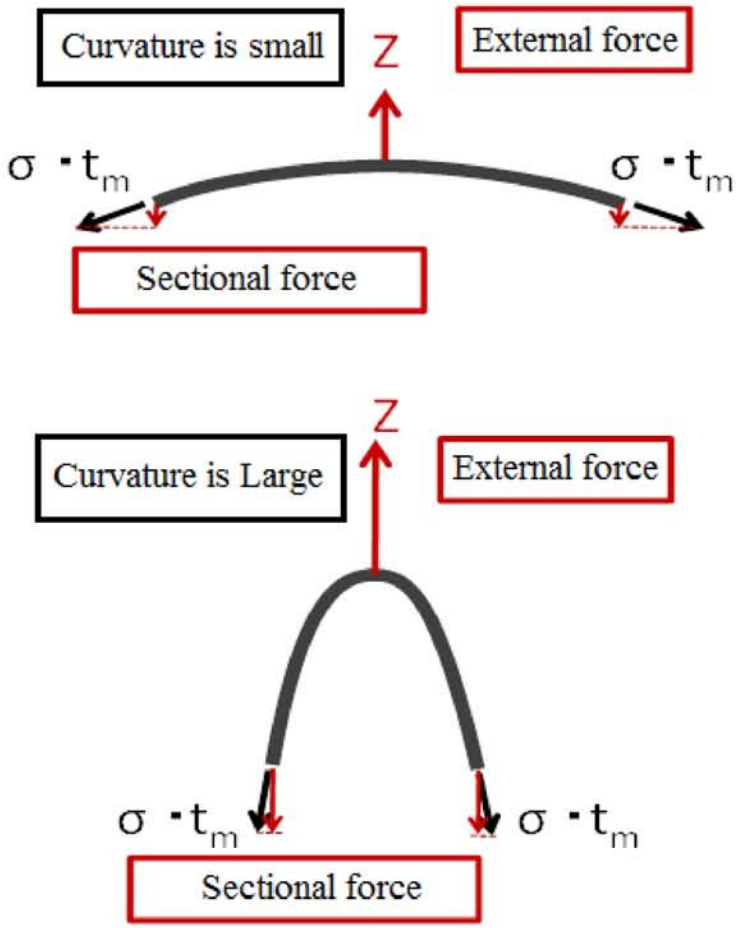

Figure 3.10. Relationship of surface external force and curvature.

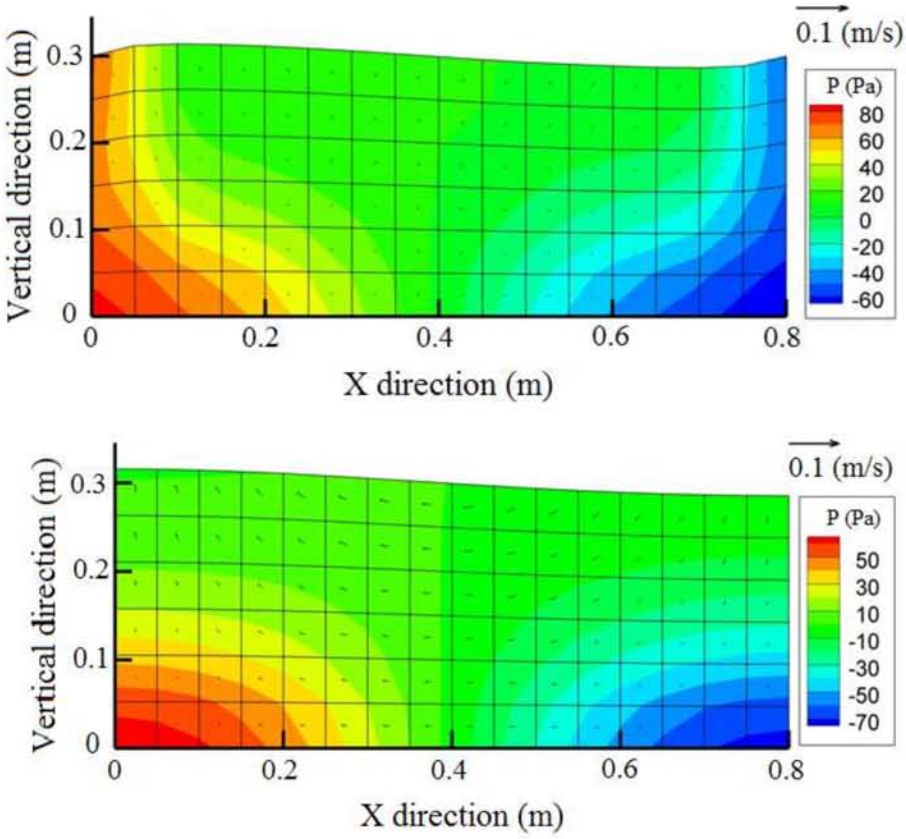

Figure 3.11. Distribution of liquid pressure after 15 cycles.

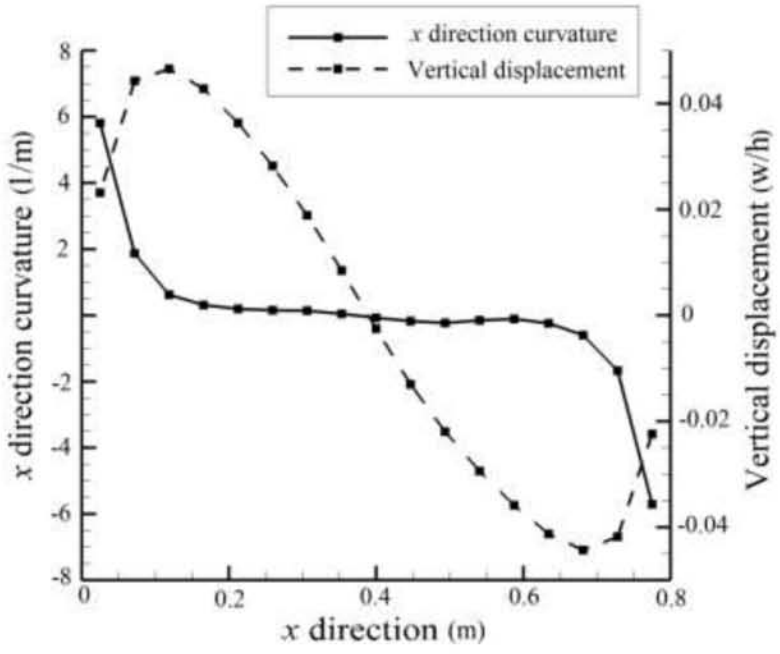

Figure 3.12. Relationship of surface external force and curvature.

3.3. Conclusion

Membrane-liquid interaction problems, including both geometry nonlinearity due to large liquid deformations and material nonlinearity of the membrane, were presented. We considered the moving boundary in the liquid region by coupling the arbitrary Lagrangian-Eulerian finite element method with the Lagrangian method for membrane elements. The time history response, liquid behavior and membrane behavior are calculated and compared with the results obtained from the sloshing model in the large-deformation domain. Furthermore, we have examined the balance of forces in the interaction model to confirm the validity of the results obtained for the deformation. We have arrived at the following conclusions:

(i) The amplitude of the upward displacement is larger than the amplitude of the downward displacement. It is strongly affected by the nonlinearity of the liquid because of the large deformations.

(ii) The frequencies increase when the initial strain and excitation increase but the influence of geometric nonlinearity due to large deformation is small because the behavior is dominated by the initial strain. It was confirmed that moving from the low to high-frequency range of the resonance frequency has a large effect in comparison to the initial strains for the hardening type nonlinearity because the membrane is rubberlike.

(iii) There is a nonlinear relation between the excitation and maximum response. The response shows a sudden exponential increase when the excitation increases. The nonlinear behavior of the excitation amplitude caused by a large deformation in the second area dominates the behavior of the membrane in this area.

(iv) The maximum upward displacement is much larger than the downward displacement and the membrane surface shape is asymmetrical with respect to the center. This asymmetry occurs as the deformation increases. These two phenomena are closely

related to each other.

(v) Equilibrium of the forces between the liquid and membrane has been shown, thus confirming the validity of the analysis in the large-deformation domain. Therefore, it is shown that the material and geometrical nonlinearities of the rubberlike membrane are very important when computing the response to a low initial strain and large excitation. Moreover, applying the arbitrary Lagrangian-Eulerian finite element method to the moving boundary in the liquid region ensures agreement between the movement of the liquid and structure.

CHAPTER 4

A THREE-DIMENSIONAL

4.1 Objectives

The aim of this chapter is to analyze the nonlinear sloshing-like behavior that occurs in containers where liquid is confined by a flexible membrane, such as bladder tanks. The 3D rectangular tank in which the upper liquid surface is covered by a membrane is analyzed and the results are compared with those of a sloshing model. Some nonlinear characteristics are obtained through parametric calculations and the force equilibrium in the liquid–structure interaction is shown to confirm the validity of the analysis. Then, a rectangular tank with the variation of tank depth was introduced for the implementation. The numerical evaluations were performed and the time historical response, natural frequency, and membrane and liquid displacements, liquid velocity and pressure were presented. Finally, the membrane and liquid nonlinear behavior, especially under low tank depth and large excitation, are discussed.

4.2 The principal strain

In previous analyses, solutions of models describing three-dimensional interactions of a rubberlike membrane with liquid have been obtained only for small deformations, with convergence problems occurring for large deformations. It is the calculation method that causes this problem. The principal strain $\bar{E}_a$ is required to calculate the Ogden strain energy function presented in Section 2.4. The principal direction θ is calculated at each integral point following Eq. (13) as described in Section 2.4.2. In previous research, it has been taken that $\theta = 0$ when $E_x - E_y$ is less than some given value. This is because the initial strains in the x and y directions are then equal

($E_{x0} = E_{y0}$), and the denominator is zero at the start of the calculation. In the case of $E_{x0} = E_{y0}$, when $E_x = E_y$, taking $\theta = 0$ is correct because the shear strain is zero. However, small shear strains are ignored and θ become discontinuous, with the result that the calculation fails to converge. In these previous studies, therefore, the calculation is possible only at small deformations domain where the variations in the principal angle θ are sufficiently small that they can be ignored. In the present approach, when $E_x = E_y$ and $\theta = 0$, Eq. (12) is used, and this allows consideration of large deformations.

4.3 Analysis of rectangular tank containing liquid whose upper surface is covered by a membrane

In this model, a complex response due to left–right asymmetry appears when the maximum vertical displacement exceeds 10% of the tank depth. A rectangular tank containing liquid whose upper surfaces are covered by membranes is vibrated horizontally and the dynamic characteristic of the model are considered.

The relationship between the stretch λ and the Cauchy stress σ under uniaxial tension is shown in Fig. 4.1. The dashed line is straight, and thus a nonlinear relationship is confirmed between λ and σ. The maximum deformation is approximately $\lambda = 1.5$ in this model, and the tangential stiffness $\frac{\Delta\sigma}{\Delta\lambda}$ decreases by 6% compared with $\lambda = 1.0$ (strain equal to zero). The membrane density ρ_m is 1.07×10^3 kg/m^3. The liquid is assumed to be water, with a density ρ_l of 1.0×10^3 kg/m^3. The analysis model is shown in Fig. 4.2. The tank dimensions are $\boldsymbol{a} = 0.8$, $\boldsymbol{b} = 0.8$, $\boldsymbol{h} = 0.3$ and the membrane thickness is $t_m = 0.001$ m.

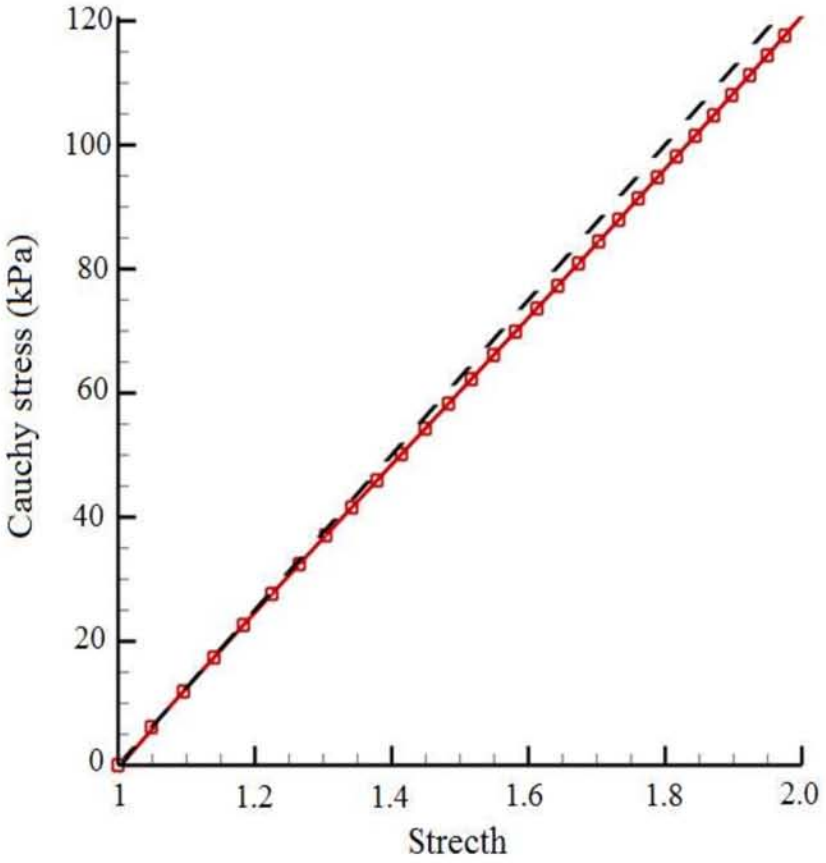

Figure 4.1. The relationship of stretch and Cauchy stress with unaxial tension.

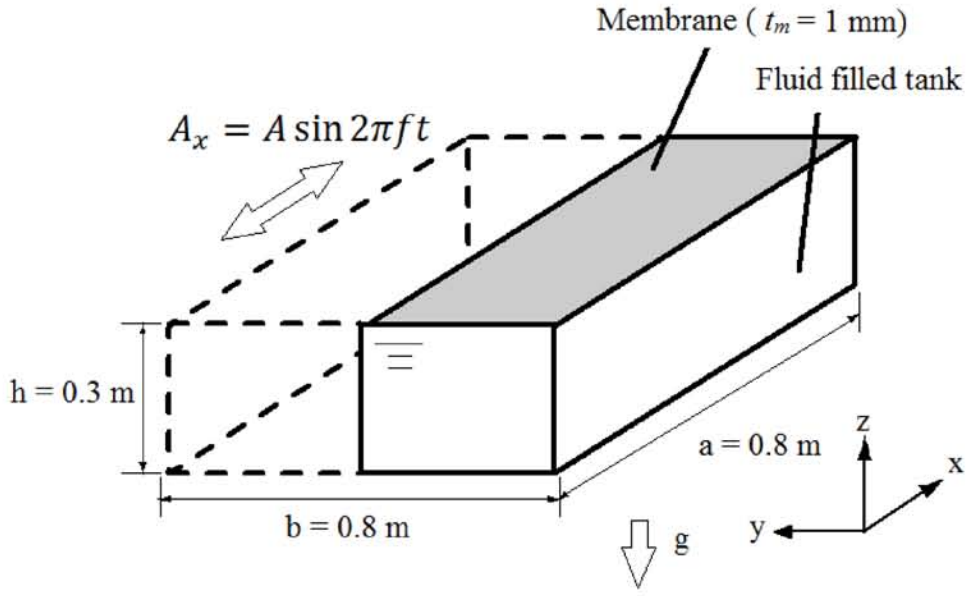

Figure 4.2. The rectangular tank which upper is covered by membrane (1/2 model).

The vibrational acceleration in the x direction is taken to be $A_x = A \sin 2\pi ft$ and the acceleration due to gravity is $g = 9.80\ \mathrm{m/s^2}$. The finite element mesh (half model) for the liquid consisted of 768 (16×8×6) elements. The membrane was divided into 48 (16×8) elements. The time increment in the time integration scheme was 0.002 of one period of the driving acceleration. The influence of the rubberlike membrane is considered in a sloshing analysis. The tank size in the sloshing model is the same as that in the rubberlike membrane–liquid interaction model. The analysis conditions are shown in Table 4.1. For the interaction model, the resonant frequency at the maximum vertical displacement of 5 cycles is used as the vibration frequency. For the sloshing model, the one-degree mode natural frequency of the linear theory is used as the vibration frequency. The linear theory of sloshing is described in Appendix B.

Table 4.1 Analysis condition of first model

	Initial strain		$A\ (\mathrm{m/s^2})$	f (Hz)	Element division		
	E_{x0}	E_{y0}			a	b	h
Interaction model	0.05	0.02	0.01	1.0	16	8	6
Sloshing model	—	—	0.01	0.9	16	8	6

4.3.1 Natural frequency

In this part of the investigation, the excitation acceleration A was varied from 0.01 to 0.08 $\mathrm{m/s^2}$ to examine the natural frequency. The maximum displacement after 5 cycles, made dimensionless using the tank depth, is shown in Fig. 4.3. For the sloshing model, the first mode of the natural frequency is 0.9 Hz according to the linear theory, and this decreases by only 0.3% when the deformation becomes large. This is a nonlinearity of the normal softening type. However, the possibility of the appearance of the internal resonance must be concern. The complicated phenomena wave more occur, in specially for

three-dimensional square tank, when the natural frequencies satisfy internal resonance conditions such as the dimension of liquid tanks, the amplitudes of sloshing, and liquid depths. The internal resonance problems were concerned and described in the literature [54-56].

In the interaction model, the natural frequency is 1.0 Hz at $A = 0.01\ \mathrm{m/s^2}$, which is 10% higher than in the sloshing model. Moreover, the natural frequency at $A = 0.08\ \mathrm{m/s^2}$ increases by 1.6% from that $0.01\ \mathrm{m/s^2}$. These results agree with the literature from Bauer and Chiba [17, 18] based on Fourier-Bessel series theory that the natural frequency must increase when a free liquid surface was completely covered by a rubberlike membrane, and the magnitude depends on the stiffness of the rubberlike coverage. In this analysis, the influence of geometric nonlinearity is small because the behavior is dominated by the initial strain. In the large-deformation domain, the natural frequency increases, but it shows a complex response owing to the left–right asymmetry. Therefore, it is possible to analyze the vertical displacement only up to values that are 10% of the tank depth. It is difficult to observe the behavior in the strong-nonlinearity domain.

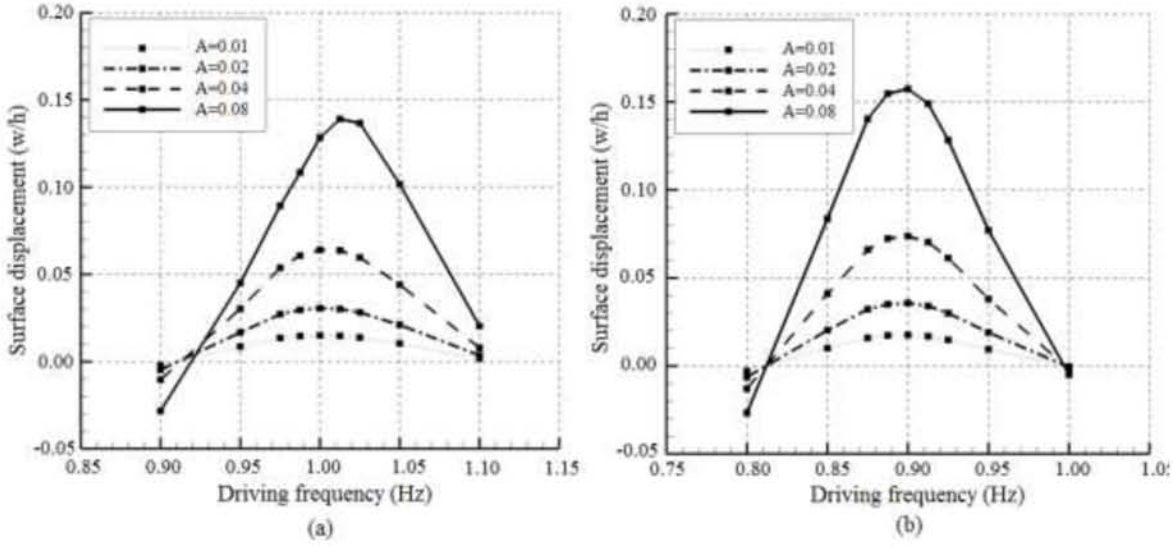

Figure 4.3. Resonant frequency (a) Interaction model (b) Sloshing model.

4.3.2 Flow rate and pressure distribution

The flow rate and pressure distribution of the liquid after 15 cycles are shown in Figs. 4.4 and 4.5 for the liquid–membrane interaction and the sloshing model, respectively: Figs. 4.4(a) and 4.5(a) at at $y = 0.4$ m, and Figs. 4.4(b) and 4.5(b) for the half-model. The pressure distribution is shown with the hydrostatic pressure at each tank depth subtracted. It should be noted that in the sloshing model the flow in the y direction is uniform for an inviscid liquid and the free-surface pressure is zero because the atmospheric pressure is neglected.

After 15 cycles, the flow rate is almost zero in both models. The distribution of liquid pressure in the interaction model, excluding the hydrostatic liquid pressure, after 15 cycles is shown in Fig. 4.4(b). The pressure distribution is large compared with that shown in Fig. 4.5(b) for the sloshing model near the edge of the tank, owing to the prevention of liquid motion by the membrane.

4.3.3 Membrane displacement

Figure 4.6 shows the vertical displacement of the membrane after 15 cycles for the interaction and sloshing models, respectively. The displacement of the upper surface in the sloshing model is maximum at the left end of the tank. In contrast, the displacement of the membrane in the interaction model is maximum at $x = 0.1$ m owing to the presence of a fixed point at the end of the tank.

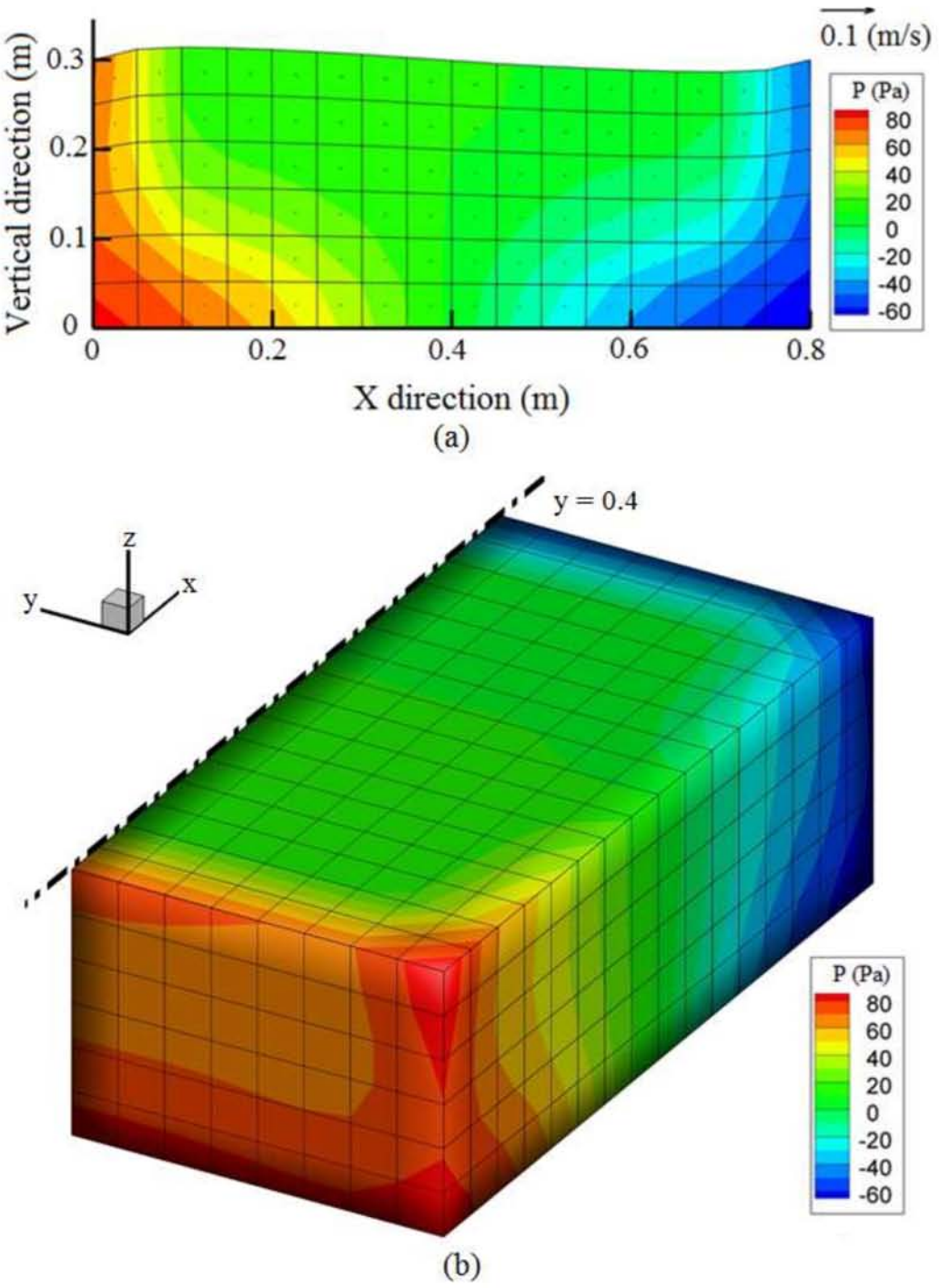

Figure 4.4. The flow rate and pressure distribution of the liquid after 15 cycles in the interaction model.

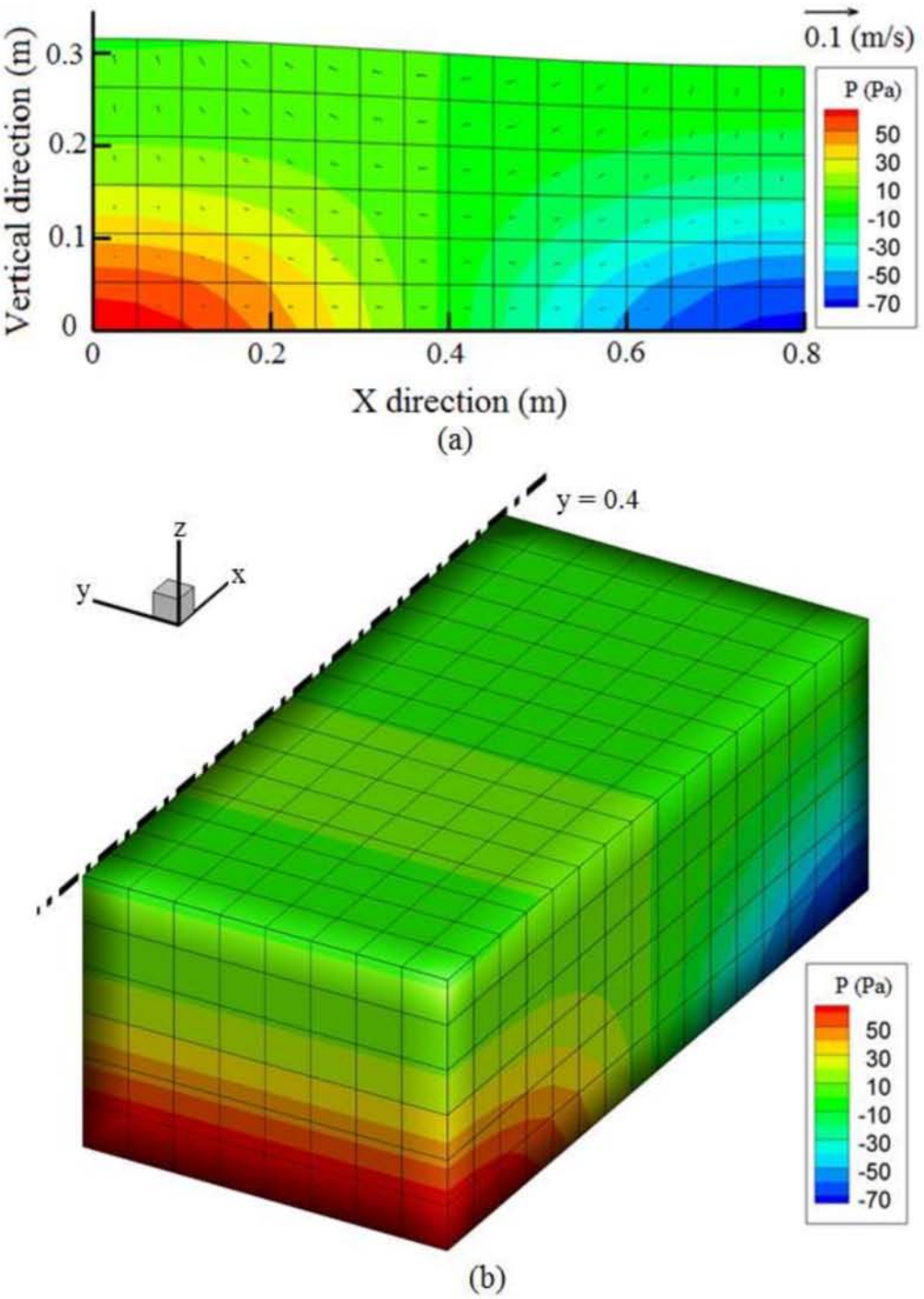

Figure 4.5. The flow rate and pressure distribution of the liquid after 15 cycles in the sloshing model.

The deformations at the surface in both models after 5 and 15 cycles are shown in Fig. 4.6. The solid lines indicate the rubberlike membrane in the interaction model and the dashed lines indicate the sloshing model. The deformation of the membrane near the center of the tank (x = 0.1–0.7 m) in the interaction model is in good agreement with the deformation of the free surface in the sloshing model. The effect of the membrane is strong only near the edge of the tank, where the deformation is constrained by the attachment of the membrane to the tank. As the deformation of the membrane becomes large, it develops a left–right asymmetry, with greater displacement on the upward-displacement side (the left side). After 15 cycles, the zero point is moved to 1.3% of the width on the left-hand side of the container. This asymmetry also appears in the sloshing model. This is due to the presence of a convection term.

The time-history response of the membrane at x = 0.1 m and y = 0.4 m is shown in Fig. 4.7. The deformation is greater here than at any other position if the first vibration mode dominates. The solid line indicates the vertical displacement and the dashed line the excitation acceleration. It can be seen that the amplitude of upward displacement is larger than the amplitude of downward displacement. After 15 cycles, the upward displacement is 5.5% greater than the downward displacement. This phenomenon is often observed in studies of liquid sloshing [12] and is a consequence of the nonlinearity of liquid behavior at large deformation.

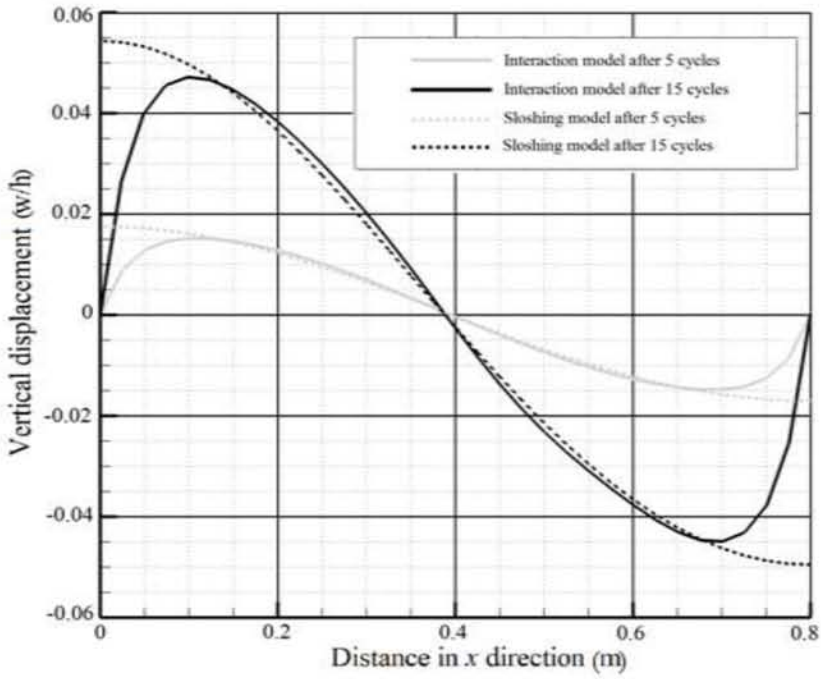

Figure 4.6. Top surface displacement.

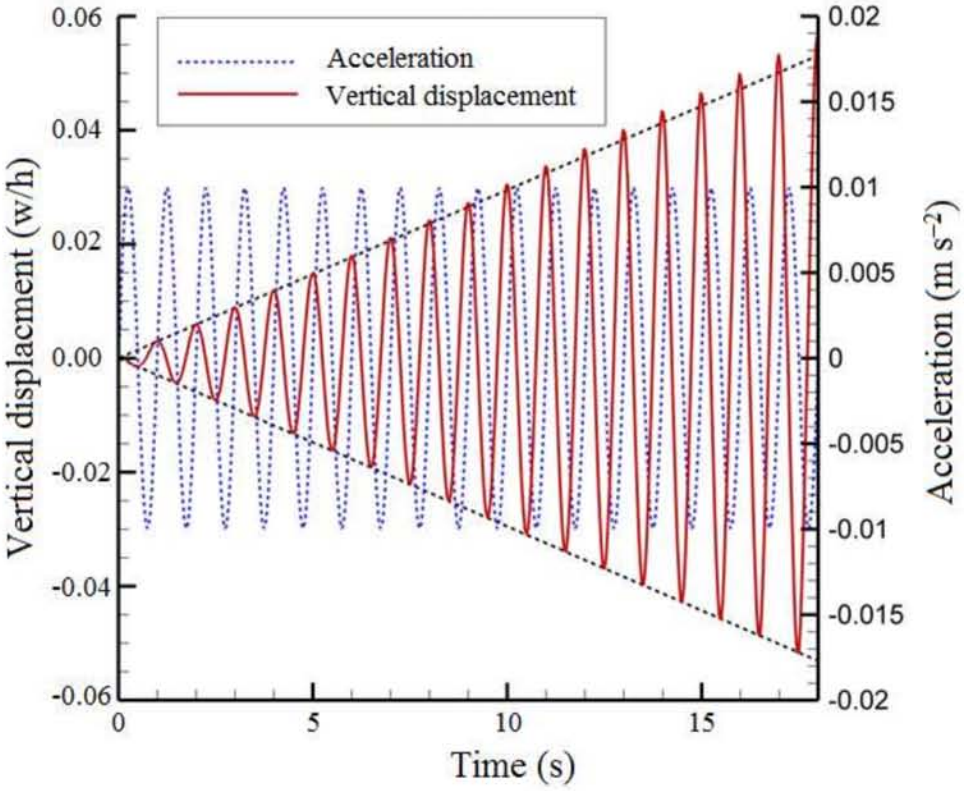

Figure 4.7. Time history response of the membrane vertical displacement.

4.3.4 Strain and stress distributions

The Green–Lagrange strain distribution of the membrane after 15 cycles is shown in Fig. 4.8. Here $E_x, E_y,$ and E_{xy} are defined as follows:

$$E_x = \frac{\partial u}{\partial x} + \frac{1}{2}\left\{\left(\frac{\partial u}{\partial x}\right)^2 + \left(\frac{\partial v}{\partial x}\right)^2 + \left(\frac{\partial w}{\partial x}\right)^2\right\} + E_{x0}, \tag{110}$$

$$E_y = \frac{\partial v}{\partial y} + \frac{1}{2}\left\{\left(\frac{\partial u}{\partial y}\right)^2 + \left(\frac{\partial v}{\partial y}\right)^2 + \left(\frac{\partial w}{\partial y}\right)^2\right\} + E_{y0}, \tag{111}$$

$$E_{xy} = \frac{\partial u}{\partial y} + \frac{\partial v}{\partial x} + \left(\frac{\partial u}{\partial x}\frac{\partial u}{\partial y} + \frac{\partial v}{\partial x}\frac{\partial v}{\partial y} + \frac{\partial w}{\partial x}\frac{\partial w}{\partial y}\right). \tag{112}$$

E_x and E_y are symmetrical because the same initial strain is applied in the x and y directions. The distributions of E_x and E_y are dominated by the out-of-plane deformation.

In other words, the nonlinear terms $\frac{1}{2}(\partial w/\partial x)^2$ and $\frac{1}{2}(\partial w/\partial y)^2$ in Eqs. (110) and (111) are dominant. When the out-of-plane displacement gradient $(\partial w/\partial x, \partial w/\partial y)$ is large, the pressure is concentrated near the tank edge, where the membrane is attached. The variations of E_x and E_y are small in comparison with the initial strain. On the other hand, the distribution of E_{xy} is dominated by the linear term in Eq. (112), $\partial u/\partial y + \partial v/\partial x$, which results from shear deformation in the x–y plane.

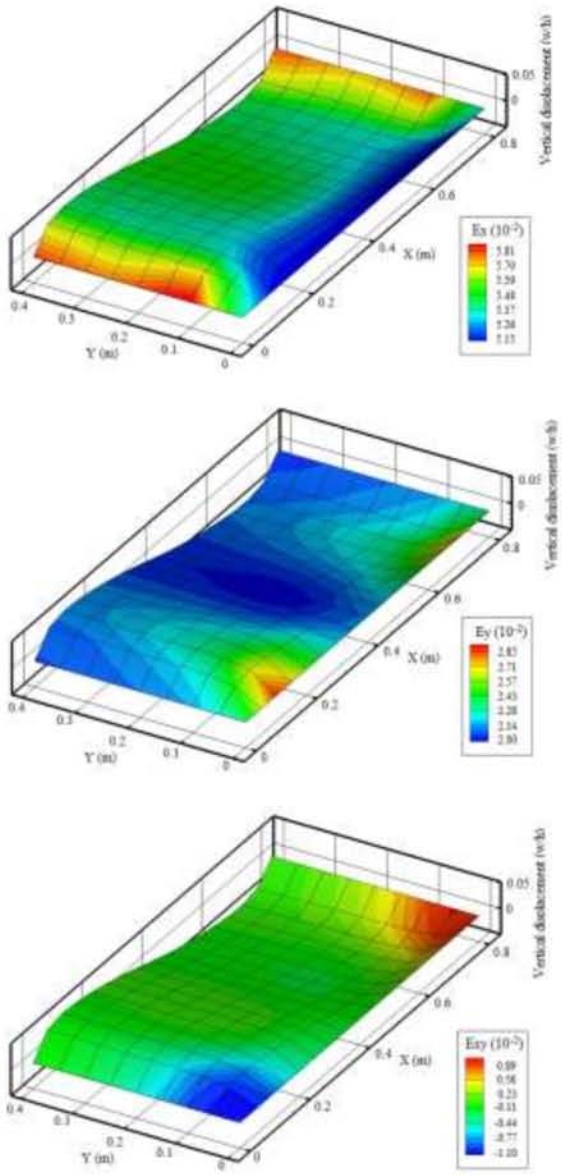

Figure 4.8. The distribution of the Green–Lagrange strain.

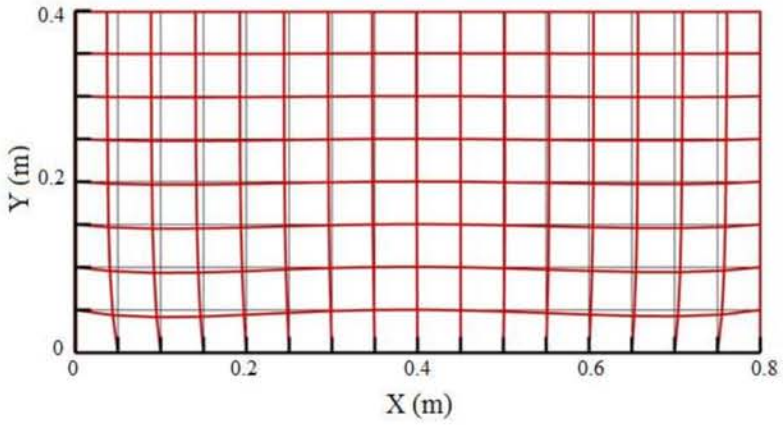

Figure 4.9. X-Y plane deformation after vibration 15 cycles.

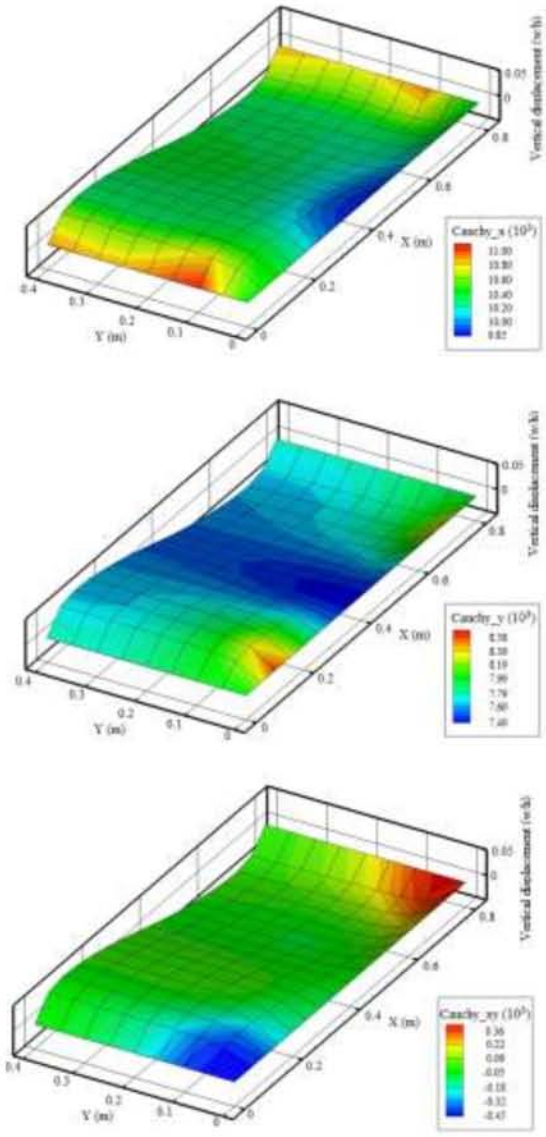

Figure 4.10. The distribution of the Cauchy stress.

The deformation in the x–y plane after 15 cycles is shown in Fig. 4.9. There is large shear deformation near the corner, which is consistent with the distribution of E_{xy}. E_{xy} near the corner is dominated by the nonlinear term resulting from the out-of-plane deformation. In this model, the pressure is concentrated where the membrane is restrained. The shear deformation is due to a tension force generated in a direction inclined at 45° to the x-axis. Elsewhere, the liquid pressure shows a relatively uniform distribution, with no strong concentration. The Cauchy stress distribution is shown in Fig. 4.10. The stress distribution is almost the same as the strain distribution, for the same reasons.

4.3.5 Equilibrium of forces in the liquid–structure interaction

To demonstrate the validity of the results obtained here for the deformation, the equilibrium of forces in the liquid–structure interaction will be examined. We consider a membrane without bending stiffness subject to liquid pressure that produces stress and curvature in the membrane. The equilibrium equation in the out-of-plane direction can be shown to take the following form [12]:

$$\frac{\bar{\sigma}_1 t_m}{r_1} + \frac{\bar{\sigma}_2 t_m}{r_2} = -\pi_f + \rho_m t_m \mathbf{a} \cdot \mathbf{n}_s, \tag{113}$$

where $\bar{\sigma}_1$, $\bar{\sigma}_2$ and r_1, r_2 are the Cauchy stresses and radii of curvature, respectively, in the principal direction, t_m is the film thickness, π_l is the liquid pressure, $\mathbf{a}$ is the membrane acceleration, and $\mathbf{n}_s$ is the normal vector of the structure. The right-hand side of this equation represents the external force per unit area, with the first term being the liquid pressure force applied to the membrane and the second term the inertial force on the membrane. Figure 4.11 is a graphical representation of the forces in Eq. (113), where Z denotes the sum of the external forces.

The membrane is supported by the component of the sectional force in the out-of-plane direction, which is equivalent to the external force. For this reason, if the curvature is small (i.e., the radius of the curvature is large), the component in the out-of-plane direction will be small, and the external force will also be small. In contrast, if the curvature is large, the component in the out-of-plane direction will be large, and the external force will also be large. The Cauchy stress is dominated by the initial tension. The differences between the maximum and minimum tensile stresses in the x and y directions are only 11% and 16%, respectively, and the distribution appears to be uniform. The external force applied to the membrane by the liquid is due only to liquid pressure because of the assumption that the liquid is inviscid. The distributions of the curvature and pressure must match in order to satisfy Eq. (113).

The distribution of the liquid pressure with the exclusion of the hydrostatic pressure after 15 cycles is shown in Fig. 4.12. The pressure change is large near the edge of tank, where liquid motion is prevented by the attachment of the membrane. The initial strain is dominant with respect to the stress on the membrane. Therefore, the strain remains almost unchanged from the initial strain (10%) and it is nearly uniform.

The curvatures in the x direction at $y = 0.4\,\mathrm{m}$ and in the y direction at $x = 0.1\,\mathrm{m}$ are shown in Fig. 4.13. The curvature in the x direction is large near the edge of the tank but is almost zero elsewhere. The curvature in the y direction is also large near the edge of the tank. This is similar to the distribution of liquid pressure.

Figure 4.14 shows the distribution of the membrane sectional force and external force, according to Eq. (113). The distributions of these forces match very well, except near the edge of the tank. The reason for this is that the Cauchy stress and the radius of curvature were calculated in the x–y direction rather than the principal direction. The difference between the forces is large near the edge of tank because of the variation of the strain in the principal direction. Therefore, in this model, it turns out that it is not the stress but rather the curvature that is dominant and supports the liquid pressure. From the above, it can be seen that there is equilibrium between the membrane and the liquid, and the results obtained for the deformation can be considered to be valid. In addition, it should be noted that the FEM analysis was not performed directly, but was formulated using the energy equation. In this case, instead of the natural boundary condition, the mechanical boundary condition was used, and this is difficult to satisfy strictly.

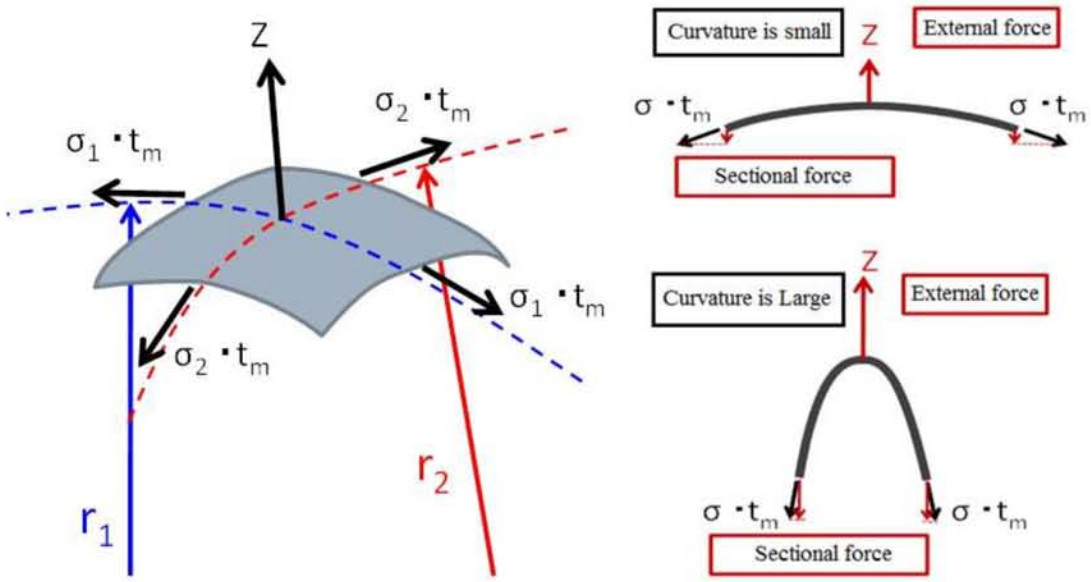

Figure 4.11. The relationship of surface external force and curvature.

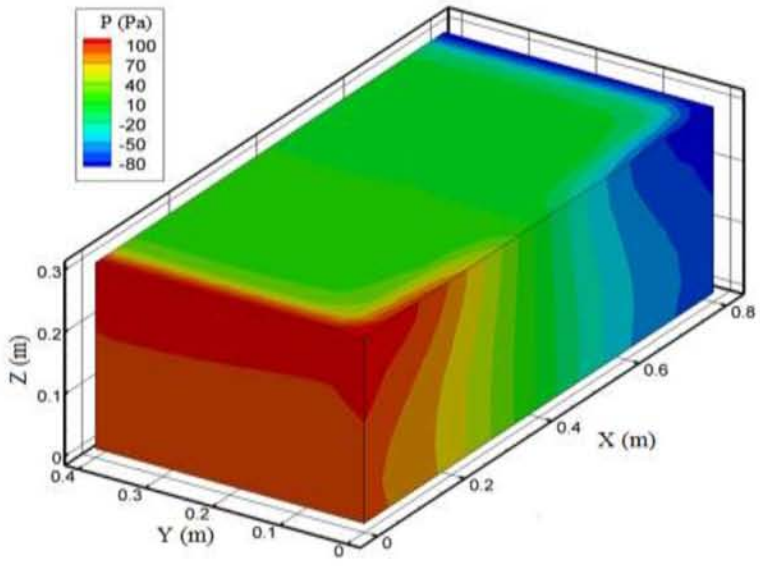

Figure 4.12. The distribution of liquid pressure after 15 cycles.

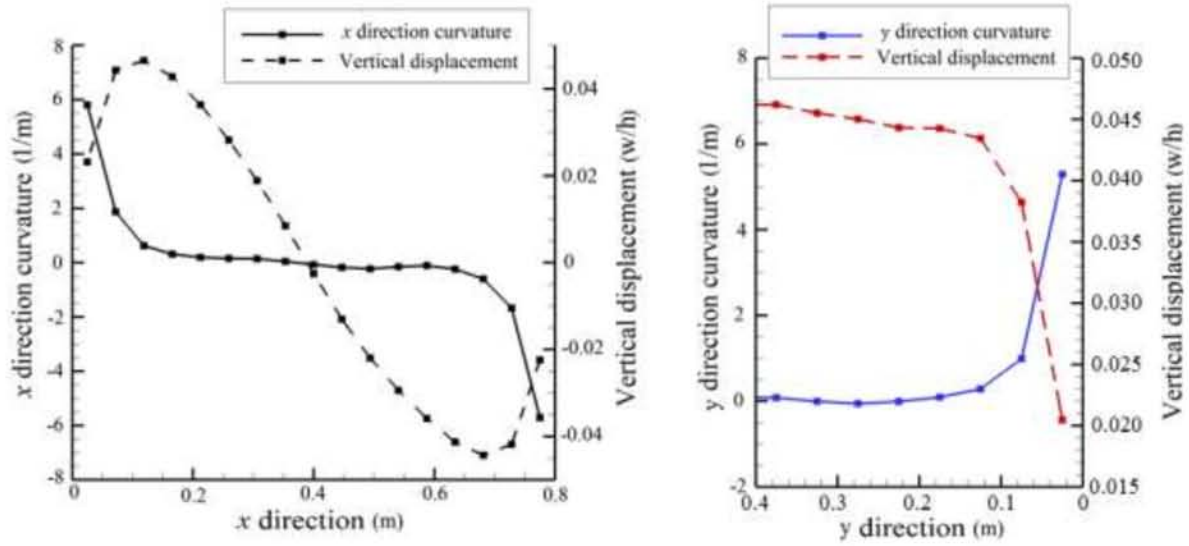

Figure 4.13. The distribution of vertical displacement and curvature after 15 cycles.

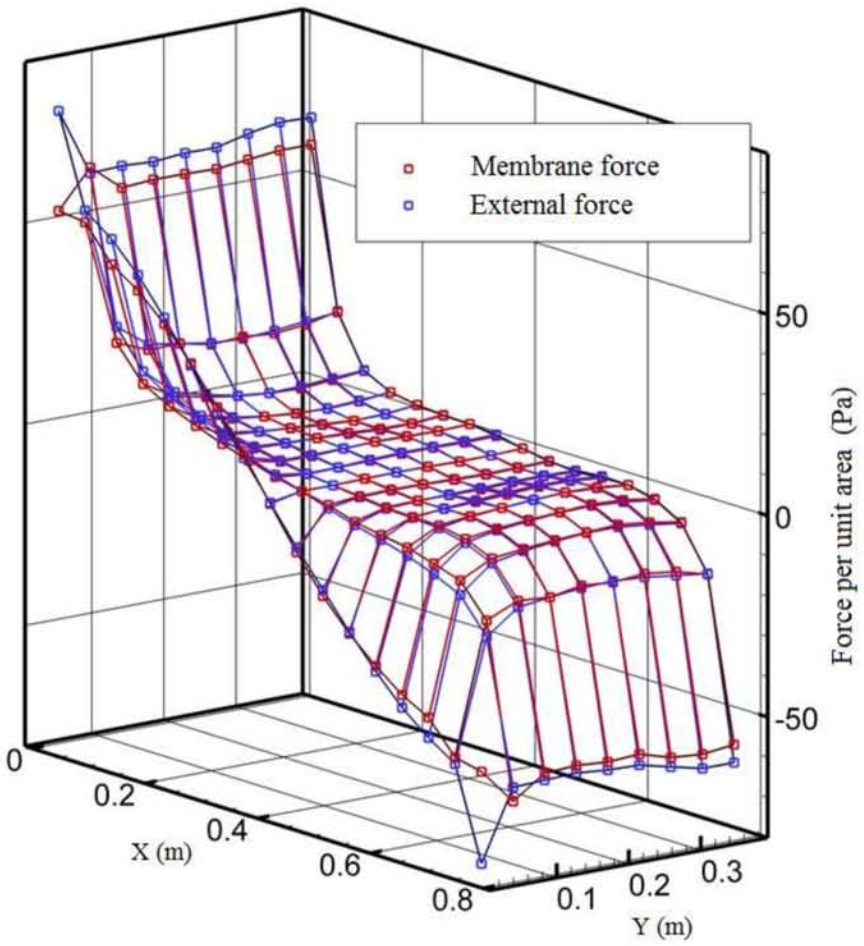

Figure 4.14. The distribution of membrane and external force.

4.4 Implementation of 3-D tank which upper surface is covered by membrane with the variation of tank depth

Considering the rubberlike membrane and liquid interaction model, a rectangular tank of infinite with both width and length of 0.8 m is filled liquid to a height (***h***) m on whose upper surface is covered by membrane as shown in Fig. 4.2. Before explanations, the parameters of numerical model were set up as follows. The width, length and depth of the container size were set with as 0.8 m, 0.8 m and h m respectively, and the membrane thickness was 0.001 m. Gravity is taken account. This membrane was subjected to uniform tension of 4.91 kN/m and 9.60 kN/m with the initial strains in x and y direction are 5% and 2% respectively. The liquid was assumed to be water, namely, the density is 1,000 kg/m^3. The excitation was restricted to be sinusoidal horizontal excitation, and undamped free vibration continues after that. The amplitudes of excitation were fixed at the constant values of 0.01 m/s^2 and 0.1 m/s^2 for small and large deformation, respectively. The variations of tank depth (***h***) were 0.15, 0.3, and 0.45 m.

4.4.1 The frequency response

In this section, the maximum amplitude of the vertical displacement of the membrane at an observation point (0.1 m of tank width) was measured during this free vibration. After four cycles, the oscillation still continued being with approximately constant amplitude. In the Fig. 4.15, it shows the upward displacement of membrane comparison between the small deformation of 0.01 m/s^2 and the large deformation of 0.1 m/s^2 with the variation of tank depth. It is noticed the peak of displacement in the small deformation region are 0.80, 1.00, and 1.06 Hz for the tank depth of 0.15, 0.30, and 0.45 m, respectively.

In the Table 4.2, it shows the excitation frequency comparison between the small deformation of 0.01 m/s^2 and the large deformation of 0.1 m/s^2. For high deformation

region, the frequency are 0.83, 1.02, and 1.08 Hz for the tank depth of 0.15, 0.30, and 0.45 m, respectively, thus the resonance frequency is obtained approximately. As the result of frequency, the peaks of each tank depth are different. At low tank depth of 0.15 m, the resonance frequency is obtained approximately at 0.8 Hz and the resonance frequency increase to be 0.83 Hz that about 3.8% form small to high deformation region. On the other hand, the resonance frequencies of tank depth of 0.30 and 0.45 m increase only 2%.

It can be pointed that the move to high-frequency range of the resonance frequency is large in comparison of tank depth that the hardening type nonlinearity is stronger due to large deformation and low tank depth. We investigate the time historical response of membrane at 0.1 m from the left of tank. This position has larger deformation than any other position if the first vibration mode dominates. The time historical

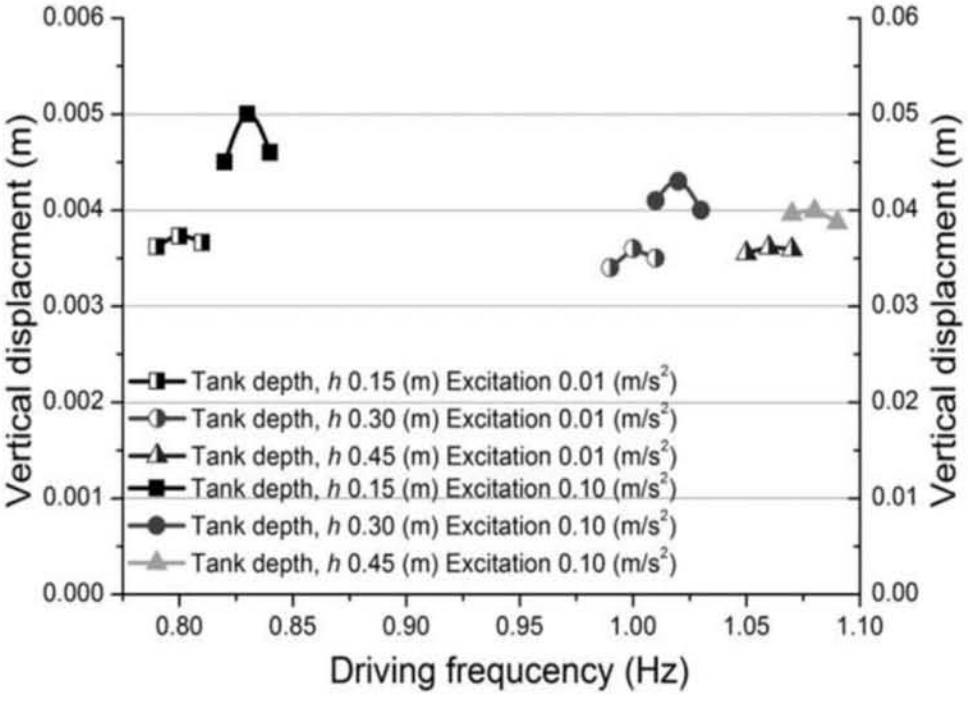

Figure 4.15. Upward displacement vs. frequency.

Table 4.2. The excitation frequency with the variation of tank depth

Excitation (m/s^2)	Tank depth (m)	Excitation frequency (Hz)
Small deformation A= 0.01 m/s^2	0.15	0.80
	0.30	1.00
	0.45	1.06
Large deformation A= 0. 1 m/s^2	0.15	0.83
	0.30	1.02
	0.45	1.08

4.4.2 The time historical response of membrane

We investigate the time historical response of membrane at 0.1 m from the left of tank. This position has larger deformation than any other position if the first vibration mode dominates. The time historical at this point of 0.01 m/s^2 and 0.1 m/s^2 are plotted in Figs. 6 and 7. The driving frequency is given as same as we mentioned before.

From Fig. 4.16, it shows the amplitude of displacement continues increasing with symmetry between upward and downward displacement and accord together with variation of tank depth.

On the contrary, Fig. 4.17 is noticed that the amplitude of upward displacement is about 1.25 times as large as the amplitude of downward displacement. This phenomenon is mainly observed in the study on a liquid sloshing [57] and is strongly affected by the nonlinearity of a liquid due to large deformation. Moreover, the low tank depth of 0.15 m shows larger upward displacement and lower downward displacement as comparison with high tank depth of 0.3 m and 0.45 m.

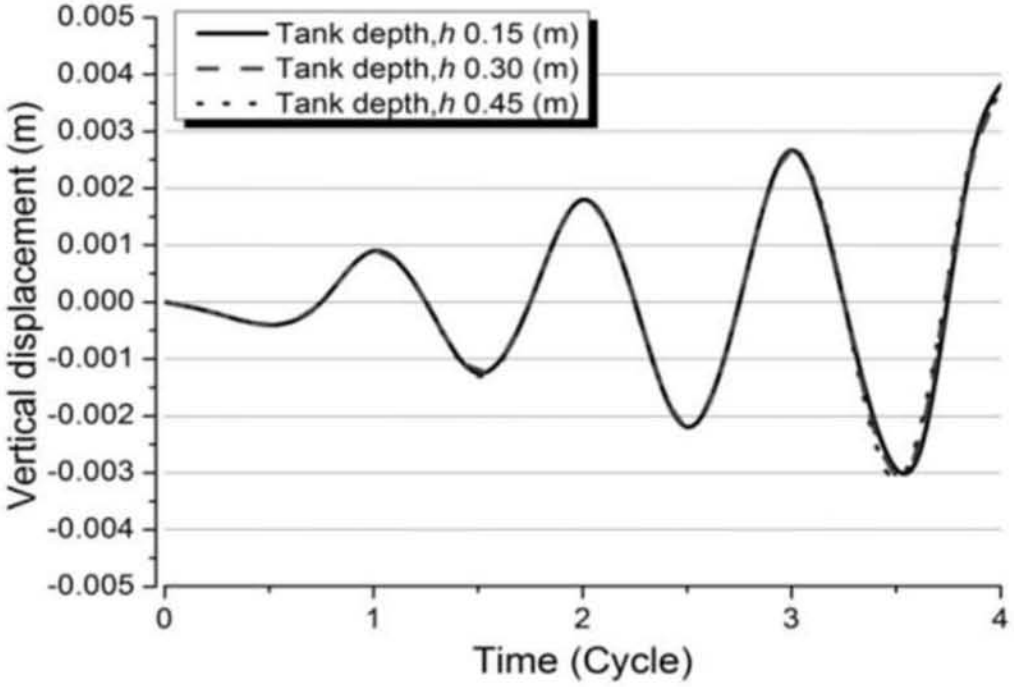

Figure 4.16. Time historical response of 0.01 m/s^2.

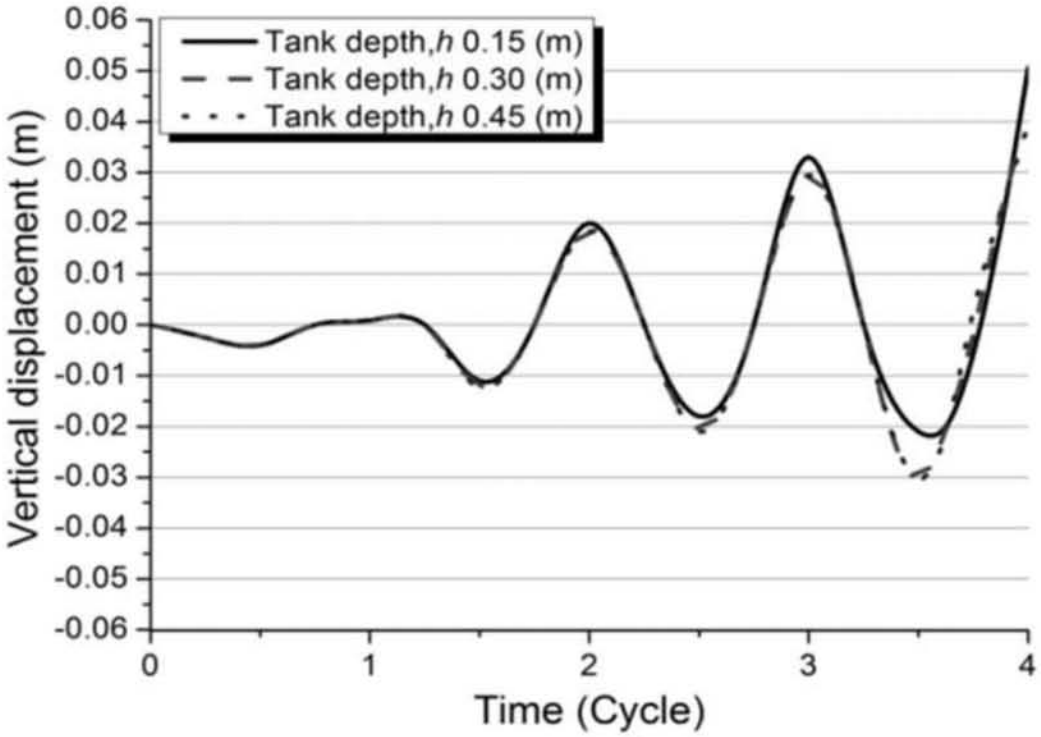

Figure 4.17. Time historical response of 0.1 m/s^2.

4.4.3 Membrane displacement

Due to Fig. 4.18, it represents the deformation profiles of the membrane at 4 cycles with the variation of tank depth and excitation amplitude. At the low excitation of 0.01 m/s^2, the displacement is symmetry and accord together with variation of tank depth. But, the high excitation of 0.1 m/s^2 shows the two characters which cannot observe by linear theory.

First, the maximum upward displacement increases more than the maximum downward displacement, as mention before, and the upward shape becomes sharp simultaneously. The maximum difference between upward and downward displacement occurred at low tank depth of 0.15 m. From the results, it was noticed that the maximum difference occurred at the high excitation of 0.1 m/s^2 and low tank depth of 0.15 m. These kinds of phenomena are well-known in the study of a free surface motion of the liquid and the main factor is the nonlinearity from the convection term of the liquid.

The membrane motion is principally dominated by the liquid motion because of the low depth of the tank and large deformation. Therefore, this sloshing-like motion of liquid is very important to the membrane system. The second is the asymmetry of the deformation as shown in Fig. 4.18. In the other words, if linear theories were employed, this symmetry would have been predicted. Contrary to this, the point which indicates zero vertical displacement shifting to the side of the upward deformation, i.e. to the left side in this figure, with the enlargement of the deformation. In same direction with first character, the maximum occurred at the high excitation of 0.1 m/s^2 and low tank depth of 0.15 m. The comparison of interaction and sloshing model is shown in Fig. 4.19. The result shows the accordance between interaction and sloshing model at large deformation of 0.1 m/s^2 with the tank depth of 0.15 m and 0.3 m. As deformation is large, deformation of membrane becomes left right asymmetry. This asymmetry is also appeared in sloshing model. This is

due to convection term. The sloshing model also confirms that nonlinearities increase due to low tank depth.

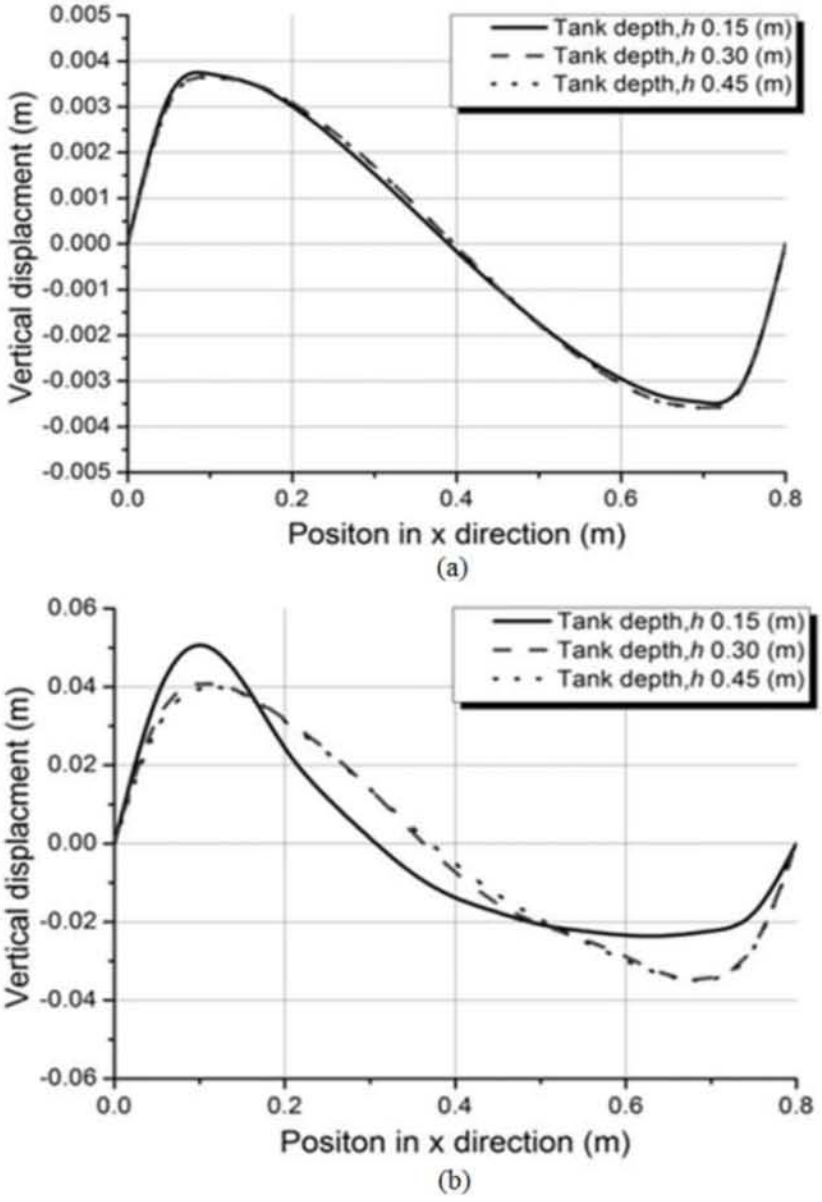

Figure 4.18. Deformation of membrane of (a) 0.01 and (b) 0.1 m/s^2.

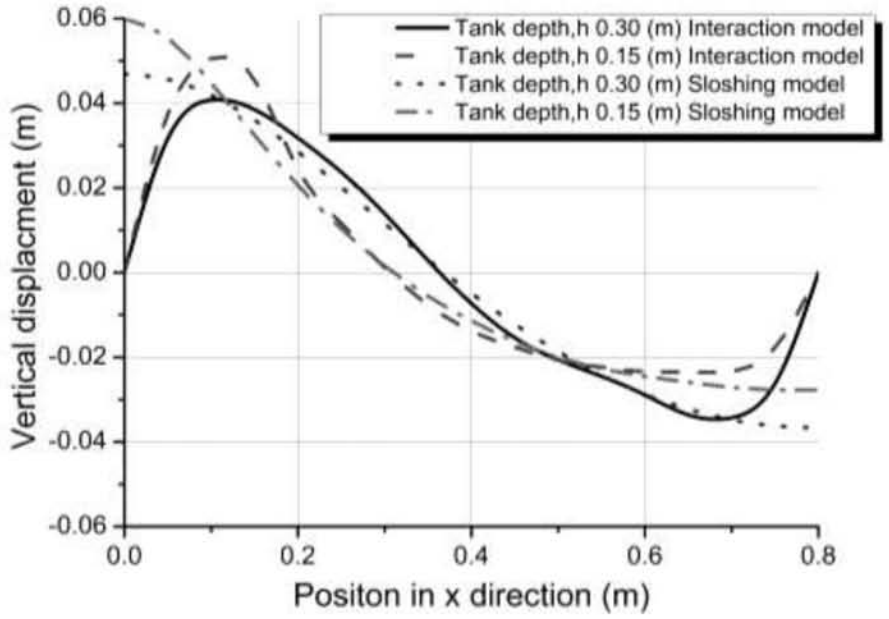

Figure 4.19. Membrane displacement comparison of interaction and sloshing model.

4.4.4 Liquid velocity and pressure

This section, the researchers focus on the causes of strong nonlinearities of liquid flow. Liquid velocity and pressure distribution of the low excitation of 0.01 m/s^2 with the variation tank depth of 0.45, 0.3, and 0.15 m are shown in Figs. 4.20-4.22 respectively. For large excitation of 0.1 m/s^2, the liquid velocity and pressure distribution of the variation tank depth of 0.45, 0.3, and 0.15 m are shown in figure Figs. 4.23-4.25 respectively. The results express liquid flow after 3.625 cycles on (a) xyz-axis and (b) xz-axis at y = 0.4 m. The results showed the strong nonlinearities in low tank depth of 0.15 m, especially on the large deformation region. The liquid velocity and pressure distribution of tank depth of 0.45 and 0.3 m are smaller than tank depth of 0.15 m. The liquid flow of 0.45 and 0.3 m seem to go around the container, but the liquid flow of 0.15 m seems to be obstructed by the bottom of the container and reflect back.

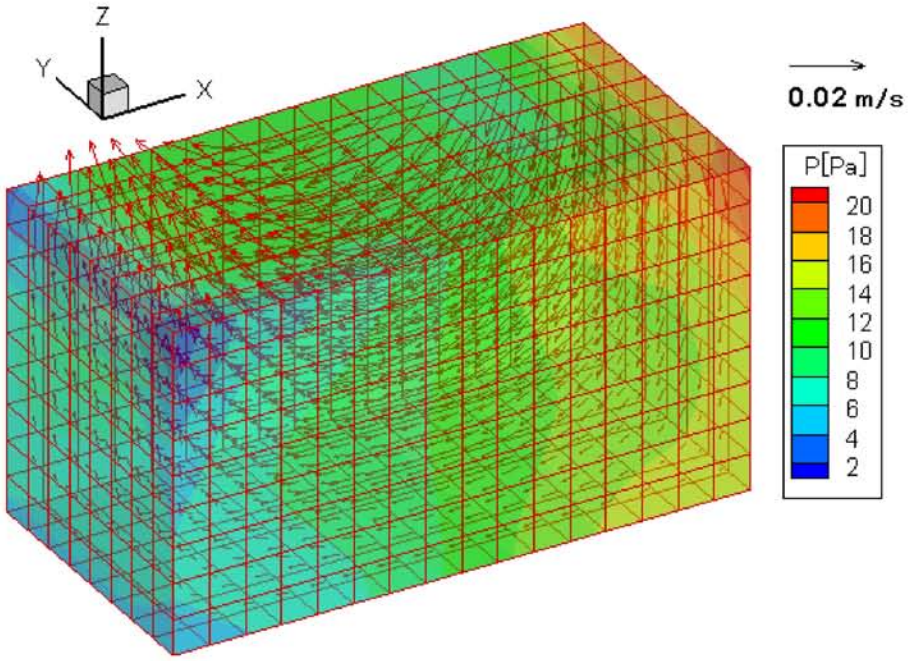

(a) xyz-axis

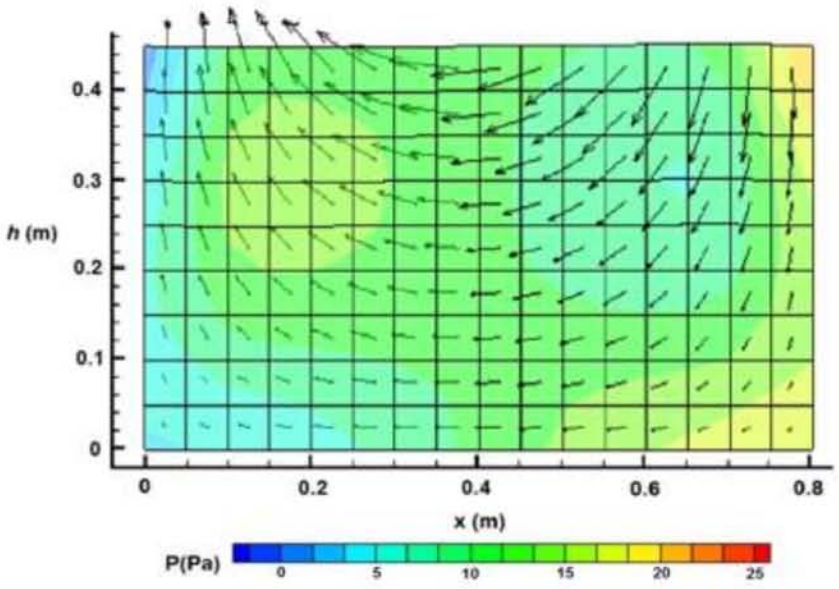

(b) xz-axis at y = 0.4 m

Figure 4.20. Liquid flow after 3.625 cycles at tank depth of 0.45 m and A=0.01 m/s^2.

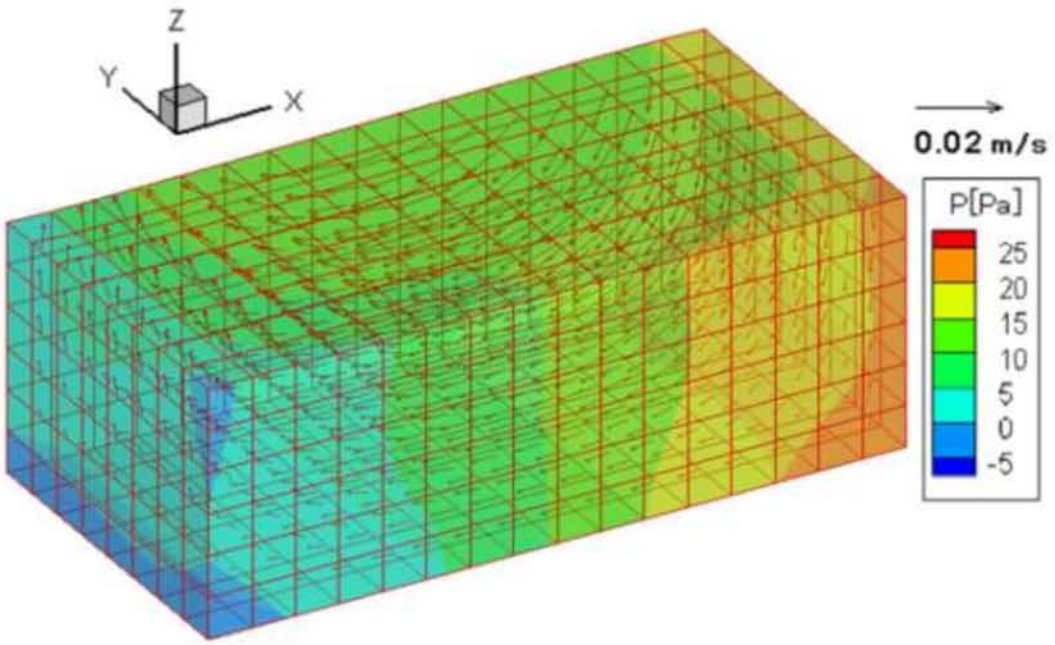

(a) xyz-axis

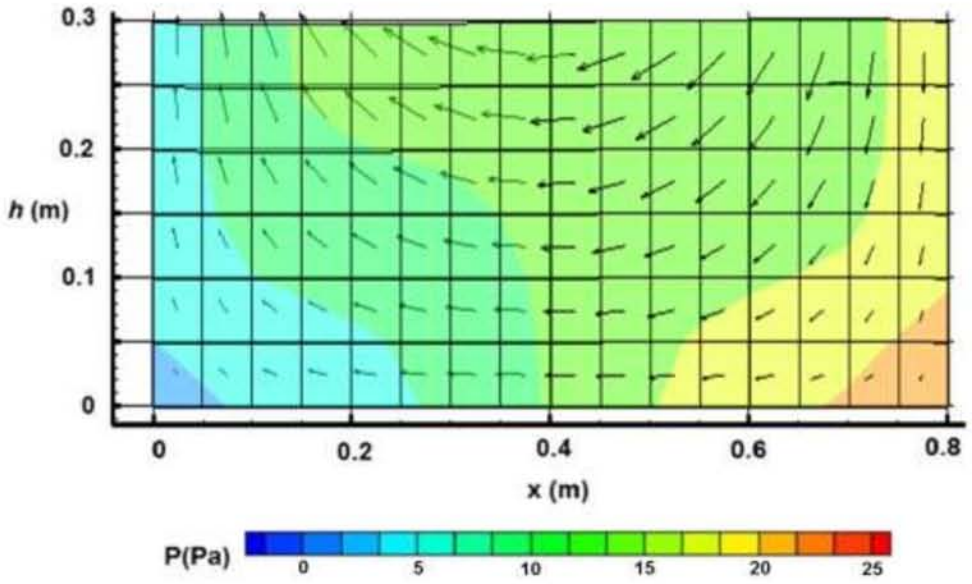

(b) xz-axis at y = 0.4 m

Figure 4.21. Liquid flow after 3.625 cycles at tank depth of 0.30 m and A=0.01 m/s^2.

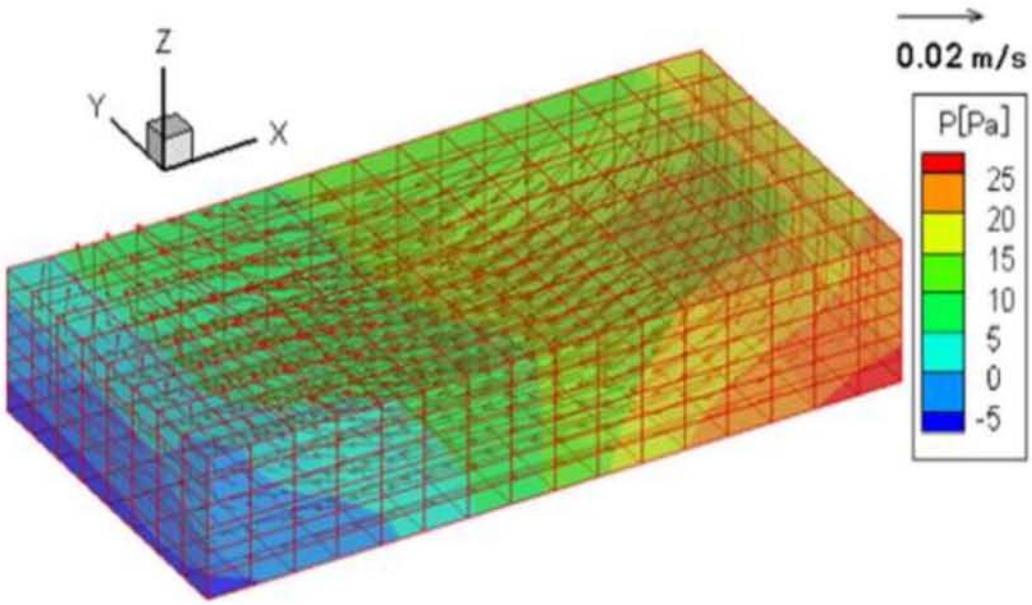

(a) xyz-axis

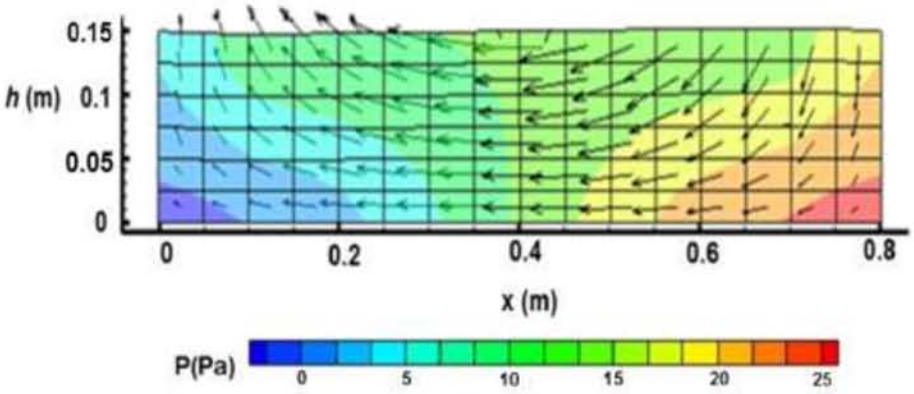

(b) xz-axis at y = 0.4 m

Figure 4.22. Liquid flow after 3.625 cycles at tank depth of 0.15 m and A=0.01 m/s^2.

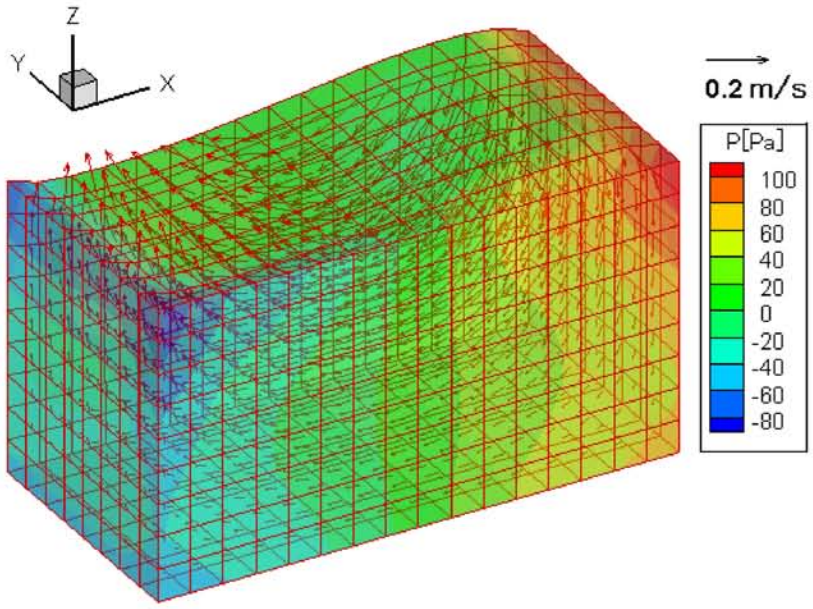

(a) xyz-axis

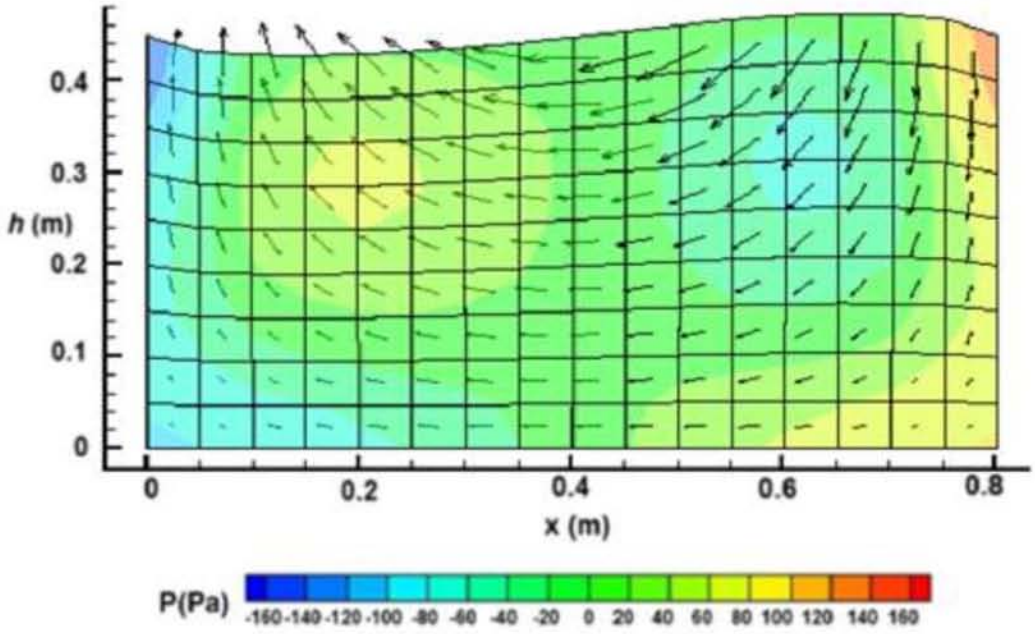

(b) xz-axis at y = 0.4 m

Figure 4.23. Liquid flow after 3.625 cycles at tank depth of 0.45 m and A=0.1 m/s^2.

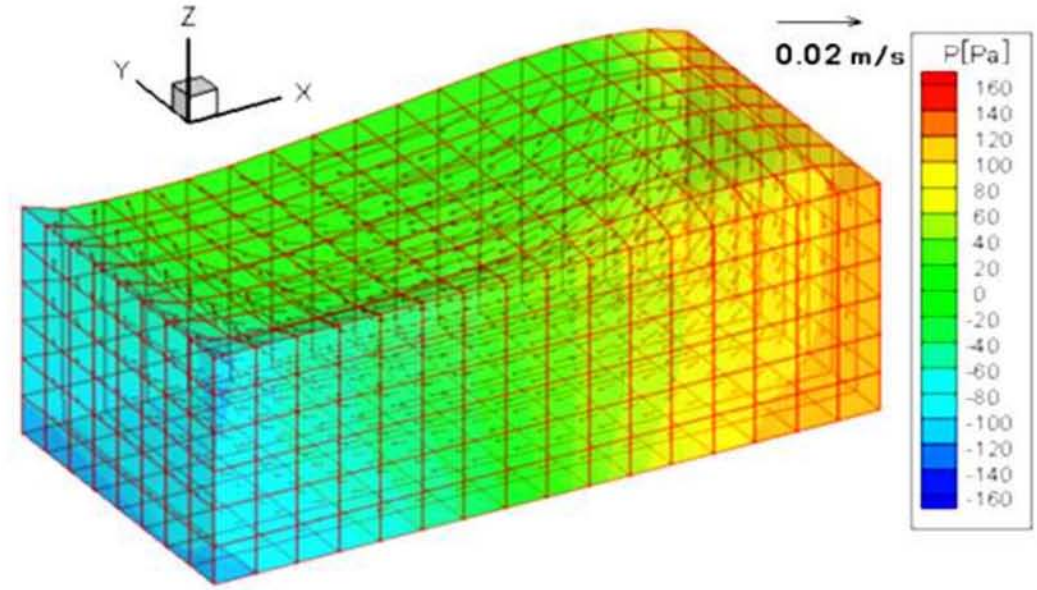

(a) xyz-axis

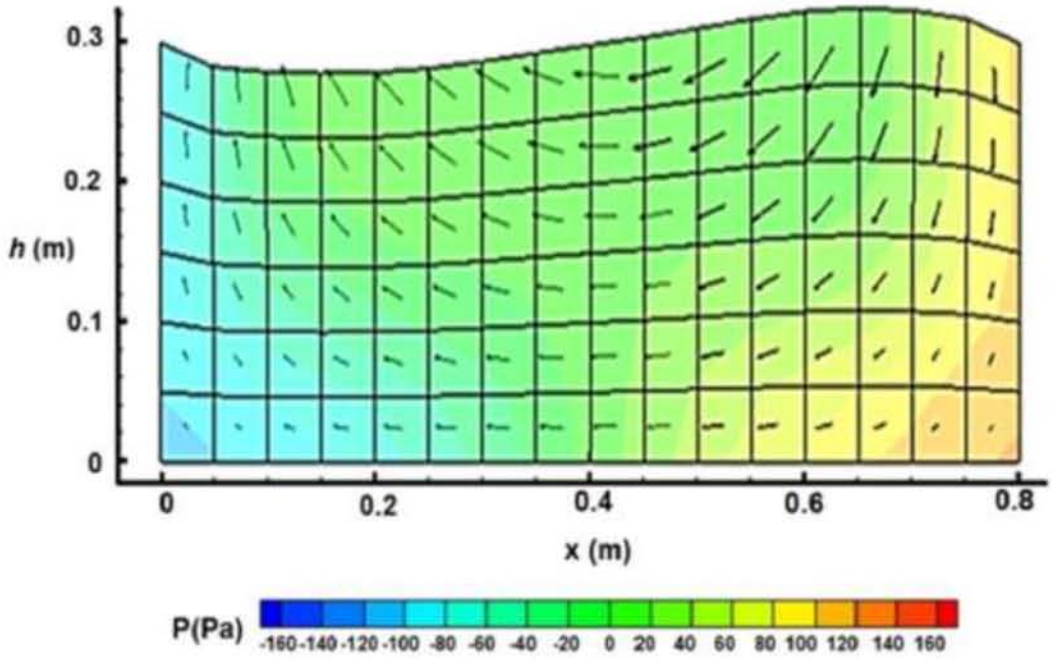

(b) xz-axis at y = 0.4 m

Figure 4.24. Liquid flow after 3.625 cycles at tank depth of 0.30 m and A=0.1 m/s^2.

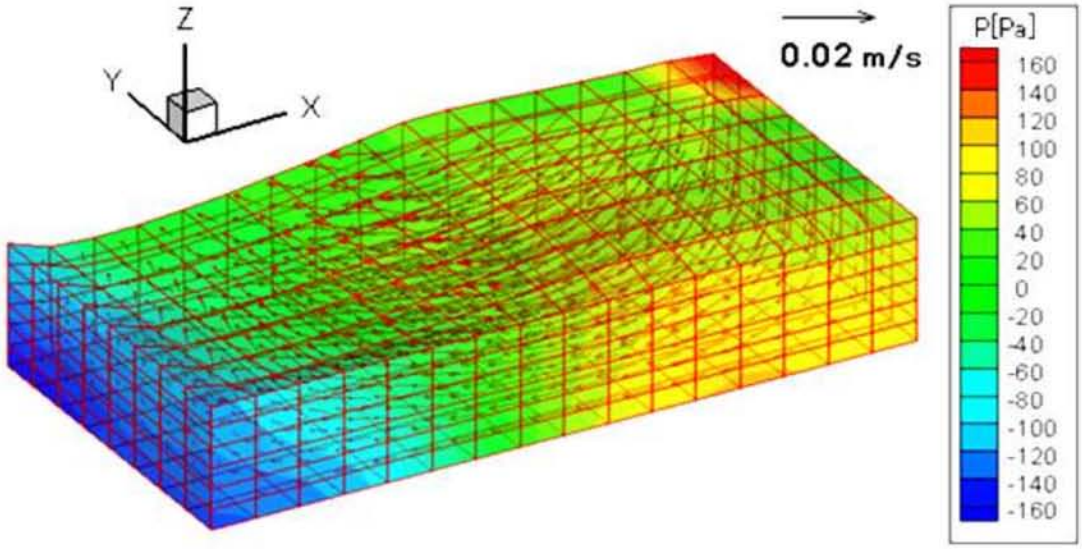

(a) xyz-axis

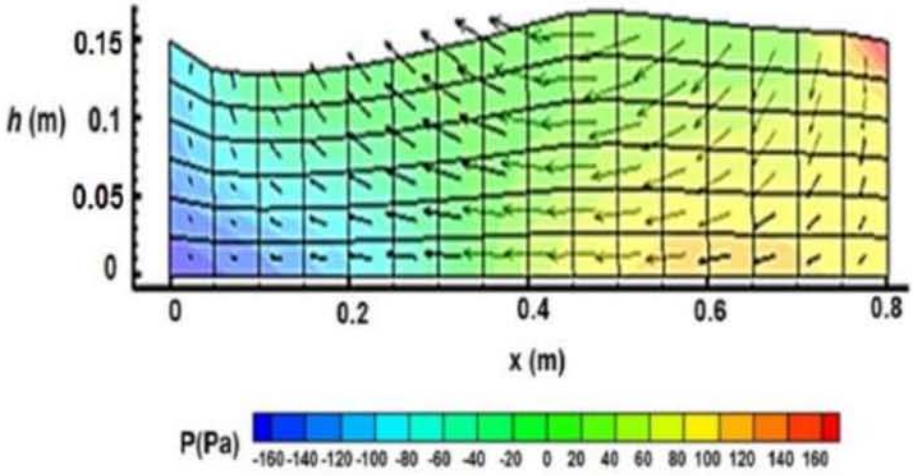

(b) xz-axis at y = 0.4 m

Figure 4.25 Liquid flow after 3.625 cycles at tank depth of 0.15 m and A=0.1 m/s^2.

4.5 Conclusions

In this section, we have analyzed the dynamical characteristics of the interaction model of a rectangular tank containing liquid whose upper surface is covered by a membrane, comparing these with the results obtained from the sloshing model in the large-deformation domain. Furthermore, we have examined the balance of forces in the interaction model to confirm the validity of the results obtained for the deformation. We have arrived at the following conclusions:

1) The influence of membrane strongly appeared in the liquid pressure and deformation, because the movement of liquid was prevented in the area that the membrane was restricted. In other area, the liquid is dominant because it has a good agreement between the free surface displacement of the sloshing model and the membrane displacement of the interaction model.

2) The nonlinearity due to a left-right asymmetry of membrane deformation was observed. At large deformation, the upward displacement is greater than the downward displacement about 5.5% and the central point moves to left side about 1.3%. These phenomena also were found in the sloshing model due to the convection term.

3) The equilibrium of force between liquid and membrane is confirmed and validity of the analysis in large deformation is confirmed.

4) The resonance frequency increases when the liquid moves from low to high excitation, especially on low tank depth model. It can be explained that the move to high-frequency range of the resonance frequency is larger than the frequency of tank depth that the hardening type nonlinearity is stronger due to liquid

5) The amplitude of upward displacement is larger than the amplitude of

downward displacement. It is strongly affected by the nonlinearity of a liquid due to large deformation, especially on low tank depth model.

6) The maximum upward displacement is much larger than downward displacement and the membrane surface shape is asymmetric with respect to the center. This asymmetry occurred along with increasing of deformation and decreasing of tank depth. These two phenomena are closely related to each other.

Therefore, it is proved that the influence of tank depth is very important in the computation when the large excitation is applied. In addition, the behavior of liquid that occurred in sloshing model as same as interaction model, thus movement of liquid is dominant in deformation of rubberlike membrane.

CHAPTER 5

IMPLEMENTATION OF A THREE-DIMENSIONAL

5.1 Objectives

The aim of this paper is to analyze the nonlinear sloshing-like behavior that occurs in containers where liquid is confined by a flexible membrane, such as bladder tanks. The three-dimensional interaction of a rubberlike membrane and liquid problem in a rectangular tank subject to vertical vibration is investigated using the arbitrary Lagrangian–Eulerian finite element method (ALE-FEM). The 3D rectangular tank with upper and lower liquid surfaces covered by membranes is analyzed. The cases of small and large deformation are considered in terms of liquid velocity and pressure distribution, membrane strain and stress distribution, and membrane displacement. The nonlinear behaviors of membrane and liquid, especially under large excitations, are discussed.

5.2 Implementation of rectangular tank containing liquid with membrane-covered upper and lower surfaces

The analysis model is shown in Fig. 5.1. The dimensions of the rectangular tank are $a = 0.3 \times b = 0.3 \times h = 0.3$ m and the membrane thickness is 0.001 m. The maximum vibrational acceleration is $A\,(\mathrm{m/s^2})$ and the acceleration in the z direction $A_z = A\sin 2\pi f t$ is given, where f (Hz) is the vibration frequency. The stresses due to atmospheric pressure on the upper and lower surfaces are ignored because the difference between them is so small. A 1/4 model is analyzed owing to the symmetry in the x and y directions.

The finite element mesh (1/4 model) for the liquid consisted of 432 (6*6*12) elements. The membrane (both side) was divided into 36 (6*6) elements. The time

increment in the time integration scheme was 0.002 of one period of the driving acceleration.

The parameters used for analysis are shown in Table 5.1. The vibration frequency that causes the maximum vertical displacement after five cycles for each vibrational acceleration is used. When $A = 0.001\ \mathrm{m/s^2}$, the analysis is in the small-deformation domain and when $A = 0.1\ \mathrm{m/s^2}$, it is in the large-deformation domain. Each characteristic is considered and then the variations of characteristics due to deformation are considered.

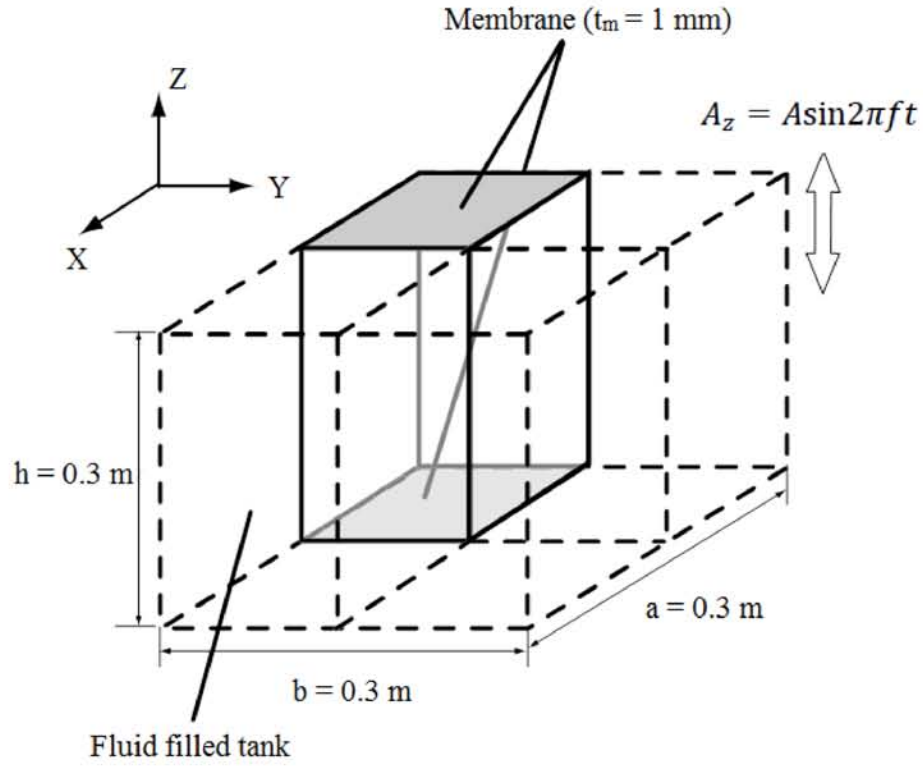

Figure 5.1. The rectangular tank which upper and lower surface is covered by membrane (1/4 model).

Table 5.1 Analysis condition of second model

	Initial strain		A (m/s^2)	f (Hz)	Element division number		
	E_{x0}	E_{y0}			a	b	h
$A = 0.001$	0.05	0.05	0.001	0.71	6	6	12
$A = 0.01$	0.05	0.05	0.01	0.72	6	6	12
$A = 0.1$	0.05	0.05	0.1	0.89	6	6	12

5.2.1 Liquid velocity and pressure distribution

The liquid velocity and pressure distribution after 5 cycles of vibration with accelerations $A = 0.001, 0.01,$ and $0.1\ \mathrm{m/s^2}$ are shown in Figs 5.2-5.4, respectively. A 1/4 model is used owing to symmetry. The liquid velocity and pressure are represented by mesh deformations because they are evaluated on a mesh that deforms due to the use of the ALE method. The pressure and displacement vary in phase with the vibration, while the liquid velocity varies out of phase with the vibration by 0.5π. The maximum pressure and displacement are reached after 5 cycles. $W1$, $W2$, and $W3$ indicate the liquid velocity in the vertical direction at the red point shown in Figs. 5.2(a)-5.4(a) after 4+7/8 cycles. $W1$ is located at the center of the upper surface, $W3$ at the center of the lower surface, and $W2$ is at the center between the upper and lower surfaces, at which point the liquid becomes almost uniform. A comparison of $W1$ and $W3$ with respect to $W2$ is shown in Table 5.2.

In the small-deformation domain, the liquid velocity and pressure show top–bottom inverse symmetry throughout. The mesh displacement becomes maximum after 5 cycles, but the maximum vertical displacement of the membrane is 0.5% of the tank depth and therefore the mesh is almost free of deformation.

After 4+7/8 cycles, the membrane is deformed by the force of the liquid, and the liquid flows along the membrane at the lower surface and perpendicular to the membrane at the upper surface for the large-deformation domain. Then $W1 < W3$, as shown in Table 5.2, and the liquid velocity at the center of the lower surface is higher than that at the center of the upper surface. This is because the liquid concentrates at the center of the membrane at the lower surface. After 5 cycles, the pressure is high at the center of the membrane at the lower surface, where there are large variations in the liquid velocity, while the liquid velocity is uniform near the upper surface.

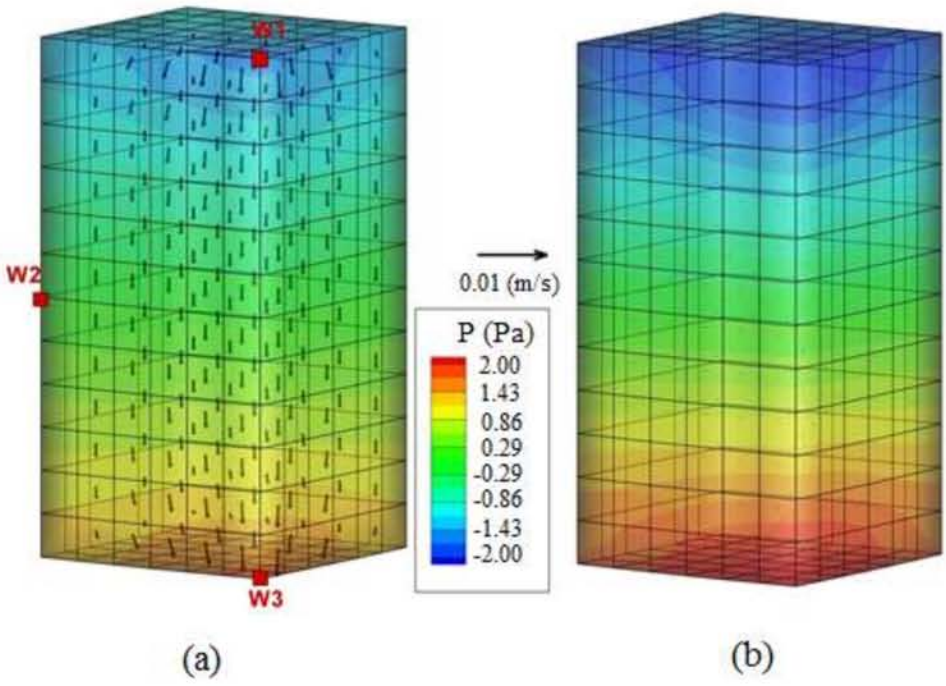

Figure 5.2. Liquid velocity and pressure distribution when A = 0.001 m/s^2

(a) 4+7/8 cycles and (b) 5 cycles.

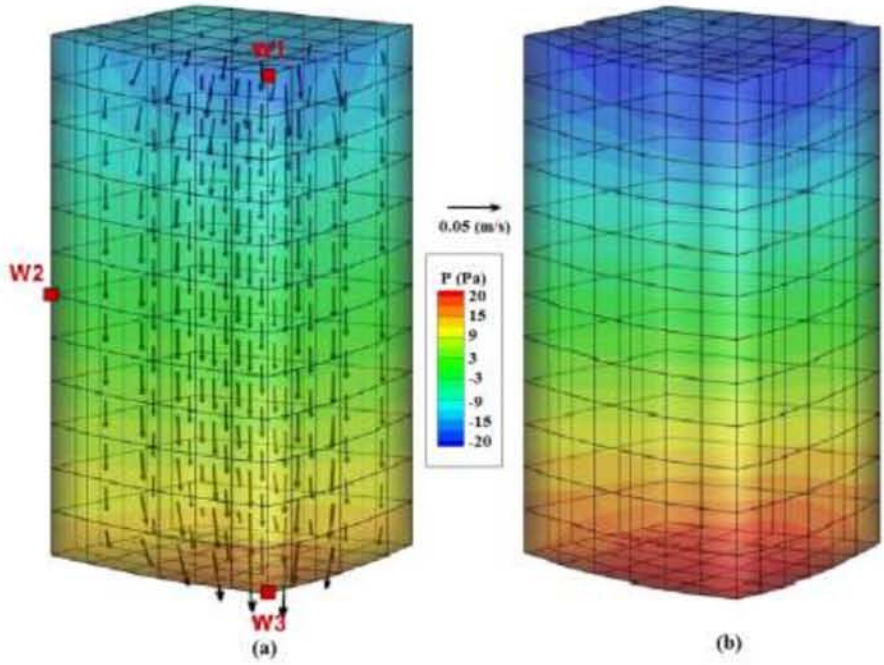

Figure 5.3. Liquid velocity and pressure distribution when A = 0.01 m/s^2

(a) 4+7/8 cycles and (b) 5 cycles.

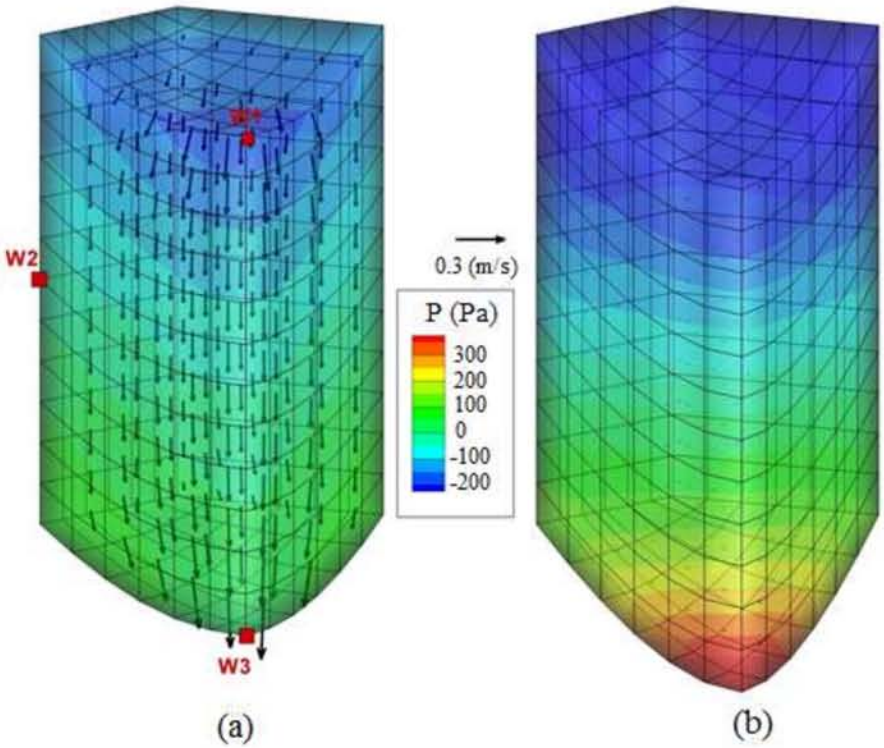

Figure 5.4. Liquid velocity and pressure distribution when A = 0.1 m/s^2

(a) 4+7/8 cycles and (b) 5 cycles.

Table 5.2 Liquid velocity in vertical direction after 4+7/8 cycles

	$W1/W2$ (center of upper surface)	$W3/W2$ (center of lower surface)
$A = 0.001$	1.98	1.99
$A = 0.01$	1.96	2.04
$A = 0.1$	1.99	2.39

5.2.2 Membrane displacement

The membrane vertical displacement, made nondimensional using the tank depth, after 5 cycles of vibration at accelerations $A = 0.001$, 0.01, and $A = 0.1\ \mathrm{m/s^2}$, is shown in Figs. 5.5-5.7, respectively. The red line indicates the upper surface and blue dotted line the lower surface. Owing to symmetry, a 1/4 model is shown, for $y = 0.15$ m. The vertical displacements at the upper and lower surfaces, made nondimensional using the tank depth, are shown in Table 5.3, together with their difference. The membrane deformations at the upper and lower surfaces for vibrational accelerations $A = 0.001$ and $0.1\ \mathrm{m/s^2}$ after 4+3/4 cycles are shown in Figs. 5.8 and 5.9, respectively, from which it can be seen that the sign of the displacement changes.

For small deformation, the rubberlike membrane is attached at the tank periphery while elsewhere it deforms in a hill-like shape as shown in Fig. 5.5. According to Table 5.3, the difference in maximum vertical displacement at the upper and lower surfaces is 0.0012% of the tank depth, and therefore the displacements of these surfaces can be taken to be the same and to show top–bottom symmetry like the liquid velocity and pressure. The curvature of the membrane is supported by stress from the liquid. The curvature is large near the center of the membrane, with the deformation become close to a sharp peak, whereas it small near the tank periphery. In the case of deformation after about 4+3/4 cycles shown in Fig. 5.8, the sign of the deformation reverses simultaneously throughout

the membrane. Therefore, in this situation, it appears that the behavior can be represented by a mode vector as in the analysis of natural vibrations, and the vibration of the membrane is almost linear.

For large deformation, the difference between the upper and lower maximum vertical displacements is 2.8% of the tank depth, as shown in Table 5.3, and the deformations of the upper and lower membranes are different, thus exhibiting a top–bottom asymmetry. At the center of the membrane, the lower surface deformation is large. On the other hand, around the tank periphery, the upper surface deformation is large. Thus, for the upper surface, the curvature is the same all around the membrane, whereas for the lower surface, the curvature is large only at the center of the membrane. This trend is similar to that of the pressure distribution. The maximum vertical displacement is 31% of the tank depth, so the analysis has to take account of large deformations. In the case of membrane deformation after about 4+3/4 cycles, the pressure is concentrated at the tank periphery where the membrane is attached, and the deformation reverses sign earlier than in other regions. There is no time at which the membrane displacement is zero all around the membrane, so this is nonlinear vibration.

Table 5.3 Maximum vertical displacement after 5 cycles

	Center of upper surface, w/h	Center of lower surface, w/h	Difference of upper and lower surface, w/h
$A = 0.001$	-5.18×10^{-3}	-5.19×10^{-3}	1.16×10^{-5}
$A = 0.01$	-5.00×10^{-2}	-5.11×10^{-2}	1.08×10^{-3}
$A = 0.1$	-2.77×10^{-1}	-3.05×10^{-1}	2.80×10^{-2}

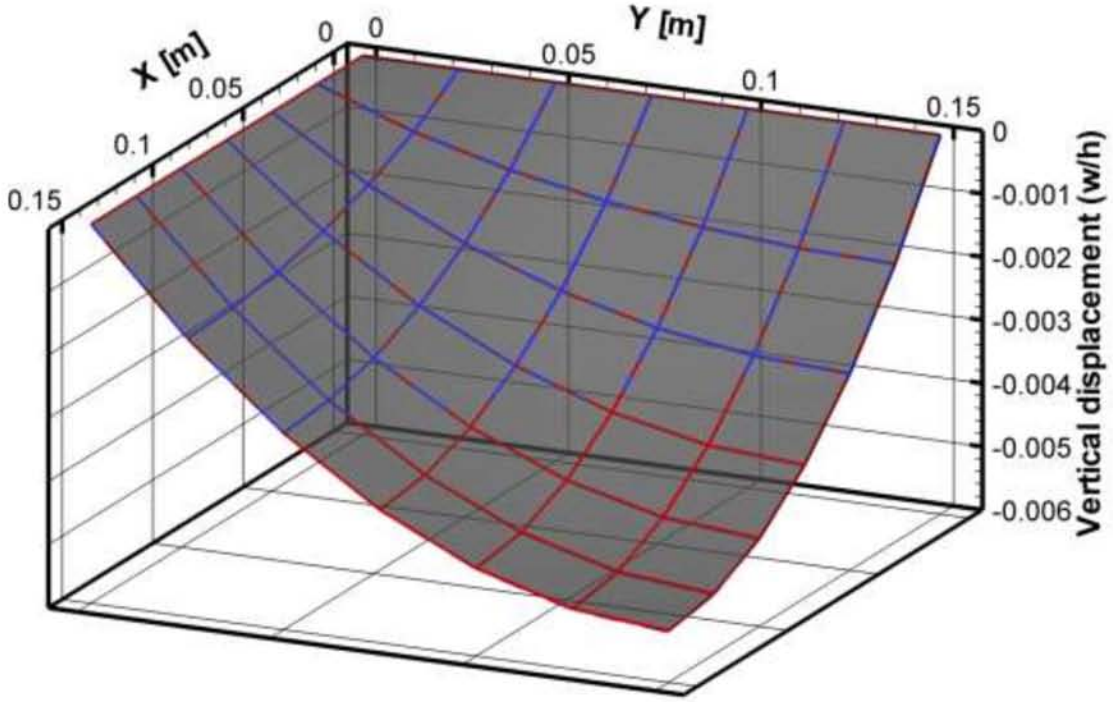

(a) 1/4 part

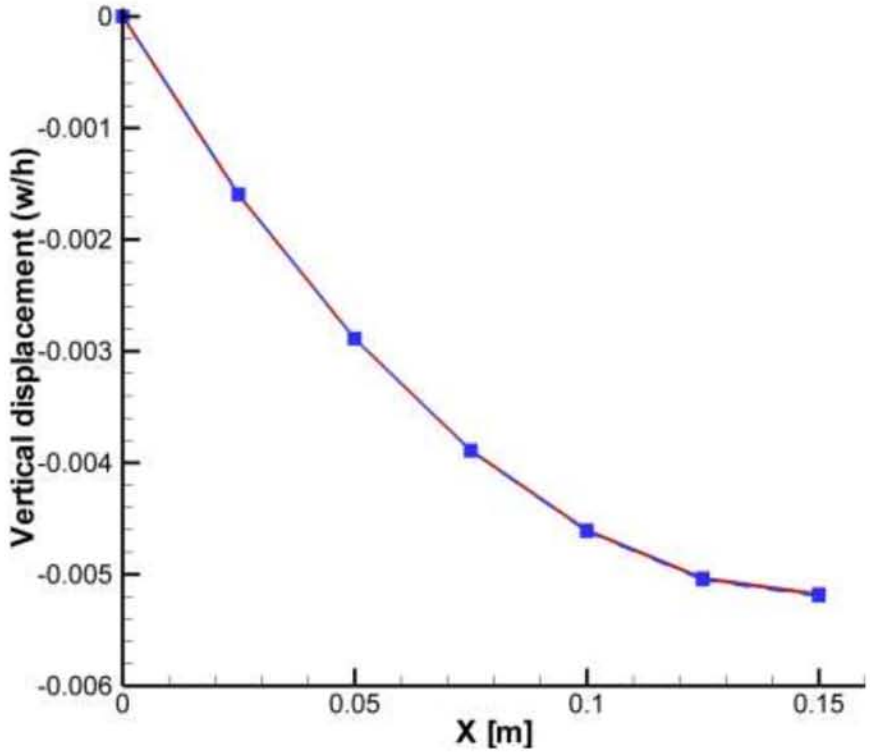

(b) y=0.15(m)

Figure 5.5. Upper and lower membrane deformation after 5 cycles (A=0.001).

(Blue line indicate lower surface, red line indicate upper surface)

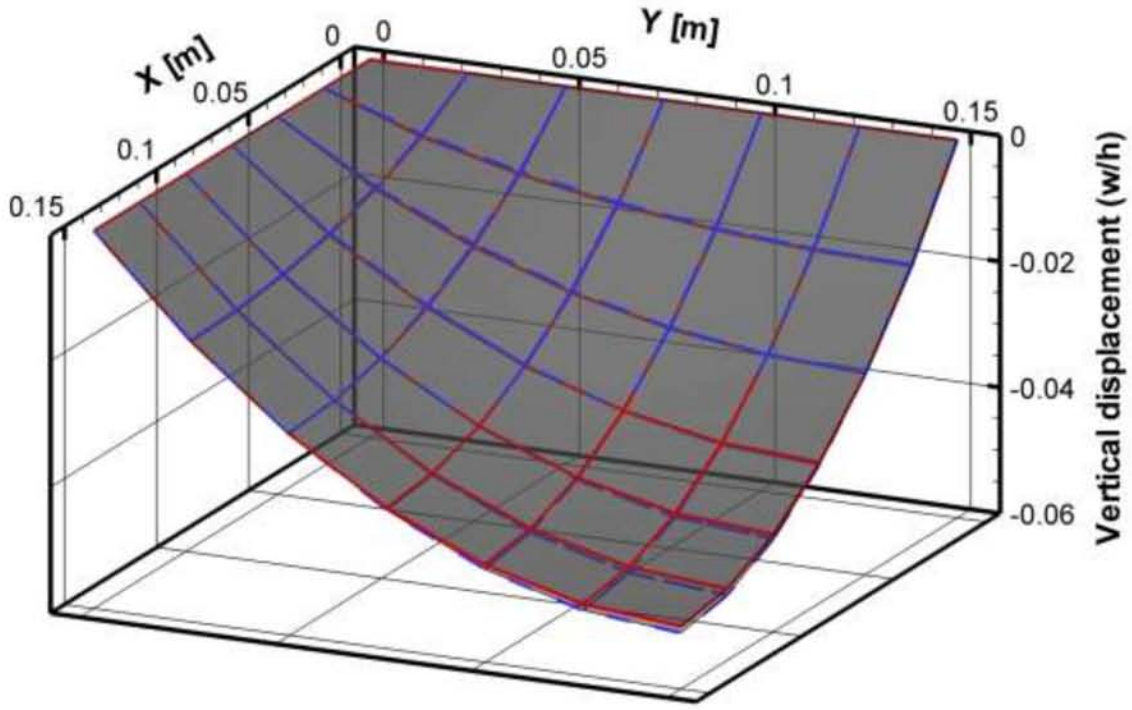

(a) 1/4 part

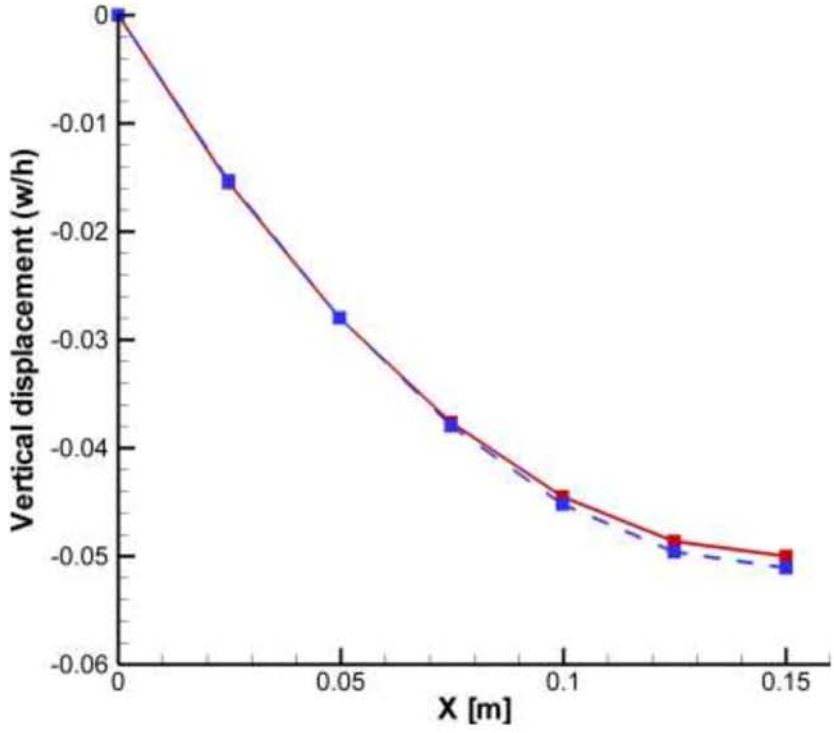

(b) y=0.15 (m)

Figure 5.6. Upper and lower membrane deformation after 5 cycles (A=0.01).

(Blue line indicate lower surface, red line indicate upper surface)

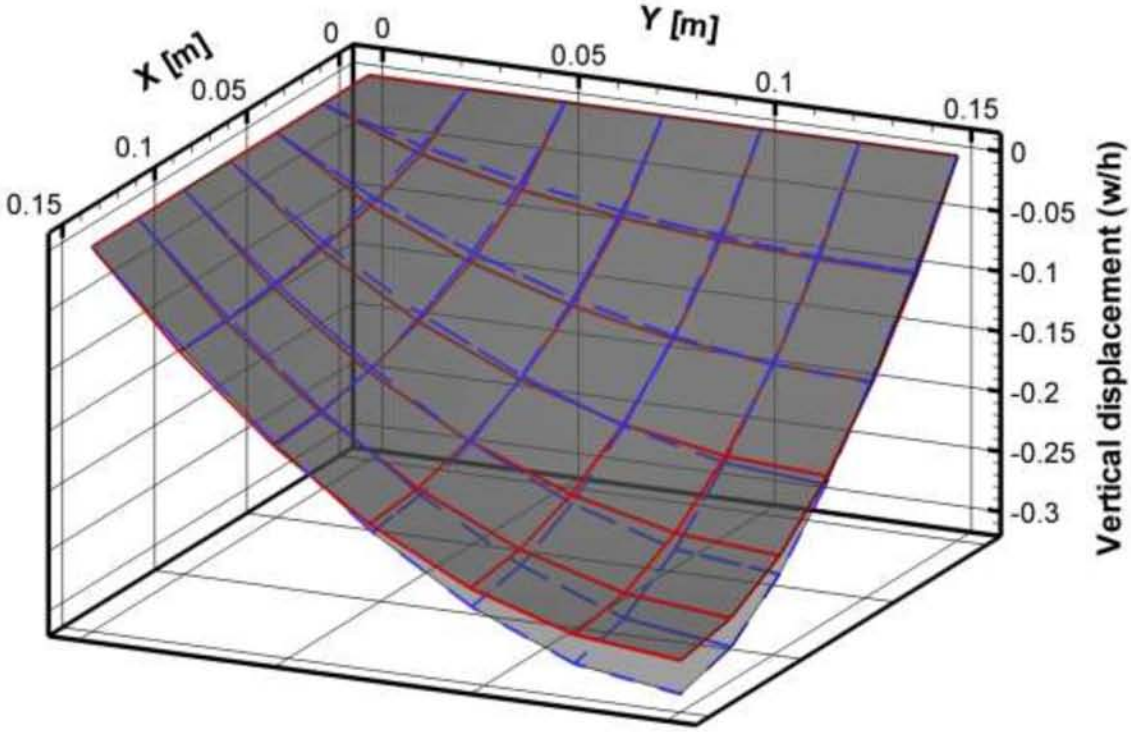

(a) 1/4 part

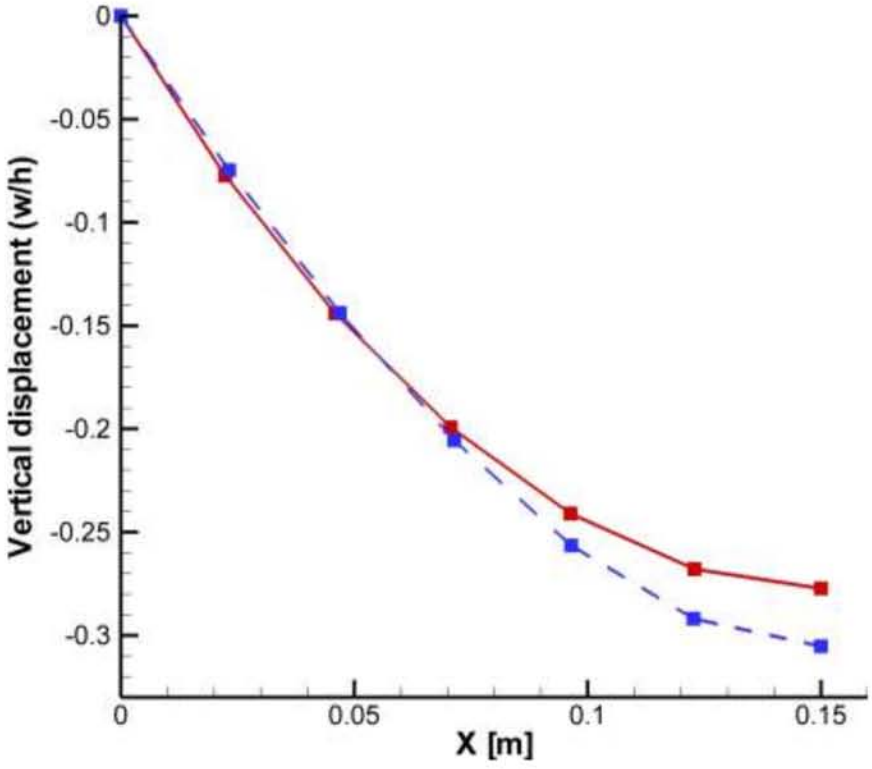

(b) y=0.15(m)

Figure 5.7. Upper and lower membrane deformation after 5 cycles (A=0.1).

(Blue line indicate lower surface, red line indicate upper surface)

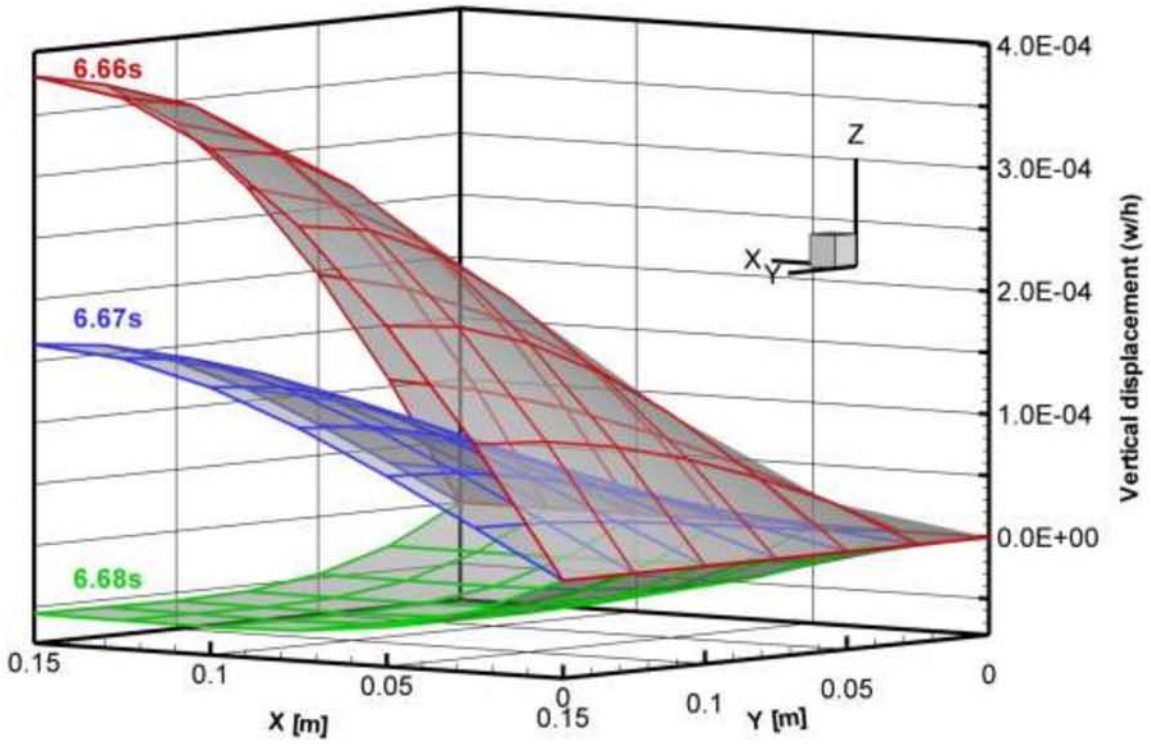

(a) Upper surface

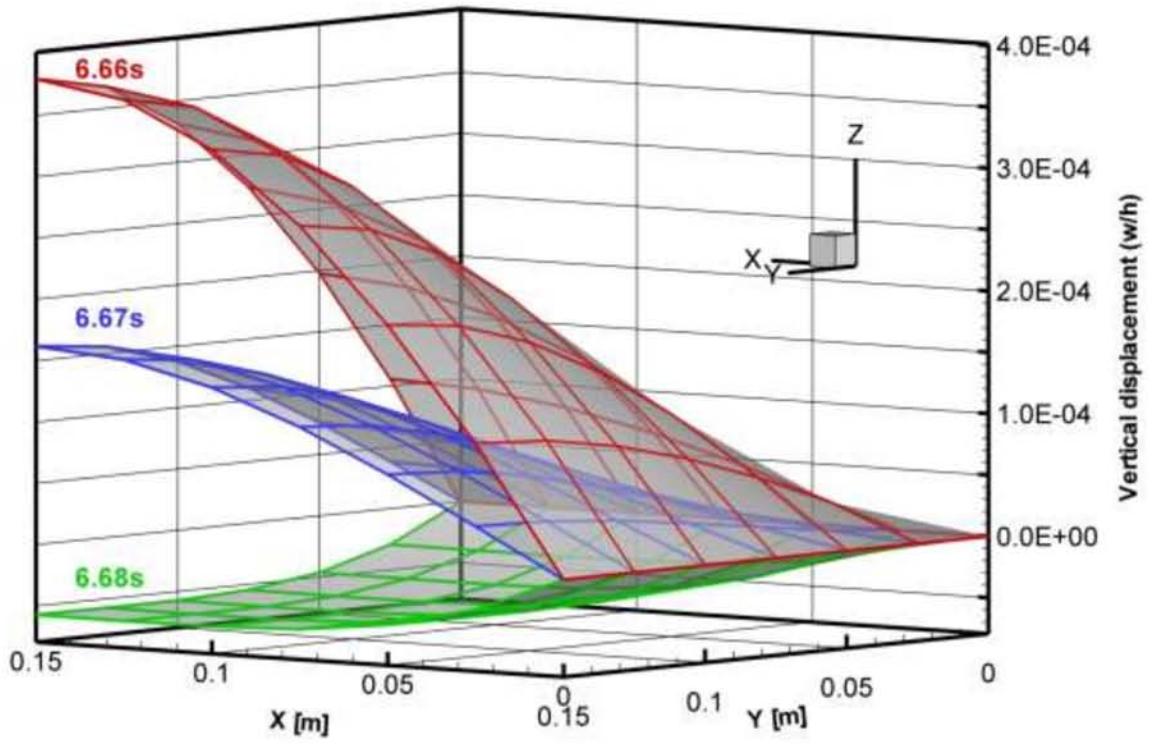

(b) Lower surface

Figure 5.8. Upper and lower surface when displacement reverse.

(A=0.001, after 4+3/4 cycle)

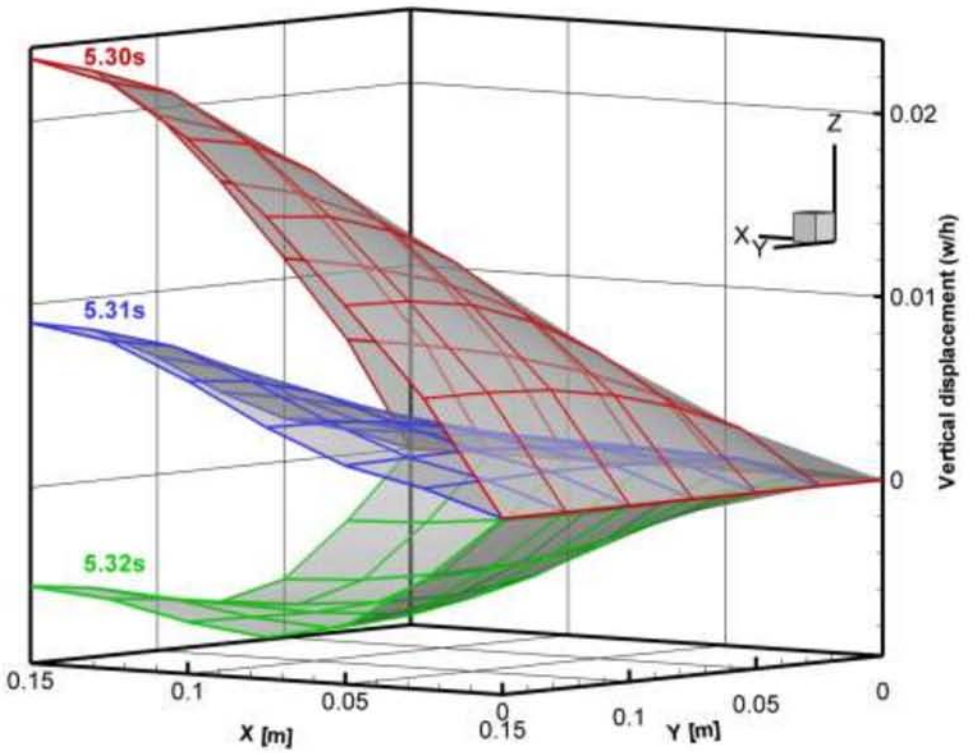

(a) 1/4 part

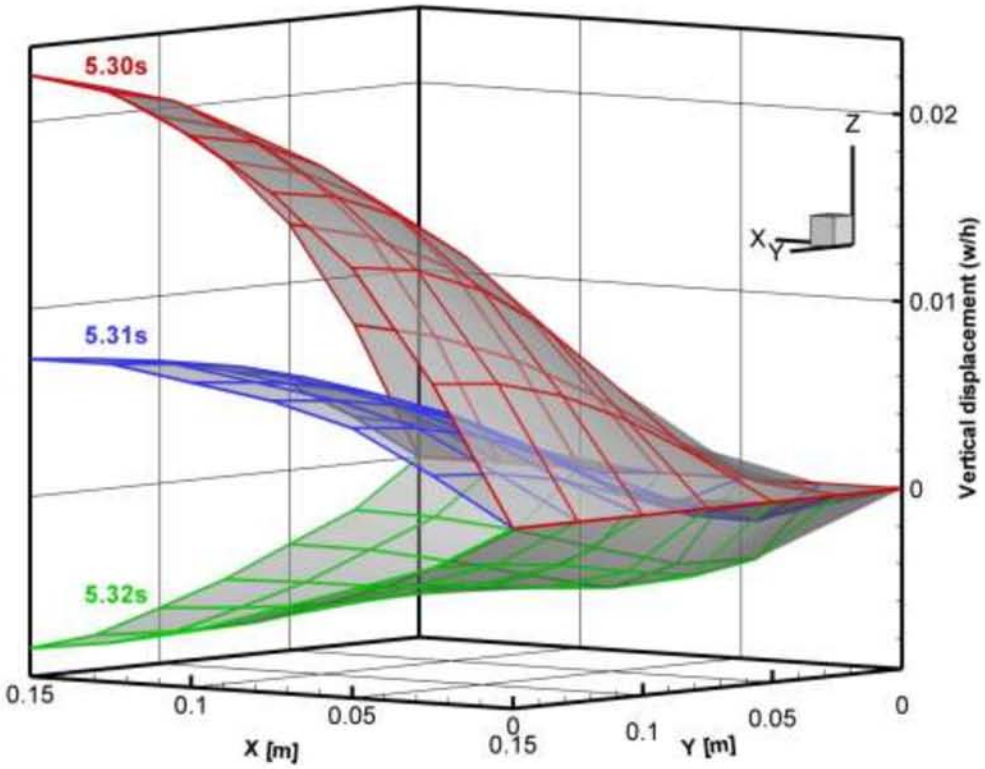

(b) y=0.15(m)

Figure 5.9. Upper and lower surface when displacement reverse.

(A=0.1, after 4+3/4 cycle)

5.2.3 Resonant frequency

The vertical displacement of the center point of the lower surface after 5 cycles is shown for different values of the vibrational acceleration in Fig. 5.10. The points connected by a line indicate the vibration frequency. The resonant frequency changes nonlinearly as the membrane deforms. The resonant frequency is defined as the frequency at which the vertical displacement is maximum after 5 cycles. Figures 5.11(a), (b), and (c) show the time-history responses of the vertical displacement at the center point of the membrane for $A = 0.001,\ 0.01,$ and $A = 0.1\ \mathrm{m/s^2},$ respectively. The red line indicates the upper surface and the green line the lower surface, while the blue dotted line indicates the vibrational acceleration. Table 5.4 shows the vibrational acceleration and phase difference for each vibration cycle.

For small deformation, the resonant frequency is 0.71 Hz. The membrane displacement diverges as shown by the time-history response in Fig. 5.11(a) because there is no damping such as liquid viscosity. In the case of linear vibrations, the phase difference between membrane displacement and vibrational acceleration is 0.5π when the model is vibrated at the resonant frequency. That is to say, the membrane displacement becomes maximum when the vibrational acceleration becomes zero. For $A = 0.001\ \mathrm{m/s^2}$ for which the resonant frequency is 0.71 Hz, the phase difference between the start and finish of vibration is $0.005\pi,$ which is 1% of 0.5π. This is so small that the phase difference can be taken as 0.5π in all cycles. Therefore, the resonant frequency does not change when vibration is confined to the small-deformation domain.

For large deformation, the resonant frequency is 0.89 Hz. The phase difference after 1 cycle is 9% larger than $0.5\pi,$ as shown in Fig. 5.11(c), and that after 3 cycles is 12% larger than 0.5π. Therefore, the phase difference between vibrational acceleration and displacement remains almost unchanged up to 3 cycles. However, after 4 cycles, the

phase difference suddenly decreases to become close to 0.5π. The variation in phase difference from 3 cycles to 5 cycles is 0.079π, which is 15% of 0.5π. This shows that the phase difference does not decrease proportionally to deformation but suddenly changes after a certain deformation has been reached. From the above, it can be seen that the resonant frequency varies widely when vibration is in the large-deformation domain, with 0.89 Hz being the average value.

When $A = 0.001$, 0.01, and $0.1\ \mathrm{m/s^2}$, the resonant frequency is 0.71, 0.72, and 0.89 Hz, respectively. When A goes from 0.001 to $0.01\ \mathrm{m/s^2}$ the percentage increase in resonant frequency is only 1.4%. However, when A goes from 0.01 to $0.1\ \mathrm{m/s^2}$, the percentage increase is 24%, confirming the strong nonlinearity. This phenomenon of a substantial increase in the resonant frequency at large deformations is called hardening nonlinearity. It does not appear in linear analyses. In addition, according to the results of the analysis in the large-deformation domain, the resonant frequency does not vary proportionally to deformation but changes suddenly after a certain value of the deformation has been reached. The deformation remains small when the acceleration is changed from $A = 0.001$ to $0.01\ \mathrm{m/s^2}$, and does not reach this value. The change in phase difference between 1 and 5 cycles is 1.0% of 0.5π when $A = 0.001\ \mathrm{m/s^2}$, 1.6% when $A = 0.01\ \mathrm{m/s^2}$, and 14% when $A = 0.1\ \mathrm{m/s^2}$. Strong nonlinearity is found when $= 0.1\ \mathrm{m/s^2}$.

Table 5.4 Vibration acceleration and phase difference of displacement （$\times\pi$(rad)）

	Vibration cycle				
	1	2	3	4	5
$A = 0.001$	0.502	0.500	0.499	0.499	0.497
$A = 0.01$	0.506	0.505	0.506	0.503	0.498
$A = 0.1$	0.546	0.565	0.556	0.523	0.477

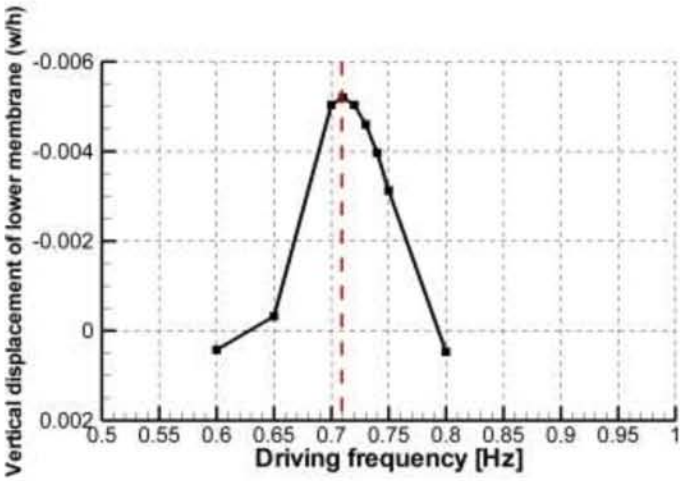

(a) $A = 0.001$

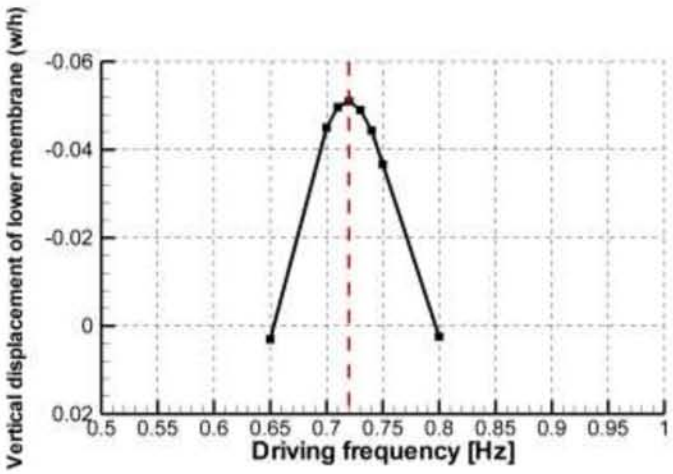

(b) $A = 0.01$

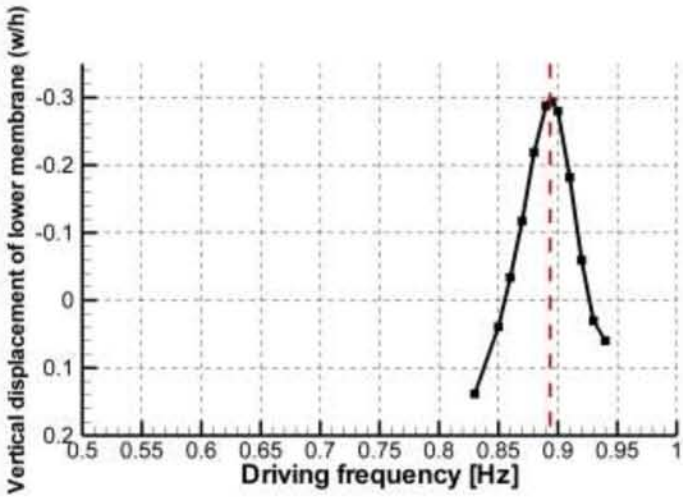

(c) $A = 0.1$

Figure 5.10. Resonant curve.

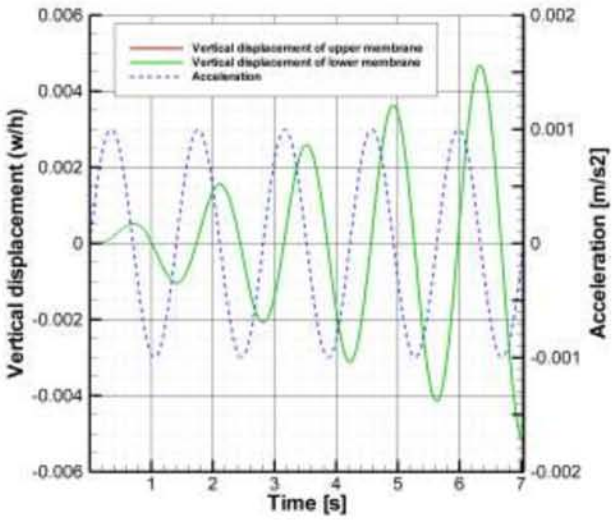

(a) $A = 0.001$

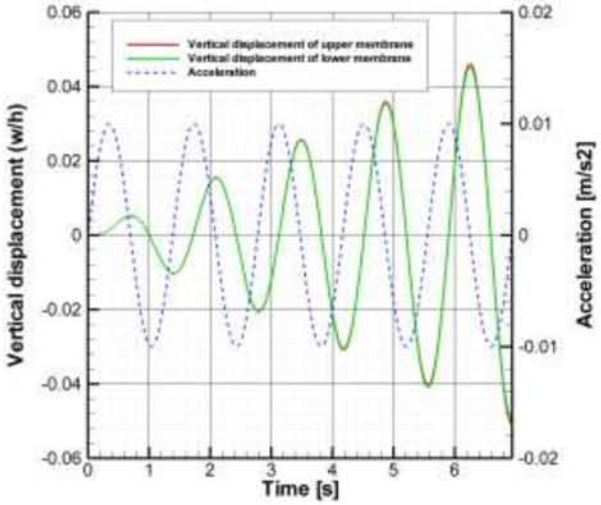

(b) $A = 0.01$

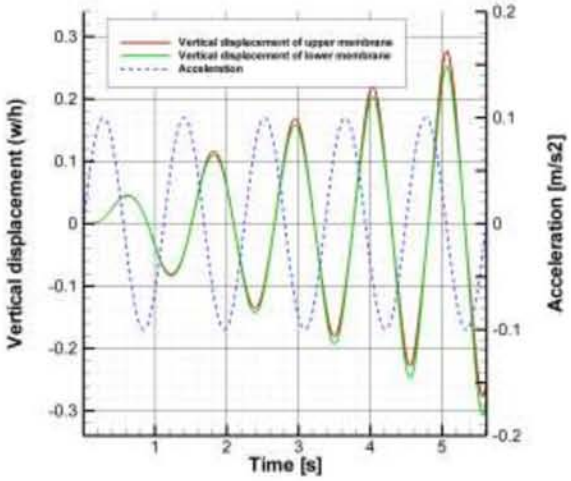

(c) $A = 0.1$

Figure 5.11. Time history response at center point of lower surface and vibration acceleration.

5.2.4 Membrane strain and stress distribution

The Green–Lagrange strain distribution of the membrane after 5 cycles is shown in Figs. 5.12 and 5.13. E_x and E_y are symmetrical because the same initial strain is applied in the x and y directions. Here E_x and E_{xy} are defined as follows:

$$E_x = \frac{\partial u}{\partial x} + \frac{1}{2}\left\{\left(\frac{\partial u}{\partial x}\right)^2 + \left(\frac{\partial v}{\partial x}\right)^2 + \left(\frac{\partial w}{\partial x}\right)^2\right\} + E_{x0}, \tag{114}$$

$$E_{xy} = \frac{\partial u}{\partial y} + \frac{\partial v}{\partial x} + \left(\frac{\partial u}{\partial x}\frac{\partial u}{\partial y} + \frac{\partial v}{\partial x}\frac{\partial v}{\partial y} + \frac{\partial w}{\partial x}\frac{\partial w}{\partial y}\right). \tag{115}$$

The Cauchy stress distribution is shown in Figs. 5.16 and 5.17. This is almost the same as the strain distribution because the rubber material is isotropic.

For small deformation, the gradient in the x direction of the vertical displacement is dominant in E_x. That is to say, the nonlinear term $\frac{1}{2}(\partial w/\partial x)^2$ in Eq. (114) is dominant. This means that the strain occurs owing to deformation in the out-of-plane direction even if there is no deformation in the x–y plane. The E_{xy} distribution is positive near the edge of the tank, where the membrane is attached, and is negative near $x = y = 0.075$ m. The negative value is due to shear deformation, which is represented by the linear term $\partial u/\partial y + \partial v/\partial x$ in Eq. (115). The positive value is due to deformation in the out-of-plane direction, which is represented by the nonlinear term $(\partial w/\partial x)(\partial w/\partial y)$. However, the variation of E_x is only 0.2% of the initial strain $E_{x0} = 0.05$ even at its maximum and E_{xy} is an order of magnitude smaller than E_x. Thus, the initial strain is dominant in phenomena in the small-deformation domain.

For large deformation, the nonlinear term $\frac{1}{2}(\partial w/\partial x)^2$ is dominant in E_x. The variation of E_x is 655% of $E_{x0} = 0.05$ at its maximum; thus, the strain more than six times the initial strain as a result of the dominance of the nonlinear term with increasing deformation in the out-of-plane direction. In the case of E_{xy}, the influence of the nonlinear term $(\partial w/\partial x)(\partial w/\partial y)$ is large. The deformation in the x–y plane after 5

cycles is shown in Fig. 5.14. The black line indicates the membrane shape before deformation and the displacement is shown at its actual size. There is negative shear deformation near $x = y = 0.075$ m in the x–y plane. However, the membrane deformation at the lower surface in the out-of-plane direction is large near $y = 0.075$, as shown in Fig. 5.15. The negative value at the lower surface resulting from shear deformation is canceled by this, and E_{xy} becomes maximum near $x = y = 0.075$ m. In the case of the upper surface, the nonlinear term prevents negative shear deformation.

The nonlinear term of the Green–Lagrange strain is of second degree, so large deformations have a strong influence. Table 5.5 shows the vertical displacement relative to its maximum value and the strain relative to its initial value (i.e., $E_x - E_{x0}$). It can be seen that when A is increased from 0.001 to 0.01 m/s^2, the vertical displacement increases by a factor of almost 9.8 and $E_x - E_{x0}$ by a factor of 95, and when A increases from 0.01 to 0.1 m/s^2, the vertical displacement increases by a factor of 6.0 and $E_x - E_{x0}$ by a factor of 36. It is found that $E_x - E_{x0}$ is approximately proportional to the square of the variation in vertical displacement. Consequently, the variation of E_x for $A = 0.01$ m/s^2 is only 20% of the initial strain $E_{x0} = 0.05$ even at its maximum; however, for $A = 0.1$ m/s^2, it is 655% of the initial strain so the influence of the initial strain is no longer small. As discussed above, the influence of the nonlinear term is strong in the large-deformation domain. The variation of the resonant frequency (see Section 5.2.3) is as follows. It increases by 24% when the acceleration changes from $A = 0.01$ to $A = 0.1$ m/s^2 because of the increase in the restoring force of the rubber. However, it increases by only 1.4% when A changes from 0.001 to 0.01 m/s^2. This is because the initial strain is dominant in the small-deformation domain. The resonant frequency changes suddenly after a certain deformation has been reached, because the strain, i.e., the restoring force, increases nonlinearly.

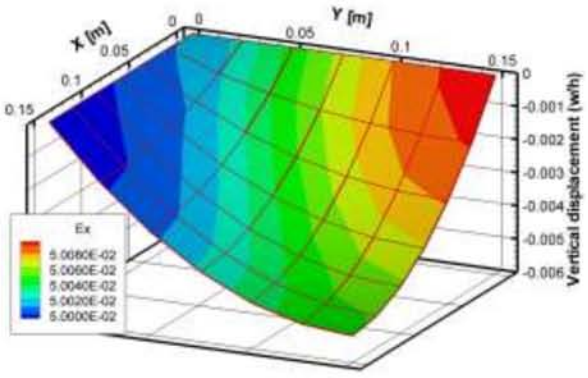

(a-1) $A = 0.001$

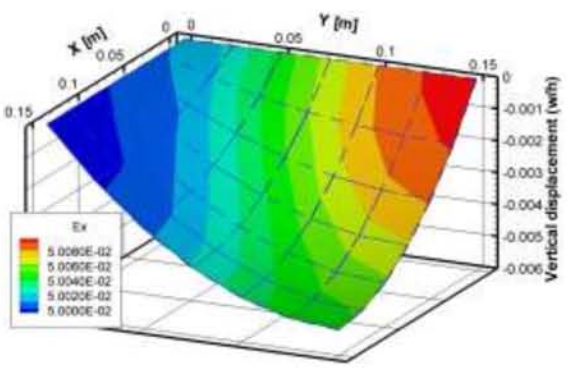

(b-1) $A = 0.001$

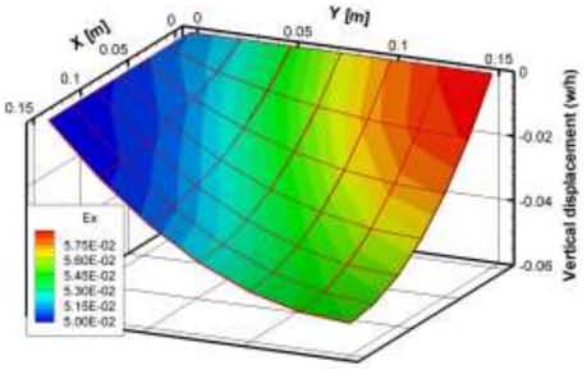

(a-2) $A = 0.01$

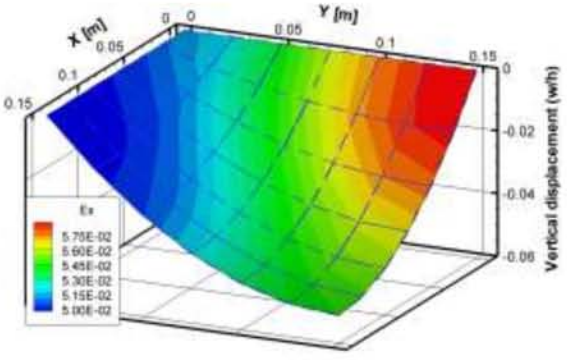

(b-2) $A = 0.01$

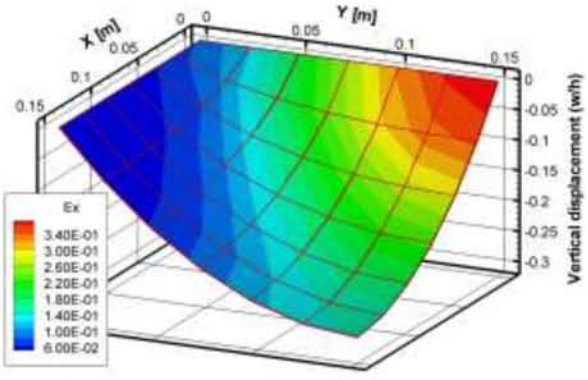

(a-3) $A = 0.1$

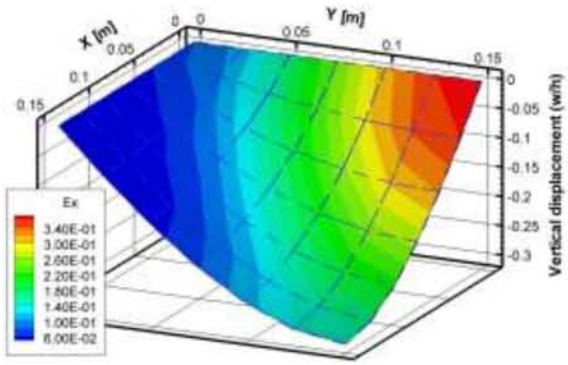

(b-3) $A = 0.1$

(a) Upper surface (b) Lower surface

Figure 5.12. Green-Lagrange strain distribution (E_x).

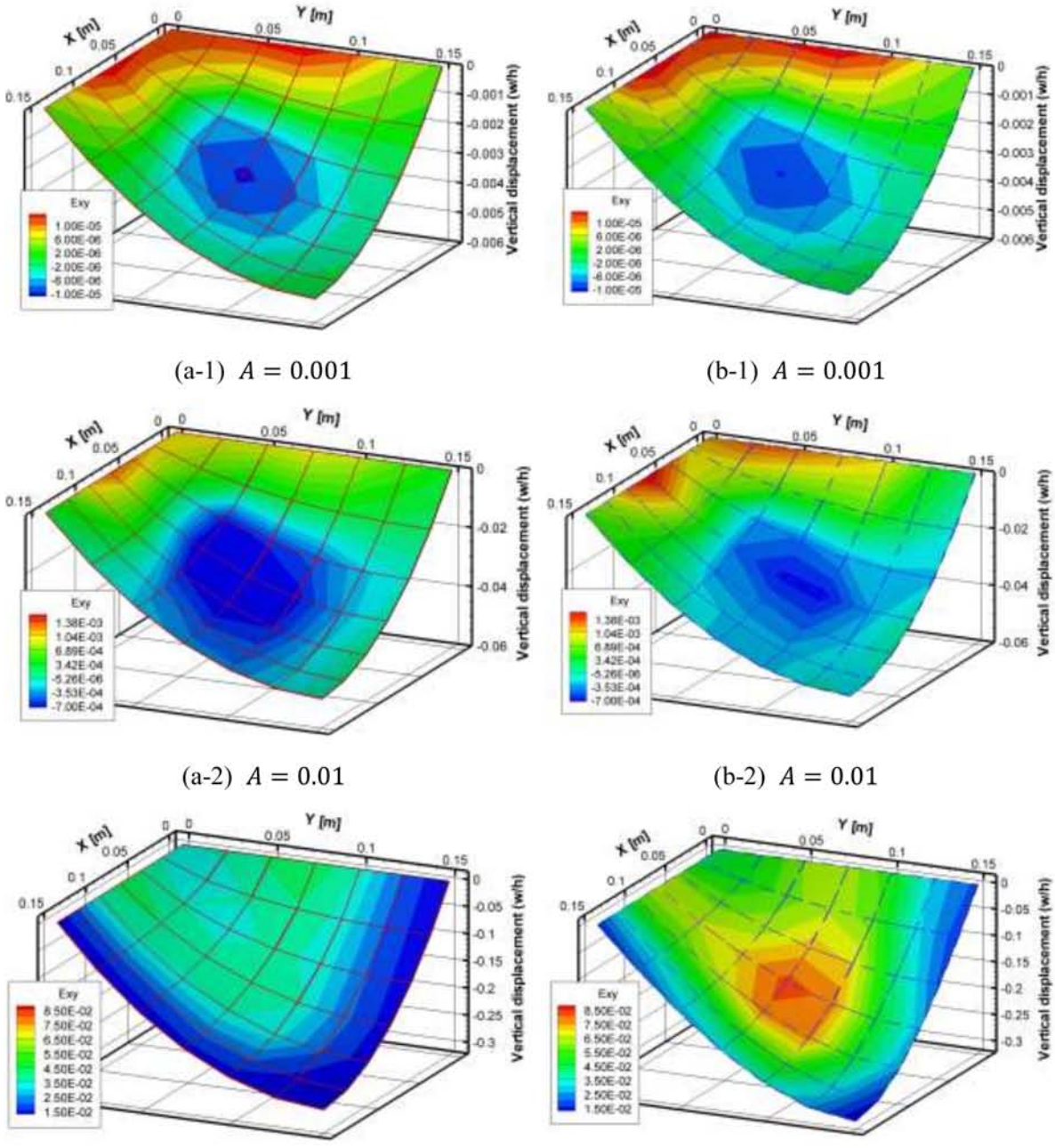

(a-1) $A = 0.001$ (b-1) $A = 0.001$

(a-2) $A = 0.01$ (b-2) $A = 0.01$

(a-3) $A = 0.1$ (b-3) $A = 0.1$

(a) Upper surface (b) Lower surface

Figure 5.13. Green-Lagrange strain distribution (E_{xy}).

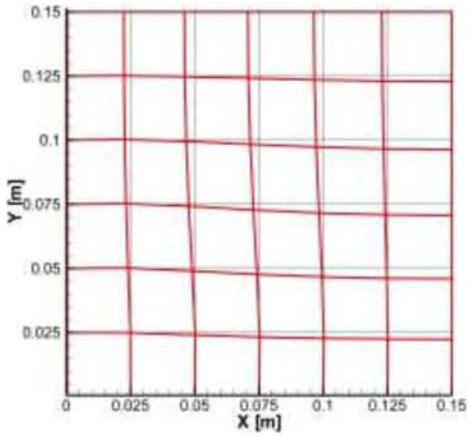

(a) Upper surface

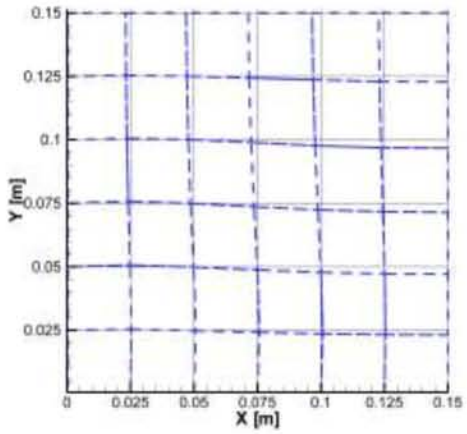

(b) Lower surface

Figure 5.14. Deformation in x-y plane after 5 cycles.

(A=0.1, black line is shape before deformation)

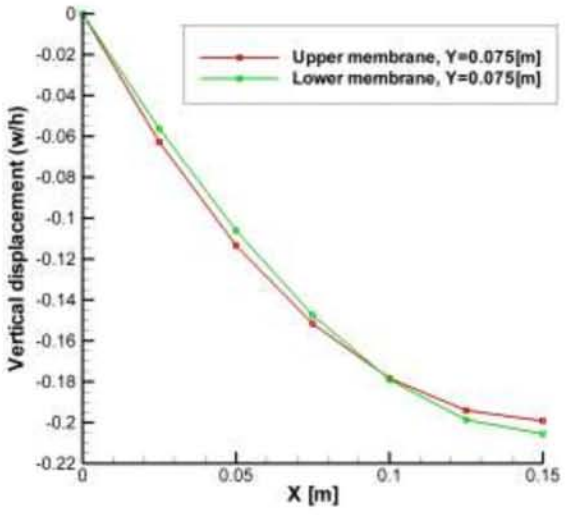

Figure 5.15. Deformation in the out-of-plane after 5 cycles (A= 0.1, y= 0.075 m).

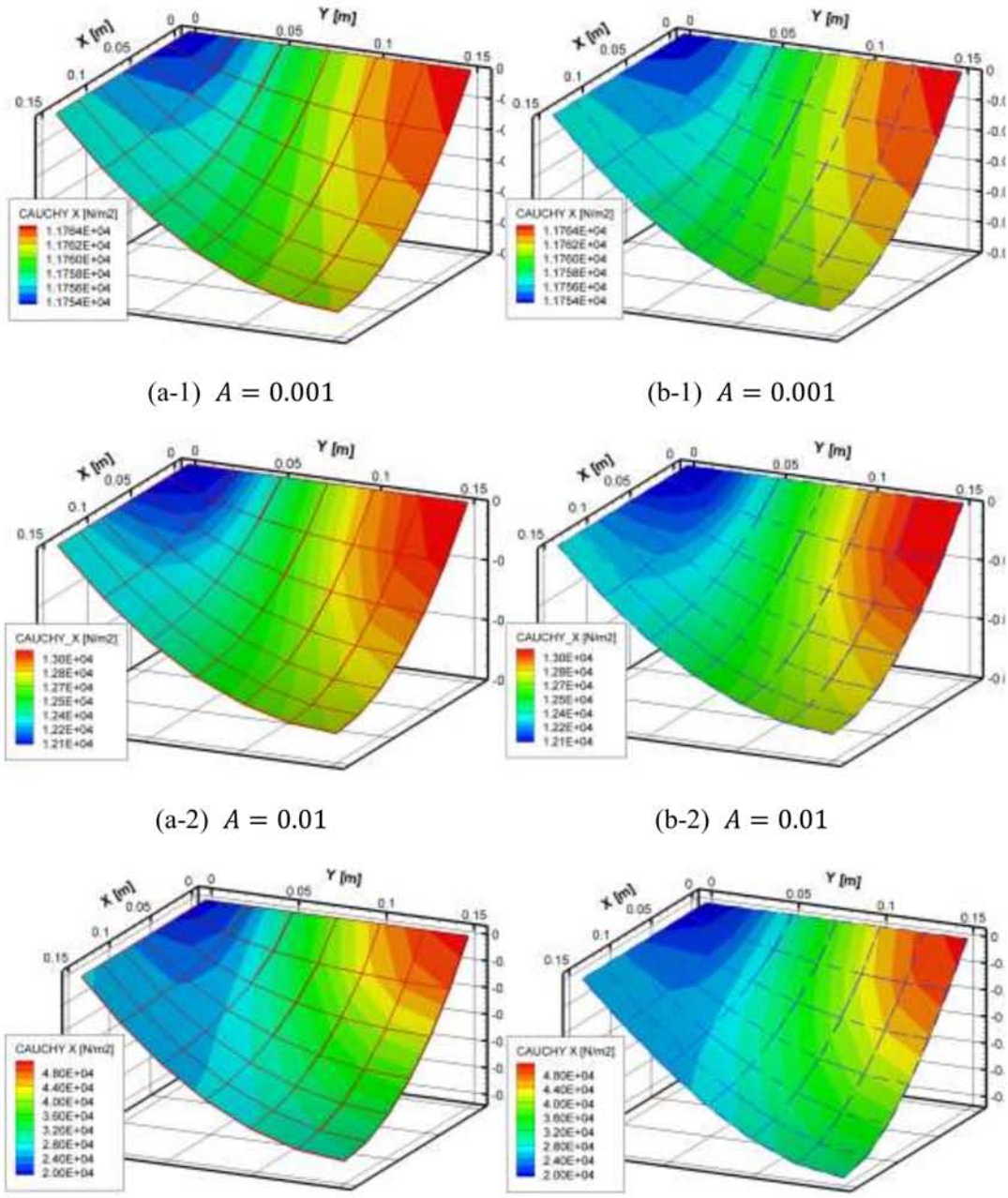

(a-1) $A = 0.001$ (b-1) $A = 0.001$

(a-2) $A = 0.01$ (b-2) $A = 0.01$

(a-3) $A = 0.1$ (b-3) $A = 0.1$

(a) Upper surface (b) Lower surface

Figure 5.16. Cauchy stress distribution (σ_x).

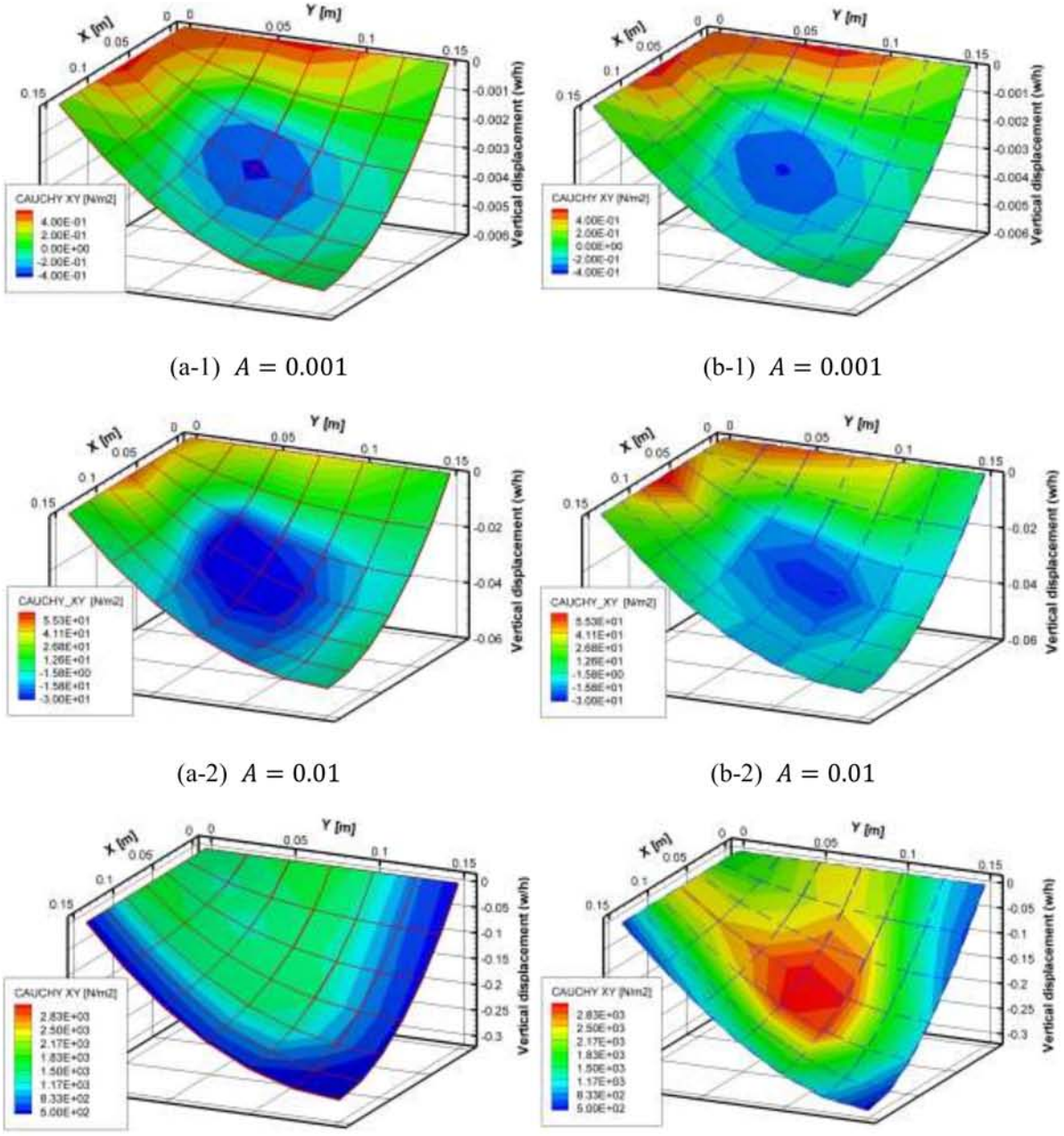

(a-1) $A = 0.001$ (b-1) $A = 0.001$

(a-2) $A = 0.01$ (b-2) $A = 0.01$

(a-3) $A = 0.1$ (b-3) $A = 0.1$

(a) Upper surface (b) Lower surface

Figure 5.17. Cauchy stress distribution (σ_{xy}).

Table 5.5 Maximum vertical displacement of lower surface and maximum value of $E_x - E_{x0}$

	Vertical displacement, w/h	$E_x - E_{x0}$
$A = 0.001$	-5.19×10^{-3}	9.49×10^{-5}
$A = 0.01$	-5.11×10^{-2}	9.05×10^{-3}
$A = 0.1$	-3.05×10^{-1}	3.27×10^{-1}

5.3 Conclusions

The difficulties arising in previous methods for the solution of models describing three-dimensional interactions of a rubberlike membrane with liquid have been described and an analysis of the large-deformation domain has been presented. In addition, the dynamical characteristics in both the small- and large-deformation domains, as well as variations in these characteristics due to deformation, have been considered. As a result, the following conclusions can be drawn.

1. In previous solution methods, a certain value was set at $E_x - E_y$ to calculate the angle that is used to calculate the principal strain. If $E_x - E_y$ was less than a certain value, then $\theta = 0$, and the principal angle become discontinuous in the structural domain. Thus, the calculation failed to converge. This problem has been solved and analysis in the large-deformation domain is allowed.

2. In the small-deformation domain, the membrane deformations and strains, as well as the stress distributions, on the upper and lower surfaces are equal. The liquid velocity and pressure distribution exhibit top–bottom asymmetry. The resonant frequency is constant in time.

3. In the large-deformation domain, the liquid velocity and pressure distribution vary owing to membrane deformation and exhibit top–bottom asymmetry. Therefore, the membrane deformation and strain and the stress also exhibit top–bottom asymmetry. The maximum vertical displacement of the membrane is 31% of the tank depth. The method

adopted here allows analysis in the large-deformation domain. It confirms that the resonant frequency varies during vibration, and there is a phase difference between the vibrational acceleration and the displacement.

4. The resonant frequency at $A = 0.1\ \mathrm{m/s^2}$ is 25% higher than that at $A = 0.001\ \mathrm{m/s^2}$, confirming the presence of hardening nonlinearity. This occurs because the membrane strain is proportional to the square of the displacement as a result of geometrical nonlinearity, and the restoring force increases suddenly. The resonant frequency changes by 1.4% when the acceleration goes from $A = 0.001$ to $A = 0.01\ \mathrm{m/s^2}$. This is because the initial strain is dominant.

CHAPTER 6

CONCLUSIONS AND RECOMMENDATION

6.1 Conclusions

The material nonlinearity of rubberlike membranes and the geometric nonlinearity of the moving boundary of a liquid at large deformation have been investigated in two-dimensional dynamic analyses. Therefore, it is shown that the material and geometrical nonlinearities of the rubberlike membrane are very important when computing the response to a low initial strain and large excitation. Moreover, applying the arbitrary Lagrangian-Eulerian finite element method to the moving boundary in the liquid region ensures agreement between the movement of the liquid and structure. However, realistic situations are too complex to be approximated by a two-dimensional model, and it is necessary to consider three-dimensional models.

We performed three-dimensional dynamical analyses of interactions between rubberlike membranes and liquid in the large-deformation domain.

First, a rectangular tank contained liquid whose upper surface was covered by a rubberlike membrane, and we examined the balance of forces in the membrane–liquid interaction in the out-of-plane direction using the equilibrium equations of the membrane. After that, we considered a rectangular tank containing liquid whose upper and lower surfaces were both covered by a rubberlike membrane, and we investigated dynamic properties including the natural frequency, liquid pressure, flow rate, strain, and the deformation of the rubberlike membrane.

We arrived at the following conclusions:

1. Although previous calculation methods failed to converge owing to the presence of large strain, we have been able to avoid this problem and allow analysis in the

large-deformation domain.

2. In the case of a rectangular tank containing liquid whose upper and lower surfaces are covered by a rubberlike membrane, in the large-deformation area, the liquid velocity and pressure distribution show a vertical asymmetry. There are significant differences in membrane deformation, strain, and stress distributions between the upper and lower surfaces.

3. Comparing the small- and large-deformation domains, a nonlinearity of hardening type is observed, with the resonance frequency being 20% higher at the maximum. This is a geometric nonlinearity, with the variation of strain in the membrane being proportional to the square of the variation of the vertical displacement as a result of a restoring force that increases rapidly at large deformations.

4. In the case of a rectangular tank containing liquid whose upper surface is covered by a membrane, nonlinearities such as left–right asymmetry of the deformation are observed in the large-deformation domain. This is also seen in the sloshing model owing to the presence of the convection term.

Motion of the liquid is obstructed near the edge of the tank where the membrane is attached. In this region, the influence of the membrane dominates over the liquid pressure and liquid deformation. Elsewhere, the effects of the liquid are dominant.

5. From a comparison of the liquid pressure and the membrane curvature, it was confirmed that the liquid pressure was supported by the curvature. In addition, the balance of forces in the structure and at the liquid boundary in the out-of-plane direction were shown to be satisfied from the equilibrium equation.

The present study has successfully provided a three-dimensional dynamical analysis of the interaction between a rubber membrane and a liquid in the large-deformation domain, where the characteristics of the nonlinearity are completely

different from those at small deformation. Moreover, the equilibrium of the forces involved in the structure–liquid interaction is satisfied, indicating the validity of the analysis.

6.2 Recommendation

Several potential future works and recommendations for other researchers as extensions of this study are listed below:

1. As mention in the introduction, the dimension of tank show strong effects to the behaviors of sloshing nonlinear. There is no a comparison with purely nonlinear sloshing nonlinear results, e.g., in [5,6], as a limit case; this is especially strange because the depth-to-breadth ratio is 0.375 which is close to the experimental and theoretical cases in [5,6]. We recommend the researchers to investigate the effect of tank depth for a comparison with purely nonlinear sloshing nonlinear results.

2. In a sloshing model using a square tank, the natural frequencies of the (1,0) and (0,1) sloshing modes are identical. In such a case, it is known that (1,0) and (0,1) modes may appear simultaneously due to the internal resonance even when the tank is excited in the x direction. Actually, this work did not concern and observed about the internal resonance in the square tank. However, the internal resonance is possible to appear in the sloshing of a square tank when the natural frequencies satisfy the internal resonance conditions. Then, we add the comment about the possibility of the appearance of the internal resonance and refer to the literatures.

3. This work describes a method for calculating the interaction between flow phenomena and elastic membranes. The model makes use of a finite-element formulation for the structure in combination with an ALE approach for the liquid. This work lacks a grid refinement study, which helps to separate the numerical errors from the physical

contents of the paper. Since the physics of the rubberlike membranes is complex, physical validation is necessary which should not be hampered by a large amount of numerical noise. The researcher should do the grid refinement to improve the numerical accuracy.

4. No experiments or comparisons with existing experiments are done that makes the output not validated. The researchers should do experiments or compare with existing experiments.

5. The effect of liquid viscosity is interesting. It was found that viscosity decreases the oscillation frequencies in comparison to the coupled hydroelastic frequencies of the frictionless liquid and that a new phenomenon appears exhibiting for certain small liquid heights h/a only a periodic motion [58-60]. In that treatment, adhesive conditions at the container bottom were satisfied, while at the small sidewall area only the normal velocity condition has been observed. This seems to be justified for shallow containers. This analytical treatment yields approximate complex frequencies, of which the real parts describe the damping decay, while the imaginary parts represent the oscillation frequencies.

APPENDIX A

Green–Lagrange strain variation equation

From Eqs. (9)–(11), the Green–Lagrange strain in a Cartesian coordinate system $(x,\ y,\ z)$ is given by

$$\delta E_x = \frac{\partial \delta u}{\partial x} + \left(\frac{\partial u}{\partial x}\frac{\partial \delta u}{\partial x} + \frac{\partial v}{\partial x}\frac{\partial \delta v}{\partial x} + \frac{\partial w}{\partial x}\frac{\partial \delta w}{\partial x}\right) \tag{A1}$$

$$= \frac{\partial}{\partial x}\left[1 + \frac{\partial u}{\partial x} \quad \frac{\partial v}{\partial x} \quad \frac{\partial w}{\partial x}\right]\begin{Bmatrix}\delta u\\ \delta v\\ \delta w\end{Bmatrix},$$

$$\delta E_y = \frac{\partial \delta v}{\partial y} + \left(\frac{\partial u}{\partial y}\frac{\partial \delta u}{\partial y} + \frac{\partial v}{\partial y}\frac{\partial \delta v}{\partial y} + \frac{\partial w}{\partial y}\frac{\partial \delta w}{\partial y}\right) \tag{A2}$$

$$= \frac{\partial}{\partial y}\left[\frac{\partial u}{\partial y} \quad 1 + \frac{\partial v}{\partial y} \quad \frac{\partial w}{\partial y}\right]\begin{Bmatrix}\delta u\\ \delta v\\ \delta w\end{Bmatrix},$$

$$\delta E_{xy} = \frac{\partial \delta u}{\partial y} + \frac{\partial \delta v}{\partial x}\left(\begin{array}{c}\dfrac{\partial \delta u}{\partial x}\dfrac{\partial u}{\partial y} + \dfrac{\partial u}{\partial x}\dfrac{\partial \delta u}{\partial y} + \dfrac{\partial \delta v}{\partial x}\dfrac{\partial v}{\partial y}\\ + \dfrac{\partial v}{\partial x}\dfrac{\partial \delta v}{\partial y} + \dfrac{\partial \delta w}{\partial x}\dfrac{\partial w}{\partial y} + \dfrac{\partial w}{\partial x}\dfrac{\partial \delta w}{\partial y}\end{array}\right) \tag{A3}$$

$$= \frac{\partial}{\partial x}\left[\frac{\partial u}{\partial y} \quad 1 + \frac{\partial v}{\partial y} \quad \frac{\partial w}{\partial y}\right]\begin{Bmatrix}\delta u\\ \delta v\\ \delta w\end{Bmatrix} + \frac{\partial}{\partial y}\left[1 + \frac{\partial u}{\partial x} \quad \frac{\partial v}{\partial x} \quad \frac{\partial w}{\partial x}\right]\begin{Bmatrix}\delta u\\ \delta v\\ \delta w\end{Bmatrix}.$$

When discretized using a shape function as described in Section 2.8.1, it can be written as

$$\delta\mathbf{E} = \mathbf{B}\delta\mathbf{U}, \tag{A4}$$

where

$$\delta\mathbf{E} = \begin{bmatrix}\delta E_x & \frac{1}{2}\delta E_{xy}\\ \frac{1}{2}\delta E_{xy} & \delta E_y\end{bmatrix}, \tag{A5}$$

$$\mathbf{B} = \begin{bmatrix} \left(1+\frac{\partial u}{\partial x} \quad \frac{\partial v}{\partial x} \quad \frac{\partial w}{\partial x}\right)\mathbf{H}_{,x} & \frac{1}{2}\begin{Bmatrix} \left(1+\frac{\partial u}{\partial x} \quad \frac{\partial v}{\partial x} \quad \frac{\partial w}{\partial x}\right)\mathbf{H}_{,y} \\ +\left(\frac{\partial u}{\partial y} \quad 1+\frac{\partial v}{\partial y} \quad \frac{\partial w}{\partial y}\right)\mathbf{H}_{,x} \end{Bmatrix} \\ \text{sym} & \left(\frac{\partial u}{\partial y} \quad 1+\frac{\partial v}{\partial y} \quad \frac{\partial w}{\partial y}\right)\mathbf{H}_{,y} \end{bmatrix} \tag{A6}$$

Here $(\quad)_{,x}$ and $(\quad)_{,y}$ denote partial derivatives with respect to the Cartesian coordinates x and y. Furthermore, the Green–Lagrange strain tensor, $\delta\bar{\mathbf{E}}$ in the principal direction can be obtained as in Section 2.4.2 using the following equations.

$$\delta\bar{\mathbf{E}} = \bar{\mathbf{B}}\delta\mathbf{U}, \tag{A7}$$

$$\bar{\mathbf{B}} = \mathbf{T}\mathbf{B}\mathbf{T}^{\mathrm{T}} \tag{A8}$$

.

APPENDIX B

Linear theory of sloshing model

The governing equations of the interaction problem are Eqs. (29) - (32). In contrast, in the liquid sloshing analysis, because there is no structure term, the governing equations are as follows:

$$\nabla \cdot \nabla \phi = 0 \qquad \text{in } \Omega_f, \tag{B1}$$

$$\pi_f \mathbf{n}_f = 0 \qquad \text{on } T_f, \tag{B2}$$

$$\nabla \phi \cdot \mathbf{n}_f = 0 \qquad \text{on } T_r, \tag{B3}$$

$$\pi_f \equiv \frac{1}{2}\rho_f \nabla \phi \cdot \nabla \phi + \rho_f \phi' + \rho_f \mathbf{a} \cdot \mathbf{y}_f \tag{B4}$$

where Γ_f and Γ_r are the boundaries of the free surface and the rigid container, respectively. For small excitations, the free surface is replaced by the static condition $z = \eta$ and quadratic terms are neglected. Equation (B2) then becomes

$$\rho_f \dot{\phi} + \rho_f g \eta = 0, \tag{B5}$$

The vertical velocity w of the free surface is

$$w = \frac{D\eta}{Dt} = \frac{\partial \eta}{\partial t}. \tag{B6}$$

Equations (B.5) and (B.6) give

$$\frac{\partial^2 \phi}{\partial t} + g\frac{\partial \phi}{\partial z} = 0 \quad (z = 0). \tag{B7}$$

The continuity equation (B.1) is solved under the boundary conditions (B.3) and (B.7). For the rectangular tank used in this study, the natural frequency ω_0 is obtained as

$$\omega_0 = \sqrt{gk \tanh(kH)}, \tag{B8}$$

with

$$k = \frac{2\pi m}{l}. \tag{B9}$$

H and l are the depth and width of the tank and m is the vibration mode number. The natural frequencies from the first to the third mode are shown in Table B1.

Table B1. The natural frequency of sloshing model (small deformation)

Mode	f_0 (Hz)
1	0.90
2	1.38
3	1.71

REFERENCES

[1] R. A. Ibrahim, Liquid Sloshing Dynamics, Cambridge University Press, Cambridge, 2005.

[2] J. P. B. Vreeburg, A. E. P. Veldman, Transient and sloshing motions in an unsupported container, in: R. Monti (Ed.), Physics of Fluids in Microgravity, Taylor and Francis Publishers, 2002, pp.293-321.

[3] J. P. B. Vreeburg, Measured states of Sloshsat FLEVO, in: Proceedings of the 56th International Astronautical Congress, Fukuoka, 2005, Paper IAF-05-C1.2.09.

[4] A. E. P. Veldman, J. Gerrits, R. Luppes, J. A. Helder, J. P. B. Vreeburg, The numerical simulation of liquid sloshing on board spacecraft, J. Comput. Phys. 224 (2007) 82–99.

[5] O. M. Faltinsen, O. F. Rognebakke, I. A. Lukovsky, A. N. Timokha, Multidimensional modal analysis of nonlinear sloshing in a rectangular tank with finite water depth, J. Fluid Mech. 407 (2000) 201-234.

[6] O. M. Faltinsen, A. N. Timokha, Adaptive multimodal approach to nonlinear sloshing in a rectangular tank, J. Fluid Mech. 432 (2001) 167-200.

[7] Y. W. Kim, Y. S. Lee, Coupled vibration analysis of liquid-filled rigid cylindrical storage tank with an annular plate cover, J. Sound Vib. 279 (2005) 217-235.

[8] K. C. Biswal, S. K. Bhattacharyya, P. K. Sinha, Dynamic response analysis of a liquid-filled cylindrical tank with annular baffle, J. Sound Vib. 274 (2004), 13-37.

[9] K. N. Karagiozis, M. Amabili, M. P. Padoussis, A. K. Misr, Nonlinear vibrations of fluid-filled clamped circular cylindrical shells, J. Fluid Struct. 21(2005) 579-595.

[10] K. H. Jeong, Hydroelastic vibration of two annular plates coupled with a bounded compressible fluid, J. Fluid Struct. 22 (2006) 1079-1096.

[11] M. S. Celebi, H. Akyıldız, Nonlinear modeling of liquid sloshing in a moving rectangular tank, Ocean Eng. 29 (2001) 1527-1553.

[12] H. Kawakami, Vibration analysis of fluid-filled rubberlike membrane structures, in: Proceeding of 38th AIAA/ASME/ASCE/AHS/ASC Structures, Structural Dynamics, and Materials Conference, Kissimmee, Florida, April 1997, pp.411–420.

[13] H. F. Bauer, Coupled frequencies of a liquid in a circular cylindrical container with elastic liquid surface cover, J. Sound Vib. 180 (1995) 689-704.

[14] H. F. Bauer, M. Chiba, Hydroelastic viscous oscillations in a circular cylindrical container with an elastic cover, J. Fluids Struct. 14 (2000) 917-936.

[15] H. F. Bauer, W. Eidel, Frictionless liquid sloshing in circular cylindrical container configurations, Aerosp. Sci. Technol. 3 (1999) 301-311.

[16] H. F. Bauer, K. Komatsu, Coupled frequencies of a frictionless liquid in a circular cylindrical tank with an elastic partial surface cover, J. Sound Vib. 230 (2000) 1147-1163.

[17] H. F. Bauer, M. Chiba, Axisymmetric oscillation of a viscous liquid covered by an elastic structure, J. Sound Vib. 281 (2005) 835-847.

[18] H. F. Bauer, M. Chiba, Viscous oscillations in a circular cylindrical tank with elastic surface cover, J. Sound Vib. 304 (2007) 1-17.

[19] R. I. Bohun, V. A. Trotsenko, Free oscillations of a fluid in a cylindrical container with arbitrary axisymmetric bottom and elastic elements on the free surface of the fluid, Nonlinear Oscil. 13 (2011) 493-514.

[20] I. Gavrilyuk, M. Hermann, A. Timokha, V. Trotsenko, Modelling of the eigenfield of a prestressed hyperelasticmembrane encapsulating a liquid, Comput. Methods Appl. Math. 6(4) (2006) 367-385.

[21] H. F. Bauer, Hydroelastic vibrations in a rectangular container, Int. J. Solids Struct. 17 (1981) 639-652.

[22] H. F. Bauer, W. Eidel, Non-linear hydroelastic vibrations in rectangular containers, J. Sound Vib. 125 (1988) 93-114.

[23] H. F. Bauer, W. Eidel, Hydroelastic vibrations in a rectangular container filled with frictionless liquid and partly elastically covered free surface, J. Fluids Struct. 19 (2004) 209-220.

[24] T. Ikeda, N. Nakagawa, Nonlinear vibrations of a structure caused by water sloshing in a rectangular tank, J. Sound Vib. 201 (1997) 23-41.

[25] T. Ikeda, T. Hirayama, N. Nakagawa, Nonlinear vibrations of a structure caused by water sloshing in a cylindrical tank, JSME Int. J. Ser. C, Dyn. Control Robot. Des. Manuf. 41 (1998) 639-651.

[26] T. Ikeda, Nonlinear parametric vibrations of an elastic structure with a rectangular liquid tank, Nonlinear Dyn. 33 (2003) 43-70.

[27] H. Akyildız, N. E. Ünal, Sloshing in a three-dimensional rectangular tank: numerical simulation and experimental validation, Ocean Eng. 33 (2006) 2135-2149.

[28] J. W. Miles, Internally resonant surface waves in a circular cylinder, J. Fluid Mech. 149 (1984) 1-14.

[29] D. D. Waterhouse, Resonant sloshing near a critical depth, J. Fluid Mech. 281 (1994) 313-318.

[30] O. M. Faltinsen, O. F. Rognebakke, A. N. Timokha, Resonant three dimensional nonlinear sloshing in a square-base basin, J. Fluid Mech. 487 (2003) 1-42.

[31] M. Chiba, Axisymmetric free hydroelastic vibration of a flexural bottom plate in a cylindrical tank supported on an elastic foundation, J. Sound Vib. 169 (1994) 387-394.

[32] H. F. Bauer, M. Chiba, Viscous hydroelastic vibrations in a cylindrical container with an elastic bottom, J. Sound Vib. 247(1) (2001) 33-57.

[33] M. Chiba, H. Watanabe, H. F. Bauer, Hydroelastic coupled vibrations in a cylindrical container with a membrane bottom, containing liquid with surface tension, J. Sound Vib. 251 (4) (2002) 717-740.

[34] Y. K. Cheung, D. Zhou, Coupled vibratory characteristics of a rectangular container bottom plate, J. Fluid Struct. 14 (2000) 339-357.

[35] F. Daneshmand, E. Ghavanloo, Coupled free vibration analysis of a fluid-filled rectangular container with a sagged bottom membrane, J. Fluid Struct. 26 (2010) 236-252.

[36] H. Zhang, P. Wu, W. Liu, The analysis of second-order sloshing resonance in a 3-D tank, J. Hydrodynam. 26(2) (2014) 309-315.

[37] S. M. Hasheminejad, M. Tafani, Coupled hydroelastic vibrations of an elliptical cylindrical tank with an elastic bottom, J. Hydrodynam. 26(2) (2014) 264-276.

[38] M. Souli, A. Ouahsine, L. Lewin, ALE formulation for fluid–structure interaction problems, Comput. Methods Appl. Mech. Eng. 190 (2000) 659-675.

[39] C. W. Hirt, A. A. Amsden, J.L. Cook, An arbitrary Lagrangian–Eulerian method for all flow speeds, J. Comput. Phys. 14 (1974) 227-253.

[40] J. Donea, S. Jiuliani, J. P. Halleux, An arbitrary Lagrangian–Eulerian finite element method for transient dynamic fluid–structure interactions, Comput. Methods Appl. Mech. Eng. 33 (1982) 689-723.

[41] W. K. Liu, J. Gvildys, Fluid structure interaction of thanks with an eccentric core barrel, Comput. Methods Appl. Mech. Eng. 58 (1985) 51-77.

[42] C. Nitikipaiboon, K. J. Bathe, An arbitrary Lagrangian–Eulerian velocity potential formulation for fluid–structure interaction, Comput. Struct. 47 (1993) 871-891.

[43] P. LeTallec, J. Mouro, Fluid structure interaction with large structural displacements, Comput. Methods Appl. Mech. Eng. 190 (2001) 3039-3067.

[44] D. J. Benson, An efficient, accurate, simple ale method for nonlinear finite element programs, Comput. Methods Appl. Mech. Eng. 72 (1989) 305-350.

[45] A. M. Winslow, Equipotential zoning of the interior of a three-dimensional mesh, Lawrence Radiation Laboratory, UCRL-7312, 1992.

[46] A. Soulaimani, Y. Saad, An arbitrary Lagrangian–Eulerian finite element method for solving three-dimensional free surface flows, Comput. Methods Appl. Mech. Eng. 162 (1998) 79-106.

[47] J. R. Cho, S. Y. Lee, Dynamic analysis of baffled fuel-storage tanks using the ALE finite element method, Int. J. Numer. Methods Fluids 41 (2003) 185-208.

[48] A. Ali, M. Hosseini, B. B. Sahari, A review of constitutive models for rubber-like materials, Am. J. Eng. Appl. Sci. 3 (2010) 232-239.

[49] F. Cirak, R. Radovitzky, A Lagrangian–Eulerian shell–fluid coupling algorithm based on level sets, Comput. Struct. 83 (2005) 491-498.

[50] R. W. Ogden, Elastic deformation of rubberlike solids, in: H.G. Hopkins, M.J. Sewell (Eds.), Mechanics of Solids, Pergamon Press, Oxford, 1981, pp. 499-537.

[51] S. Timoshenko, J. N. Goodier, Theory of elasticity, McGraw-Hill (2nd Ed.), The Maple Press Company, York, Pennsylvania, 1951.

[52] E. Kock, L. Olson, Fluid-structure interaction analysis by finite element method-a variational approach, Int. J. Numer. Meth. Eng. 31 (1991) 463-491.

[53] G. X. Wu, Q. W. Ma, R. Eatock Taylor, Numerical simulation of sloshing waves in a 3D tank based on a finite element method, Appl. Ocean Res. 20 (1998) 337–355.

[54] T. Ikeda, R. A. Ibrahim, Y. Harata, T. Kuriyama, Nonlinear liquid sloshing in a square tank subjected to obliquely horizontal excitation, J. Fluid Mech. 700 (2012) 304-328.

[55] T. Ikeda, Y. Harata, R. Ibrahim, Nonlinear liquid sloshing in square tanks subjected to horizontal random excitation, Nonlinear Dynam. 72 (2013) 1-15.

[56] T. Ikeda, Y. Harata, T. Osasa, Internal resonance of nonlinear sloshing in rectangular liquid tanks subjected to obliquely horizontal excitation, J. Sound Vib. 361 (2016) 210-225.

[57] H. Kawakami, N. Watanabe, Vibration analysis of fluid-filled rubberlike membrane structure (second report): Proceeding of 39th AIAA/ASME/ASCE/AHS/ASC Structures, Structural Dynamics, and Materials Conference Long Beach, California, April 1998, pp. 2012-2020.

[58] H.F. Bauer, W. Eidel, Axisymmetric viscous liquid oscillations in a cylindrical container, Forschung im Ingenieurwesen 63 (1997) 189-201.

[59] H.F. Bauer, W. Eidel, Oscillations of a viscous liquid in a cylindrical container, Aerosp. Sci. Technol. 8 (1997) 519-532.

[60] H.F. Bauer, W. Eidel, Free oscillations and response of a viscous liquid in a rigid circular cylindrical tank Aerosp. Sci. Technol. 3 (1999) 495-512.

PUBLICATION LIST

Refereed Journal Paper

1. W. Parasil, and N.Watanabe, "Nonlinear dynamical analysis of interaction between a three-dimensional rubberlike membrane and liquid in a rectangular tank", *International Journal of Non-Linear Mechanics*, (2016) Vol. 87, p. 64-84.
2. W. Parasil, and N.Watanabe, "Nonlinear dynamic analysis of the interaction between a two-dimensional rubberlike membrane and a liquid in a rectangular tank", *Aerospace Science and Technology*, (2016) Vol.56, p. 212-222.

International Conference Proceedings

1. W. Parasil, and N. Watanabe, "Three dimensional nonlinear analysis of fluid-membrane interaction in the rectangular tank", the 23rd International Congress on Sound and Vibration (ICSV23), 10 –14 Jul 2016, Athens, Greece.
2. W. Parasil, and N. Watanabe, "The effects of tank depth on the nonlinear behaviors of fluid-membrane interaction in rectangular tank", the 22nd International Congress on Sound and Vibration (ICSV22), 12–16 Jul 2015, Florence, Italy.

ACKNOWLEDGEMENTS

Completion of this doctoral dissertation was possible with the support of several people. I would like to express my sincere gratitude to all of them. First of all, I would like to sincerely thank my supervisor Professor Naoyuki Watanabe for his valuable guidance, scholarly inputs and consistent encouragement that I received throughout the research work. Besides my advisor, I would like to thank the rest of my thesis committee: Prof. Koichi Kitazono, Prof. Hironori Sahara, and Assoc. Prof. Toshio Tagawa, for their insightful comments and encouragement, but also for the hard question which incented me to widen my research from various perspectives.

I would like to thank Tokyo Metropolitan Government (TMG) for the generous funding and scholarship under the project of Asian Network of Major Cities 21(ANMC-21) and Asian Human Resources Fund program. I am grateful to Asst. Prof. Dr. Preechar Karin (KMITL) for introducing this exceptional scholarship to me to pursue a Ph.D. in TMU.

My gratefulness also sends to Dr. Sompong Srimanosaowapak, my academic advisor in MTEC, NSTDA. He taught me some of the most valuable skills I have gained during my master degree. Scientific research and writing are skills that everyone should have and have given me a huge advantage in the route to Ph.D. I would like to thank my colleagues in Near Net Shape Metal Manufacturing laboratory, especially P'Pang Thitima for their supports and helps me to get a master degree. In addition, I also thank TAIST and TGIST staffs for their kindly assistance. I would like to thank NSTDA for encouraging and for allowing me to grow as a research scientist.

My sincere gratitude goes to Dr. Arief Yudhanto (KAUST), who selflessly helped and supported me during my research. I would like to gratefully acknowledge the support from former and current members of Watanabe Laboratory, especially Dr. Atsushi Kondo

(e-Xtream Engineering, MSC Software), Dr. Satoshi Morooka, Dr. Ridlo Nasution, Dr. Jonny Herwan, Mr. Saharat Chantanumataporn, Mr. Prabij Joshi, my tutor Mr. Yousuke Oishi (Fuji Heavy Industries), Mr. Yasuhito Mikami, Mr. Norimasa Goto, Mr. Takuya Yoshida, Ms. Tomoko Inoue et al. Many thanks to my resident advisor in Hirayama, Prof. Ayumu Inasawa, and staff of TMU International Center and Hino campus for their kind help and support.

I am deeply indebted to Tezuka-sensei, Ishii-sensei, Kuze-sensei, and the members of Minamitama nihongonokai for helping me to adapt to Japanese life. I would also like to express my thanks to P'Nokhook and the members of Royal Thai Embassy, Tokyo for honored opportunities to work together and suggestion during I stay in Japan. I thank my fellow teammate at Thai restaurant JASMINE THAI, Coredo Muromachi.

Living in Japan would not be easier without heartfelt companion with Thai friends (Pang Taywin, Dr. Ya Peeramed (KMITL), Benz Pornphan, Som Potchara, P'Beer Atchara, N'Mewxiquez Athiwat, P'Good Dittapoom, Dr. Kwan Wannida (KMUTNB), P'Nan, TMU friends, Tokodai friends, Todai friends, TSAJ friends, TAIST-Tokyo Tech and football teammate ("FC TITAN and Power Crazy"), and everyone who came to visit me .

In addition, I would like express appreciation to my ex and someone who spent sleepless nights with and were always my support in the moments when there was no one to answer my queries.

Last but not the least, words cannot express how grateful I am to my mother, and father for all of the sacrifices that you've made on my behalf. Your prayer for me was what sustained me thus far. I cannot get the Ph.D. without an untiring supports from my beloved family. It is because of their unconditional love and trust that make everything in my life become possible.

BIOGRAPHY

Worawat Parasil was born in 1988 from Chachoengsao in the east of Thailand. He got bachelor's degree in aerospace engineering from King Mongkut's University of Technology North Bangkok. He received master's degree in automotive engineering, TAIST- Tokyo Tech program, from King Mongkut's University of Technology Thonburi. He got a scholarship to study the doctoral degree in Aerospace Engineering at Tokyo Metropolitan University from Tokyo Metropolitan Government under the "Asian Human Resources Fund" program. His current research interests fluid and structural interaction dynamics analysis, and computer modeling and simulation. Mr. Parasil focuses on the material nonlinearities as a rubberlike membrane, and geometry nonlinearities as the large deformation due to high excitation vibration. He also interests include aerodynamics, aluminum casting, mechanical properties investigation, and aircraft design.